The star-forming core ahead of HH 80N: studying the interaction with a parsec scale jet

Josep Maria Masqué Saumell

UNIVERSITAT DE BARCELONA

Departament d'Astronomia i Meteorologia

The star-forming core ahead of HH 80N: studying the interaction with a parsec scale jet

Memòria presentada per
Josep Maria Masqué Saumell
per optar al grau de
Doctor en Ciències Físiques
Barcelona, gener 2012

Programa de Doctorat d'Astronomia i Meteorologia

Bienni 2003–2005

Memòria presentada per **Josep Maria Masqué Saumell** per optar al grau de Doctor en Ciències Físiques

Directors de la tesi

Dr. Robert Estalella

Dr. Josep Miquel Girart

Agraïments-Agradecimientos

Durant el transcurs de la tesi, he rebut constantment mostres de suport per part de molta gent que, molts cops, han estat determinants per seguir avançant en el meu treball. Sovint, degut a presses i maldecaps, un simple 'gràcies' era la resposta a aquestes mostres d'ajuda. Crec que això no és suficient i que estic en deute amb aquestes persones. En aquest espai vull agrair amb tota sinceritat l'ajuda a tots aquells qui, de diverses formes, han contribuït en la conclusió d'aquest treball.

En primer lloc vull expressar el meu agraïment als meus directors de tesi. Gràcies Robert per introduir-me en l'apassionant món de la radioastronomia. Vull agrair-te també l'ajuda i el suport rebut durant tots aquests anys. Gràcies Josep Miquel per presentar-me la regió d'HH 80N, parella de ball durant tant de temps. Gràcies també pel suport i l'orientació rebuda de la qual n'he après moltes coses.

També estic agraït amb els membres del grup ràdio que durant tots aquests anys han anat passant pel DAM: Chema, Maite, Rosario, Àngels, Imma, Òscar, Aina, Gemma, Álvaro, Felipe, Pau, Marco. Moltes gràcies a tots per ajudar-me quan ho necessitava!

También debo agradecer a Mayra y a Guillem su contribución en esta tesis y también per su excelente hospitalidad durante mis estancias en el Instituto de Astrofísica de Andalucía (IAA). Gracias Mayra por acercarme al mundo del modelaje, y de transmitirme energía y ánimos frente a un reto tan difícil como ha sido modelar la fuente de HH 80N. Gràcies Guillem per la teva implicació en el projecte i per les discussions fructíferes al despatx, a les reunions de grup, dinant, fent el cafè..., que han estat determinants en el meu treball.

Òbviament, he d'agrair als membres del DAM tot el suport rebut. Gràcies a 'secre', JR, Montse i Rosa, per facilitar tràmits burocràtics a vegades gens trivials. Gràcies a la gent de suport, Jordi i Gabi, per la seva paciència a l'hora de solucionar problemes informàtics. No m'oblido dels estudiants que han estat companys i amics durant el temps que hem coincidit al DAM: Carme, Neus, Rosa, Sinuè, Pol, Javi, Víctor, Laura, Pere, Jordi, Javi, Teresa, Nadia, Adolfo, Kike, Santi, Andreu, Héctor, Nadia, Iñigo, Andreu, Maria, Eva, Maria, Benito (si m'he deixat algú prego que em perdoni!). El suport mutu fa que tot sigui mes fàcil!

Tampoc m'oblido dels companys de la carrera, alguns escampats arreu del món.

Gràcies Raül, Gemma, Helena, Puy, David, Olga (biòloga infiltrada), Mau, Maria, Miguel i, en especial, a tu Nuri, per haver compartit colze a colze moments delicats de l'etapa final de la tesi (ànim, que ja ho tens!). Gràcies també a tu, Darta, perquè, tot i no tenir gens clar el concepte 'termonuclear', jo et considero un petit físic atrapat en la ment d'un fiscal.

Gran part del mèrit d'aquesta tesi també te'l dec a tu, Patri. A pesar de que els nostres camins s'han separat, tu has viscut de prop durant molt de temps desenvolupament de la tesi donant-me una empenteta quan era necessari. Molta sort per Boston!

Finalment, gràcies també a la meva família, i als amics d'Alcover, de l'Espluga, de Valls, de Tarragona, de Cambrils,...que d'una forma o altra han contribuït a l'elaboració d'aquesta tesis. I perquè no hauria pogut créixer en un ambient millor.

Moltes gràcies a tothom!

Als meus pares i al padrí

...when you have eliminated the impossible,
whatever remains,
however improbable,
must be the truth?

Sherlock Holmes in The Sign of the Four
Sir Arthur Conan Doyle

Contents

Resum de la tesi: La font amb formació estel·lar per davant d'HH 80N: estudi de la seva interacció amb un jet a escala de parsecs

Introducció

D'ençà de la formulació de la llei de la gravitació universal per Isaac Netwon, està àmpliament acceptat que els estels s'han de formar necessàriament pel col·lapse gravitacional de la matèria interestel·lar. Gràcies al recent desenvolupament d'instruments moderns, que observen radiació electromagnètica a longituds d'ona ràdio, i tècniques computacionals avançades, hem estat capaços de desvelar com i on es formen els estels. Avui en dia, sabem que els estels es formen en les regions més denses de la Galàxia anomenades núvols moleculars. Segons la seva massa, els núvols moleculars es classifiquen en núvols foscos (masses de 10^3 $M_\odot$ i temperatures de 10–20 K), associats amb la formació d'estels de baixa massa, i els núvols moleculars gegants (masses de 10^4–10^6 $M_\odot$, i temperatures de $\sim$ 20 K) que alberguen agrupacions d'estels d'alta i baixa massa.

Els estels massius es formen ràpidament començant a cremar hidrogen al seu nucli quan encara es troben a la fase protoestel·lar. D'altra banda, els estels de baixa massa es formen en un procés gradual molt més ben conegut, tot i que les condicions inicials de les quals parteix el col·lapse protoestel·lar es debaten entre dos possibles escenaris. Una possibilitat consisteix en la formació quasi-estàtica i regulada magnèticament d'una regió d'alta densitat de gas dins del núvol molecular

(nucli dens). El col·lapse s'inicia des del centre del nucli i es propaga en forma d'ona de col·lapse cap a l'exterior a la velocitat del so. L'altra possibilitat implica la formació dinàmica de nuclis densos a partir de la turbulència del núvol molecular. Aquests dos escenaris representen casos límit i la realitat segurament es troba en una posició intermèdia. En qualsevol cas, en etapes més avançades del col·lapse, les regions més interiors del nucli dens es tornen suficientment opaques i calentes per frenar la caiguda de material, formant un nucli hidrostàtic. Finalment, el material envoltant el protoestel desapareix pràcticament i aquest es fa visible, en una etapa de lenta contracció fins que el gas al seu interior arriba a una temperatura prou alta per iniciar les reaccions termonuclears de l'hidrogen, esdeveniment que marca el naixement de l'estel.

El model detallat abans, però, no explica alguns fenòmens associats als objectes joves com, per exemple, la discrepància entre el moment angular dels embolcalls protoestel·lars i el dels estels formats posteriorment, o quin paper juga el camp magnètic en el procés de col·lapse dels nuclis densos. Els resultats de la rotació i la presència de camp magnètic en els nuclis densos són l'aparició de discos protoestel·lars i l'expulsió de gas d'alta velocitat en forma de vent estel·lar. Mentre que el camp magnètic també regula la contracció dels nuclis densos, es creu que la presència d'un disc protoestel·lar és crucial en la col·limació d'aquests vents a escales $\lesssim$ 100 AU. Els vents protoestel·lars s'expandeixen a escales més grans, i presenten una pèrdua de velocitat i un augment de l'angle d'obertura. En el cas dels estels massius, els seus vents poden arribar a expandir-se fins a escales de parsecs, contribuint significativament als moviments turbulents observats als núvols moleculars.

La teoria de formació estel·lar estàndard tampoc inclou la influència de l'entorn del nucli dens en el seu procés de col·lapse. Els estels no es formen isolats sinó en agrupacions, fet que suggereix que l'existència d'alguns estels podria ser conseqüència dels processos causats per estels veïns (e.g. vents, supernoves, regions HII) que poden produir inestabilitats gravitacionals al seu entorn induint el col·lapse de nuclis densos.

Observacionalment, el procés de formació estel·lar es pot estudiar mitjançant dos línies principals: l'emissió tèrmica de la pols al continu i la de les línies moleculars. L'emissió de la pols està directament lligada a la massa de l'embolcall, la qual va disminuint a mesura que el protoestel embegut evoluciona. En particular, s'ha proposat la distribució de l'emissió contínua entre 2.2 μm i 100 μm per establir l'estat

evolutiu dels nuclis protoestel·lars dels estels de baixa massa. Aquesta mètode no és aplicable als estels d'alta massa ja que aquests abandonen la fase pre-estel·lar mentre encara adquireixen material de l'embolcall. D'altra banda, donat que les condicions del gas a l'interior dels núvols moleculars permeten l'aparició de molècules, l'estudi de la química aporta informació sobre les propietats físiques del gas de les regions de formació estel·lar i del seu estat evolutiu. A més, la cinemàtica dels núvols moleculars es pot explorar basant-se en el desplaçament en freqüència Doppler de les línies moleculars causat pels moviments de gas, per exemple, de la turbulència o dels vents protoestel·lars.

La primera evidència de l'existència de vents col·limats d'alta velocitat emergint dels nuclis protoestel·lars (a la literatura se'ls coneix com a 'jets') es va observar en regions excitades pel seu xoc amb el medi interestel·lar, conegudes com a objectes Herbig-Haro (HH). Els objectes HH presenten una gran varietat de formes i distàncies a l'objecte protoestel·lar, i requereixen un ampli ventall de tècniques observacionals a l'hora de dur a terme seu estudi: les observacions ràdio al centimètric mostren ràdio-jets col·limats a escales pròximes a la font excitadora, mentre que observacions a l'òptic poden detectar sistemes d'objectes HH expandint-se fins a escales del parsec. De forma similar, les línies moleculars s'empren per explorar la interacció entre el jet i el gas de l'entorn. Per exemple, el gas escombrat i acumulat pel vent es detecta amb línies de CS i CO (Plambeck and Snell 1995; Moriarty-Schieven et al. 1987), mentre que a regions pròximes als objectes HH s'hi pot observar gran abundància de HCO^+, SO, CH_3OH, entre d'altres espècies. Curiosament, aquestes regions no mostren connexió dinàmica amb el vent. L'explicació més acceptada és que les altes abundàncies d'algunes molècules específiques són el resultat d'una alteració causada per la radiació ultraviolada provinent de l'objecte HH. Aquesta radiació és capaç d'arrancar molècules que prèviament es troben congelades a la superfície dels grans de pols en petites condensacions de gas pròximes a l'objecte HH. La inclusió de noves espècies en la fase gasosa desencadena una química de no equilibri que origina grans abundàncies de molècules específiques (e.g. HCO^+, SO, CH_3OH), tal i com demostren els models químics (Taylor and Williams 1996; Viti and Williams 1999a).

La regió d'HH 80N

La regió GGD 27, ubicada a Sagitari a la distància de 1.7 kpc (Rodríguez et al. 1980), és una regió activa de formació estel·lar que es destaca per albergar el jet protoestel·lar més llarg i col·limat conegut fins ara. Aquest jet, que emergeix de la font lluminosa IRAS 18162−2048 de 1.7×10^4 $L_\odot$ i s'expandeix fins a una llargada total de 5 pc, presenta vents amb velocitats de fins a 600-1400 km s^{-1}, provocant xocs d'alta excitació al llarg del jet: existeixen evidències que la radiació ultraviolada (UV) dels xocs és capaç d'induir una regió foto-dissociada al seu entorn (Molinari et al. 2001). A més, al sud de IRAS 18162−2048 es troben els objectes HH 80 i HH 81, els més lluminosos mai observats. En canvi, la contrapartida nord d'aquests objectes, HH 80N, situada 3 pc al nord de IRAS 18162 − 2048, només s'ha detectat en emissió ràdio degut a una forta extinció causada per la presència d'un núvol molecular al davant de l'objecte HH.

Observacions de la regió al voltant d'HH 80N usant diverses espècies moleculars revelen que a 0.3 pc de l'objecte HH hi ha un nucli dens de 0.3 pc de grandària, (font d'HH 80N), que presenta altes abundàncies de CS, l'NH_3 i l'HCO^+ (Girart et al. 1998), suggerint una alteració química per part de la radiació UV de l'objecte HH. Posteriorment es van detectar signes de formació estel·lar a la font tal i com indiquen la presència d'un flux bipolar protoestel·lar traçat en CO i una estructura d'anell, traçada en CS, contraient-se a velocitats supersòniques. Aquesta morfologia probablement no és real, sinó un efecte de disminució d'abundància de CS a les zones centrals de la font. Les propietats cinemàtiques peculiars de la font d'HH 80N combinades amb el fet d'estar al costat d'un dels jets estel·lars més potents fan d'aquesta regió la més apropiada per estudiar la formació estel·lar induïda per un agent extern.

Objectius i estructura de la tesi

L'objectiu d'aquesta tesi és l'estudi de la influència dels jets protoestel·lars en regions de formació estel·lar del seu entorn, centrant-nos en el cas particular de la regió d'HH 80N. En primer lloc estudiem els efectes que tenen el fotons UV provinents d'HH 80N sobre la química de la font d'HH 80N, molt més massiva i extensa que altres

condensacions estudiades en regions pròximes a objectes HH, i amb un possible objecte protoestel·lar embegut. En segon lloc estudiem la física del col·lapse de la font, fent èmfasi en la possible influència del flux HH 80/81/80N. Per tal d'assolir aquests objectius, durant el període de realització de la tesi hem dut a terme una àmplia campanya observacional recollint dades corresponents a línies moleculars així com també d'emissió al continu. L'estructura de la tesi és la següent:

En primer lloc, en el Capítol 1, fem una introducció a la formació estel·lar i a la regió d'HH 80N. En el Capítol 2 construïm mapes de l'emissió centimètrica de l'extrem nord del jet HH 80/81/80N amb un gran camp de visió per esbrinar la grandaria real del jet, requisit indispensable per poder considerar la influència del jet a la font d'HH 80N. En el Capítol 3 analitzem la química de la font d'HH 80N dins del marc de la foto-il·luminació UV. En el Capítol 4 investiguem la física del col·lapse de la font, modelant la seva emissió al continu usant models estàndard de col·lapse protoestel·lar. En el Capítol 5 inspeccionem la cinemàtica del gas en les regions més denses de la font. En el Capítol 6 presentem observacions complementàries adquirides amb telescopis d'antena única amb l'objectiu d'estudiar les propietats de l'embolcall extens de la font d'HH 80N. Finalment, en el Capítol 7 fem una discussió general dels resultats d'aquesta tesi i presentem l'escenari concloent proposat per a la regió d'HH 80N.

Observacions de l'emissió al continu centimètric de l'extrem nord del jet d'HH 80/81/80N

Recentment s'han descobert alguns objectes HH situats a distàncies de parsecs de la seva font excitadora, implicant grandàries molt grans per als jets protoestel·lars (Bally and Devine 1994; Reipurth et al. 1997). No obstant, a vegades la dificultat d'associar objectes HH amb un jet determinat genera incertesa en les dimensions reals dels jets protoestel·lars.

Amb l'objectiu de mesurar la grandària del jet HH 80/81/80N, vam dur a terme observacions de l'emissió centimètrica al continu de l'extrem nord del jet utilitzant el VLA/EVLA. Les observacions es van realitzar en tres sessions. Dues sessions corresponen a observacions a 6 cm i 20 cm en configuració C. La tercera sessió correspon a observacions a 6 cm en configuració D. Els mapes resultants de les tres

sessions (veure figura 2.3) mostren diferents 'nusos' d'emissió traçant marginalment el jet, a més d'una nova font $10'$ al nord-est no detectada anteriorment. Aquesta font apareix alineada amb el jet i té un índex espectral negatiu similar a HH 80, HH 81 i HH 80N (Martí et al. 1993).

Extrapolant cap al nord el model que representa la trajectòria d'un jet al pla del cel emprat a Martí et al. (1993), si variem lleugerament els paràmetres de precessió, trobem que la posició de la font és compatible amb que aquesta pertanyi al jet. Això ens permet considerar la relació causa-efecte entre la presència del jet HH 80/81/80N i l'evolució dinàmica de la font d'HH 80N: donat que des de l'inici del col·lapse fins a l'aparició del protoestel ha transcorregut un període determinat de temps, en el cas de que HH 80N fos l'extrem nord del jet, a l'inici del període aquest hauria d'estar lluny de la font d'HH 80N, fent impossible la seva influencia sobre el col·lapse. No obstant, considerant la possibilitat que la nova font del nord pertanyi al jet, la seva grandària i edat dinàmica s'allargarien considerablement, fent possible la influència del jet a la font d'HH 80N.

L'emissió molecular de la font d'HH 80N

Recentment, observacions en regions al voltant d'objectes HH revelen que aquests poden tenir condensacions moleculars associades (Rudolph and Welch 1988; Davis et al. 1990; Torrelles et al. 1992, 1993; Girart et al. 1994, 1998, 2002, 2005; Viti et al. 2006; Whyatt et al. 2010). Tot i estar a les immediacions d'un jet estel·lar, aquestes condensacions no mostren signes d'alteració dinàmica directa (e.g. xocs amb el vent). L'explicació d'aquest fenomen, proposada per Wolfire and Koenigl (1993), és que la radiació UV provinent de l'objecte HH penetra en petits grumolls de gas transitoris del núvol per on el jet es propaga. La radiació UV deslliga les molècules que es troben a la superfície dels grans de pols provocant l'augment d'abundància de determinades espècies moleculars fent aquestes condensacions 'visibles', ja que d'altra forma no es detectarien amb les línies de les espècies en qüestió degut a que la vida d'aquests grumolls és massa curta per sintetitzar-les. La situació de la font d'HH 80N la converteix en un clar exemple de condensació irradiada. No obstant, la seva grandària i massa, són significativament més grans que les típiques derivades per a les condensacions pròximes a objectes HH ($\leq$ 0.1 pc i M$\sim$ 1 $M_{\odot}$). Això, sumat a la possible formació estel·lar, suggereix una naturalesa de la font d'HH 80N

diferent d'altres condensacions irradiades.

En aquest capítol mostrem un estudi de la química de la font d'HH 80N mitjançant un conjunt d'observacions de línies moleculars dutes a terme amb l'interferòmetre BIMA en configuració C. Els resultats mostren que l'emissió molecular, en general, segueix una estructura allargada en la direcció SE-NW, similar a la franja d'adsorció de la imatge d'arxiu a 8 μm d'Spitzer. Aquesta imatge infraroja també mostra un pic d'emissió al centre de la font, indicant la presència d'un objecte protoestel·lar. Una inspecció més detallada dels mapes de canals de les transicions revelen una cinemàtica interessant el llarg de l'eix major de l'estructura allargada. L'anàlisi de la morfologia i la cinemàtica de l'emissió molecular, mitjançant diagrames posició velocitat (diagrames PV), confirma l'estructura d'anell contraent-se detectada prèviament amb CS (Girart et al. 2001). La resta de molècules tracen només parcialment l'anell, suggerint una diferenciació química al llarg de l'estructura.

A part d'obtenir dades espectroscòpiques, amb BIMA també vam observar l'emissió tèrmica de la pols a 1.4 mm, detectant emissió marginal coincident amb el pic de 8 μm. El possible rang de masses derivat a partir de la pols, $1.6-3.1\ M_{\odot}$, està molt ben correlacionat amb el moment del flux detectat amb CO segons la relació de Bontemps et al. (1996) i demostra la joventut de l'objecte embegut, ja que gran part del material de l'embolcall encara ha de caure sobre el protoestel. De fet, tenint en compte les densitats típiques observades a partir de les quals les molècules es congelen als grans de pols Tafalla et al. 2002, juntament amb la densitat mínima crítica per a que molècules com el CS o l'HCO^+ es termalitzin, trobem un possible rang de densitats per a l'anell molecular de $5 \times 10^4 - 1.3 \times 10^5$ cm^{-3}. Considerant aquestes densitats juntament amb les dimensions de l'anell ($\sim 2.5 \times 10^4$ i $\sim 6.0 \times 10^4$ AU pels radis intern i extern, respectivament) podem concloure que aquest alberga una gran reserva de material. Per tant, l'anell representa un embolcall traçat per les diferents espècies moleculars. Una inspecció detallada de la diferenciació química al llarg d'aquest embolcall, a partir de la comparació amb les abundàncies d'una mostra de regions de formació estel·lar de diferents tipus, mostren que els fotons UV alteren la part de la font propera a HH 80N.

Estudi de la font d'HH 80N a diferents longituds d'ona

Tot i que el model clàssic de col·lapse protoestel·lar descriu el procés de formació estel·lar de forma satisfactòria en primera instància, resten detalls del procés, de caràcter secundari, que discrepen amb la teoria. Per exemple, el model assumeix condicions estàtiques inicials abans de l'inici del col·lapse al centre del nucli dens (Shu 1977), contràriament a les velocitats de col·lapse supersòniques observades al nucli d'HH 80N per a un radi de $\sim 6.0 \times 10^4$ AU. En aquest capítol mostrem els resultats del modelatge de l'emissió continua de la pols de la font d'HH 80N observada amb un gran nombre d'instruments (PdBI, IRAM 30m, APEX, VLT) usant models d'embolcalls col·lapsant dins el marc clàssic de la formació estel·lar.

Els mapes d'emissió continua a totes les longituds d'ona tenen un pic coincident a la mateixa posició, consistent amb la presència d'un objecte jove (IRS1) a la font. A més, els mapes d'alta resolució angular del PdBI mostren una condensació secundària al sud-est de IRS1 (SE) aparentment sense cap protoestel associat. Complementàriament, en aquest capítol presentem dades d'amoníac obtingudes amb el VLA i comparem la morfologia de l'emissió d'amoníac amb la de la pols. La semblança entre els dos traçadors (a excepció d'un lleuger augment de l'emissió d'amoníac a l'est de la font) indica que la presència d'amoníac a la font és deguda a les altes densitats de gas típiques de les regions de formació estel·lar, més que pel fet d'estar irradiat pels fotons UV provinents d'HH 80N.

En el modelatge ens hem centrat en IRS1 usant diversos enfocs. En primer lloc hem considerat el col·lapse d'una esfera de gas amb la densitat depenent del radi com r^{-1} (esfera singular logatròpica SLS, Mclaughin et al. 1996) inicialment estàtica. En un moment donat, el col·lapse s'inicia al centre de l'esfera i es propaga com una ona en expansió cap a enfora. En el segon enfoc hem adoptat el mateix tipus de col·lapse però per a una esfera de gas amb densitat r^{-2} (esfera singular isotèrmica, SIS, Shu 1977). Finalment, adoptem la solució de col·lapse anàloga al cas SIS però incloent-hi rotació uniforme (embolcall TSC, Terebey et al. 1984). En cada cas, suposant que la lluminositat total de la font es la suma de la lluminositat del protoestel més la causada per la caiguda del gas a la seva superfície, hem resolt l'equació de transport radiatiu al llarg de l'embolcall adoptant una llei d'opacitat donada. Com a observables, hem comparat per una banda, la distribució espectral

d'energia (SED) del model amb l'obtinguda integrant l'emissió al continu de les nostres observacions a diferents longituds d'ona, complementades amb dades d'arxiu dels satèl·lits *IRAS*, *Spitzer* i *Akari*. Per l'altra banda, hem comparat els perfils d'intensitat d'emissió al continu mil·limètric obtinguts a partir de mapes observats amb els mapes sintètics del model. El millor ajust el trobem calculant la funció χ^2 per a un sèrie de models obtinguts escombrant diversos paràmetres (ritme de caiguda de gas sobre el protoestel, radi de l'embolcall i massa del protoestel). Degut a limitacions computacionals, pel model TSC hem dut a terme una exploració cas per cas fins a trobar un model satisfactori.

Pels casos SLS i SIS, no hem trobat cap model que satisfaci conjuntament l'ajust de la SED i dels perfils. En l'ajust SLS la massa no es distribueix adequadament en l'embolcall, implicant perfils d'intensitat massa plans respecte els observats. Contràriament, en l'ajust SIS, trobem models amb uns perfils d'intensitat òptims, però que prediuen una lluminositat del model massa alta, donant fluxos que superen els límits superiors de la SED obtinguts a partir de dades del satèl·lit IRAS. A més, tant el cas SLS com el SIS prediuen una intensitat a 3 mm menor del que s'observa. Això podria ser degut a la presència d'un disc protoestel·lar a IRS1, no considerat en els models anteriors, l'emissió del qual seria dominant a 3 mm.

Com a conseqüència de la rotació i de l'evolució de les propietats dels grans de pols, la presència d'un disc és consistent amb el cas TSC. Per tant, en l'emissió modelada de l'embolcall TSC hi hem afegit la d'un disc extret del catàleg de D'Alessio et al. (2005). A més, la lluminositat resultant del model TSC pot resultar menor que la seva contrapartida SIS segons l'angle d'inclinació de la font, solucionant així el problema d'excés de lluminositat dels models SIS. Explorant diferents models, hem trobat que tant la SED com els perfils d'intensitat poden reproduir-se mitjançant un model d'embolcall TSC que consisteix en una esfera de gas de 20 $M_\odot$ de massa, 105 $L_\odot$ de lluminositat i 1.5×10^4 AU de radi a partir del qual el gas cau en caiguda lliure, més un disc de 0.6 $M_\odot$ de massa i 300 AU de lluminositat. L'edat derivada per IRS1 és de 2×10^4 anys. Segons aquests model, a radis més grans que 1.5×10^4 AU l'embolcall ha de ser estàtic, aparentment en contradicció amb l'estructura d'anell trobada anteriorment amb les observacions de BIMA. No obstant, l'emissió molecular apareix molt més estesa als mapes i, a més, el mapa de PdBI revela una possible fragmentació de la font. Això suggereix que part de la font d'HH 80N està formada per un embolcall molecular, amb vàries condensacions embegudes (IRS1 i SE), les propietats del qual podrien estar afectades pel flux d'HH 80/81/80N.

Observacions interferomètriques de la font d'HH 80N amb molècules nitrogenades

Els resultats del modelatge de IRS1, implicant un embolcall estàtic a radis més grans que 1.5×10^4 AU, entren amb conflicte amb la presencia de l'anell molecular contraient-se a velocitats supersòniques. Tenint en compte l'extensió de l'emissió molecular i la fragmentació observada amb al mapa del PdBI, existeix la possibilitat que el règim de col·lapse protoestel·lar es trobi localitzat al voltant d'IRS1, mentre que l'embolcall extens de la font d'HH 80N podria tenir una cinemàtica pròpia, possiblement afectada pel flux HH 80/81/80N. Per tal d'estudiar aquesta possibilitat hem dut a terme observacions interferomètriques d'alta resolució angular d'espècies nitrogenades (NH_3, NH_2D i $HN^{13}C$) usant el PdBI i el VLA. Les espècies nitrogenades es caracteritzen per la seva resistència a adherir-se sobre els grans de pols per a densitats del gas, 10^5-10^6 cm^{-3}, molt més altes que les d'adhesió del CS. Per tant, mitjançant el l'estudi de les seves línies podem recuperar informació del gas en regions de la font pròximes a IRS1, on el CS i altres molècules observades amb BIMA hi són absentes.

La morfologia de l'emissió de les molècules nitrogenades presenta un allargament SE-NO similar al de les espècies observades amb BIMA, però amb una morfologia més compacte. L'NH_3 (2,2) representa una excepció i mostra només emissió marginal en dos pics: un coincident amb IRS1 i l'altre situat $10''$ a l'est. Degut a que les observacions d'amoníac es van dur a terme durant la transició EVLA-VLA, quan el seguiment Doppler no estava disponible, hi ha un desplaçament instrumental en velocitat no controlat. Per tant, a l'anàlisi cinemàtic de la font d'HH 80N només usarem l'NH_2D i l'$HN^{13}C$. Inspeccionant el camp de velocitats que tracen aquestes molècules, trobem que la font es pot dividir en dues parts amb propietats ben diferenciades entre l'est i oest. La meitat est, on es troba el major volum d'emissió d'aquestes molècules, té un camp de velocitats més gran i un desplaçament en velocitat de 0.5 km s^{-1} respecte a la part oest. IRS1 es troba a la zona límit entre les dues parts de la font.

Per tal d'entendre la cinemàtica de la font d'HH 80N, hem obtingut els diagrames PV anàlogament com hem fet amb les dades de BIMA. Trobem que el gas traçat amb NH_2D com amb $HN^{13}C$, té velocitats radials menors que les detectades amb CS al voltant d'IRS1. Això descarta la possibilitat que la cinemàtica detectada a la

font d'HH 80N correspongui a moviments gravitatòriament lligats, ja que l'NH_2D i l'$HN^{13}C$ tracen regions de l'embolcall més pròximes a IRS1 que el CS. D'altra banda, l'aparença morfològica dels diagrames PV de l'NH_2D i l'$HN^{13}C$ mostra que el gas dens segueix una estructura asimètrica consistent amb la diferenciació cinemàtica entre la part est i oest de la font, però lluny de la que s'espera a partir d'un anell col·lapsant. Per tant, concloem que l'estructura d'anell vista amb CS és el resultat de la combinació de gradients de velocitat del gas amb densitat moderada al llarg de la font d'HH 80N.

L'observació de NH_3 i NH_2D a la font d'HH 80N font ens permet mesurar el seu nivell de deuteració, obtenint valors de fins al 40%, similars als valors més alts observats en altres regions de formació estellar (Crapsi et al. 2005). La fracció de deuteració està íntimament lligada a l'evolució de les condensacions de gas que es troben en l'estadi previ a la formació d'estels al seu interior, mostrant un nivell de deuteració més alt aquelles que tenen altes densitats columnars d'H_2 i baix nivell de turbulència, i que, per tant, estan a la vora del col·lapse protoestel·lar. Deixant de banda una possible influència dels fotons UV d'HH 80N a la fracció de deuteració a l'extrem est de la font, el pic de deuteració a SE implica que aquesta condensació probablement formarà un protoestel imminentment. D'altra banda, IRS1 mostra un nivell més baix de deuteració indicant que ja ha iniciat el col·lapse i ha aparegut un objecte central al seu interior el qual altera el gas del seu entorn. Independentment de l'estat evolutiu de les condensacions de la font d'HH 80N, la presència de NH_2D a la font d'HH 80N implica que el gas dens ha hagut d'estar present a la font durant un període almenys de 10^6 anys, d'acord amb els models químics. Tenint en compte l'edat dinàmica del flux HH 80/81/80N (10^5 anys, Yamashita et al. 1989), deduïm que la font d'HH 80N ja existia abans de l'arribada del flux.

Observacions de l'embolcall molecular de la font d'HH 80N mitjançant telescopis de plat únic

Els estels es formen en condensacions de gas fredes (10-15 K) i denses (2×10^3-2×10^5 cm^{-3}) que es formen a partir de la fragmentació d'una estructura més gran, sovint de forma filamentosa (Schneider and Elmegreen 1979; Hacar and Tafalla 2011). Aquest podria ser el cas de la font d'HH 80N, per la qual el mapa de l'emissió al continu obtingut amb el PdBI mostra varies condensacions, IRS1 i SE, embegudes

en un embolcall més extens. Les propietats d'aquestes condensacions podrien haver-se heretat de l'embolcall de la font d'HH 80N. Per tal de caracteritzar les propietats d'aquest embolcall extens, possiblement afectades pel jet d'HH 80/81/80N, vam dur a terme observacions de la font d'HH 80N amb telescopis de plat únic (IRAM 30m i MOPRA).

Durant les observacions d'IRAM 30m vam fer diversos apuntats al llarg de la font d'HH 80N sintonitzant diferents línies sobretot de CS i SO. Durant les observacions de MOPRA vam fer un únic apuntat al centre sintonitzant línies d'espècies deuterades entre d'altres. Com a resultat general, veiem que la majoria d'espectres tenen un doble pic, consistent amb els resultats trobats anteriorment respecte la presència de dues components a la font d'HH 80N. Mentre que a 3 mm es detecten gairebé totes les línies observades, aquest no és el cas a 1 mm, on les línies es detecten marginalment.

El fet d'observar diferents transicions d'una mateixa molècula ens permet derivar propietats físiques del gas emissor (densitat i temperatura) i la densitat columnar de la molècula en qüestió. La nostra estratègia ha consistit en obtenir intensitats de línies sintètiques a partir de RADEX, un codi que modela la transferència radiativa de l'emissió molecular, i compar-les amb les intensitats observades. Aquesta comparació es fa calculant la funció χ^2 obtinguda per a un conjunt de condicions físiques possibles per al gas. Els resultats d'aquesta anàlisi indiquen que el gas de la font d'HH 80N traçat pel CS i SO és majoritàriament fred ($\leq$ 15 K) i moderadament dens $\leq 10^5$ cm^{-3}).

A més, a partir de l'emissió a 1.2 mm, podem obtenir la densitat columnar d'H_2, que juntament amb la densitat columnar de les espècies obtingudes amb l'anàlisi RADEX, ens permet derivar abundàncies. A partir de la comparació d'abundàncies amb els models d'evolució química (Bergin and Langer 1997; Aikawa et al. 2005), hem deduït que, en primer lloc, la font d'HH80N ha de ser més vella que 10^5 anys, tal i com indica la no detecció de C_2S (de Gregorio-Monsalvo et al. 2006). En segon lloc, tot i l'edat avançada de la font d'HH 80N, les condensacions al seu interior s'han hagut de formar en molt poc temps.

Discussió general: el rol del flux HH 80/81/80N

El jet HH 80/81/80N pot influenciar a la font d'HH 80N de dos formes: l'alteració radiativa deguda als fotos UV provinents d'HH 80N afectant principalment la química; i l'alteració dinàmica, que pot provocar la formació estel·lar induïda a la font.

L'interès per estudiar la influència radiativa d'HH 80N sorgeix arrel de la diferent naturalesa intrínseca de la font d'HH 80N comparada amb altres condensacions ubicades a les proximitats d'objectes HH, sent aquestes últimes molt més petites i menys massives. En primer lloc trobem que la gran quantitat de material de la font d'HH 80N impedeix que els fotons UV penetrin ben a dins de la font, limitant els efectes fotoquímics a la seva 'superfície'. En segon lloc, el efectes fotoquímics només es detecten a la part est de la font, a 0.2 pc d'HH 80N, romanent altres parts de la font més llunyanes a l'objecte HH inalterades. Això implica que la fotoquímica és un fenomen de caire local.

Inspeccionant els espectres d'$HN^{13}C$, NH_2D i CS trobem que no existeix alteració de xoc per part del jet d'HH 80/81/80N. No obstant, la interacció dinàmica pot existir indirectament mitjançant ones magneto-hidrodinàmiques alimentades pel jet. Aquestes moviments poden arrastrar masses de gas escombrat que eventualment, poden col·lisionar amb el nucli d'HH 80N. Un petit càlcul demostra que el jet HH 80/81/80N injecta prou moment a la regió per alimentar indirectament la cinemàtica observada a la font d'HH 80N. En un estudi recent, Duarte-Cabral et al. (2011) simula la col·lisió de dos núvols. La semblança dels seus diagrames PV sintètics amb els nostres és notable.

En cas d'haver-hi col·lisió entre una massa de gas arrossegada i la font d'HH 80N, es podrien desencadenar algunes inestabilitats donant lloc al naixement induït d'estels. El temps d'interacció derivat a partir de la cinemàtica observada a la font ($\sim 10^5$ anys), molt més gran que el de IRS1 (2×10^4 anys), permet considerar aquesta possibilitat. Anàlisis similars al presentat al Capítol 4 per altres regions de formació estel·lar, poden ajudar a compendre si la formació estel·lar provocada per un agent extern és un fenomen freqüent o no. Independentment de la possibilitat d'haver-hi formació estel·lar induïda a la font, l'èxit en el modelatge del Capítol 4 usant models estàndard de formació estel·lar implica que el procés de col·lapse, un cop iniciat, no es desvia del procés de formació clàssic d'estels a pesar de partir d'unes condicions inicials probablement diferents.

Resum de l'escenari final proposat per la regió d'HH 80N

A al figura 7.6 presentem un possible escenari que explica la cinemàtica dels diferents traçadors moleculars. Havent abandonat la hipòtesi de la morfologia d'anell per la font d'HH 80N, considerem una possible col·lisió d'una massa de gas arrossegada degut a ones magnetohidrodinàmiques generades al jet d'HH 80/81/80N. Aquest fenomen crearia la diferenciació cinemàtica, apreciada amb NH_2D, entre la part est de la font, que rebria la col·lisió, i la part oest que preservaria la velocitat original de la font d'HH 80N. IRS1 i SE es trobarien a la regió de col·lisió, que és on s'acumula la major part del material de la font d'HH 80N, sent aquest un resultat consistent amb els de Duarte-Cabral et al. (2011). Els gradients de velocitat del gas de moderada densitat podrien simular l'aparença d'anell als diagrames PV, tal i com es veu amb CS. De cara al futur, són necessàries simulacions hidrodinàmiques seguint la línia de Duarte-Cabral et al. (2011) per a confirmar aquest escenari.

Chapter 1

Introduction

1.1 Physics of star formation

1.1.1 Standard models

Since the formulation of the law of gravitation by Isaac Newton in *Philosophiae naturalis principia mathematica* (1687), it is accepted that stars must form by the gravitational collapse of interstellar matter. However, understanding how an almost empty medium can condense and heat up to densities and temperatures 20 and 6 orders of magnitude higher, respectively, had open questions. For example 'what is the nature of the material from which stars are made out?' or 'are stars still forming nowadays?'.

The modern telescopes observing at radio wavelengths and advanced computational techniques can provide answers to these questions. Nowadays, we know that stars form in molecular clouds (see Fig. 1.1). These clouds, composed basically of H_2 and dust, are the densest regions of the interstellar medium. Their size is variable but two general types can be distinguished: dark clouds and giant molecular clouds. Typically, dark clouds have sizes of a few parsecs, masses about 10^3 $M_\odot$ and gas temperatures of 10–20 K. There is a large number of dark clouds in the Galaxy and some of them are close enough (< 500 pc) to be seen in silhouette against the background galactic stars (see Fig. 1.1). On the other hand, giant molecular clouds have masses of 10^4–10^6 $M_\odot$, temperatures of ~ 20 K and extend over tens of parsecs.

Indeed, they are the largest structures in the Galaxy. Dark clouds are associated with the formation of low-mass stars ($M < 8\ M_{\odot}$), while giant molecular clouds are the cradles of rich stellar clusters where high-mass ($M > 8\ M_{\odot}$) and low-mass protostars can be found.

Figure 1.1: The Pipe Nebula (also known under the astronomical names of Barnard 59, 65-67 and 78) seen against the brighter clouds of the Milky Way's disk in the Ophiuchus constellation is an example of a dark molecular cloud. Courtesy ESO/Yuri Beletsky.

There is different physics behind the formation of high-mass stars and low-mass stars. While low-mass stars form steadily undergoing a pre-main sequence evolution, high-mass stars form very rapidly and start to burn hydrogen still in the protostellar phase (Palla and Stahler 1993). The high luminosity of massive protostars implies strong radiation pressure that may halt the infall and, hence, the existence of high-mass stars is puzzling. Some explanations involve accretion of material through a circumstellar disk similarly to the formation of low-mass protostars, or stellar growing by merging protostars.

The formation of low-mass stars is much more well understood, even though two

possible explanations of how the collapse of a cloud core is initiated are confronted. One possibility is that the gas of the cloud is magnetically driven (Shu et al. 1987) and a core forms and evolves quasi-statically to a r^{-2} radial density profile (Singular Isothermal Sphere, Shu 1977). The collapse then begins at the center of the core an propagates outwards as an expansion wave at the speed of sound. This approach, also called inside-out collapse, agrees qualitatively with observations of nearby low-mass collapsing cores (e.g. B335, Zhou et al. 1993). The second possibility is that the collapse begins with an unstable core created by turbulence (Hayashi 1966; Klessen 2001). In this approach, the collapse departs from an uniform isothermal sphere and suits better with the star formation process found in rich clusters (e.g. NGC 1333 IRAS 4A, Belloche et al. 2006). The approaches discussed above are two limiting cases and, probably, the reality is somewhere in between.

At the innermost regions of the core, when the gas density reaches values $\rho \simeq 10^{-13}$ g cm^{-3}, the opacity increases and the gas behavior switches from isothermal to adiabatic. The gas becomes then hot enough to stop the collapse and the first hydrostatic core is formed. Gradually, the mass of the envelope surrounding the growing protostar will decrease until the protostellar photosphere becomes visible. At this point, accretion is no longer occurring. The protostar will remain contracting in the pre-main sequence stage until it becomes hot enough to start thermonuclear reactions in its center, which establishes the birth-line of the star.

1.1.2 Effects of rotation and magnetic fields: disks and collimated winds

Despite the successful scenario of low-mass star formation outlined above, several caveats still have to be addressed. For instance, a star has typically less angular momentum than its equivalent mass in the interstellar medium, which is called the angular momentum problem. Observations show that protostellar envelopes rotate with angular velocities of a fraction of km s^{-1} pc^{-1} beyond a few 10^3 AU from the protostar (e.g. angular velocities of 0.5–1 km s^{-1} pc^{-1} at a radius of 1.1×10^4 AU were derived in IRAM0 4191+1522, Belloche et al. 2002) even though, recently, Tobin et al. (2011, 2012) have questioned the common interpretation of the observed velocity gradients in protostellar envelopes as rotation, showing that an important part of the observed kinematics could be due to projected infall velocities. One of the consequences of a rotating core is the formation of an inner flattened structure

as a result of the conservation of angular momentum during the collapse (Cassen and Moosman 1981). The physical structure of disks is difficult to determine at earliest stages of protostellar evolution because they are surrounded by thick dusty envelopes (e.g. Jørgensen et al. 2005).

On the other hand, magnetic field plays an important role in the evolution of star forming cores. First, it regulates the contraction of the core providing an effective pressure against gravitational collapse. This is the basis of the Shu et al. (1987) model where the authors consider that the r^{-2} density profile is reached quasi-statically. Second, it can remove angular momentum from the protostar and disk system via a magneto-centrifugal mechanism that could drive winds emanating from the protostellar system (Pudritz and Norman 1983). Observations show that these winds are collimated at scales $\lesssim$ 100 AU (see Anglada 1996). This sets a strong observational limitation for the proper study of the collimation process owing to the lack of sufficient angular resolution for the typical distance of star forming sources. Only the use of advanced instruments such as PdBI or SMA (and the recently commissioned ALMA) may overcome this observational difficulty. Although the collimation mechanism is still a matter of debate, the presence of a protostellar disk is believed to be crucial in this process (Shu et al. 1995). The collimated winds are observed as jets at the inner parts of the core (at scales of $\sim$1-3 $\times 10^4$ AU), and outflows at larger scales (from 3×10^4 to 10^5 AU). The lower velocity and broader opening angle of large outflows in comparison with jets suggest that the latter are made of gas from the protostellar environment that has been accelerated by the interaction with the jet.

High-mass protostars are also observed to launch outflows but at larger scales, up to several pc. The momentum and energy of such giant outflows are considerably higher than their counterparts of low-mass protostars. Many studies show that the injection of energy to the surrounding ambient cloud by giant outflows can be an important source of turbulence that, in turn, can regulate the star formation rate and efficiency in the cloud (Bally et al. 1996; Reipurth et al. 1997). Consequently, giant HH flows can provide an important feedback to the star formation in the cloud affecting the emergence of a new generation of stars.

1.1.3 Protostellar collapse triggered by an external agent

Although the standard theory of protostellar collapse may provide a good zeroth-order description of the star formation process, more sophisticated models are needed to explain peculiar cases. The assumed initial conditions of the standard model consisting of an isolated non-rotating isothermal sphere are unrealistic. The high proportion of multiple systems suggest that most stars are formed in clustered mode and, hence, the protostellar collapse may be affected by the feedback of the neighboring protostars.

Perturbations caused by the external medium may produce gravitational instabilities and induce a core to collapse (Hennebelle et al. 2003). Examples of triggered star formation by an external agent can be found in several environments: expanding HII regions (Wilking et al. 1984; Healy et al. 2004), stellar winds (Redman et al. 2003) or molecular outflows (Yokogawa et al. 2003). All these phenomena, resulting from the stellar feedback, are often present in star forming regions. Understanding how stars form in different environments is paramount to achieve a complete scenario of star formation.

1.2 Observational signatures

1.2.1 Thermal dust emission

At the earliest stages of evolution, protostars are invisible because of the surrounding thick and massive envelopes of infalling material. These envelopes are made of very cold gas and dust at a few tens of K. With such temperatures, the spectral energy distribution (SED) of a star-forming core peaks at long wavelengths because the protostellar light is absorbed and reprocessed by the cold envelope.

The mass of the envelope decreases gradually because, as the protostar grows, it is removed by the outflow and a large fraction of material is accreted onto the accretion disk and the protostar. The dust opacity law $\kappa_\nu \propto \nu^\beta$ of the disk has a slope β distinctly shallower than that for diffuse interstellar medium because of grain growth (Beckwith and Sargent 1991). The resulting mass and temperature distribution of the envelope are modified accordingly, and so does the SED. High-

mass protostars evolve rapidly leaving the pre-main sequence phase while material is still accreting onto their surface. Therefore, their evolutionary stage is difficult to determine observationally. On the contrary, the evolutionary stage of low mass protostars can be inferred from the thermal emission of their envelope. The energy distribution spectral index $\alpha = -d\ \log(\nu\ F_\nu)/(d\ \log\ \nu)$, where F_ν is the spectral energy distribution, estimated between 2.2 μm and 100 μm, can be used to classify protostellar cores into four classes (Lada 1987; Andre et al. 1993):

Class III objects $(-3 < \alpha \leq -2)$: Pre-main sequence objects. Their spectral energy distributions coincide with a black body at the temperature of its photosphere. There is little contribution at infrared wavelengths, indicating that the accretion process is almost completed.

Class II objects $(-2 < \alpha \leq 0)$: Their spectral energy distribution is broadened, showing an infrared contribution. This proves the existence of some dust surrounding the protostar, mainly found in the accretion disk.

Class I objects $(0 < \alpha \leq 3)$: This class includes objects embedded in a dense medium and not visible. They are systematically brighter than Class II and Class III objects due to the accretion luminosity.

Class 0 objects $(3 \leq \alpha)$: Their spectral distribution, similar to that of a very low temperature black-body, is interpreted as evidence for a cold dust envelope emission. Almost all the luminosity is produced by the accretion shock, indicating that, as Class I objects, this class includes objects in the main accretion phase.

This classification is believed to represent an evolutionary scheme of low mass star formation being the Class 0 sources the youngest and Class III sources the oldest (but see Masunaga and Inutsuka 2000, for caveats to this classification).

1.2.2 Molecular line emission

One of the most amazing discoveries of the last century is the presence of molecules in the interstellar medium. Molecules are found in molecular clouds mainly because of two reasons. First, molecular clouds have high gas densities involving frequent collisions between atoms allowing the formation of complex molecules. Second, dust is abundant in clouds and shields complex molecules from destructive interestellar radiation. The fact that molecular gas is associated with sites of star formation makes molecules useful probes of the physical conditions of star forming material. Because of the low temperature of molecular clouds, rotational levels of molecules are excited. The transitions between rotational levels emit lines with frequencies at radio wavelengths.

The chemical evolution of gas is linked to the evolution of star-forming regions. Thus, the molecules that are sensitive to a particular environment can be used to understand the evolutionary state of protostellar cores (e.g. from dark and dense clouds prior to the formation of protostars, to evolved cores with parts of the envelope heated by the protostellar radiation or shocked by outflows, see Fig. 1.2). Many models aimed at describing the chemical evolution of these environments have been developed over the last decades. The contribution of these models in the understanding of molecular line observations is crucial. The gain in complexity of chemical models over the last years is notorious: starting from pure gas-phase networks (Bates and Spitzer 1951; Herbst and Klemperer 1973) and pure grain-surface chemistry models (Allen and Robinson 1977; Tielens and Hagen 1982), nowadays, both contributions can be merged, including the effects of density increase due to core contraction (Rawlings 1982; Bergin and Langer 1997; Garrod et al. 2005; Taylor et al. 1998). Furthermore, radiative heating and outflow from the central star, as well as UV irradiation (e.g. from a HH shock), has been also considered (Draine and McKee 1993; Ceccarelli et al. 1996; Taylor and Williams 1996; Viti and Williams 1999b,a).

Despite the difficulty of obtaining a perfect match between model predictions and observations, in part due to the complexity of chemical networks, significant progress has been made and several *universal* results have been obtained. First, chemical inhomogeneities within molecular clouds have been observed, typically when comparing the spatial distribution of carbon-bearing molecules such as CS with nitrogen-bearing molecules such as NH_3 and N_2H^+ when there is no source of

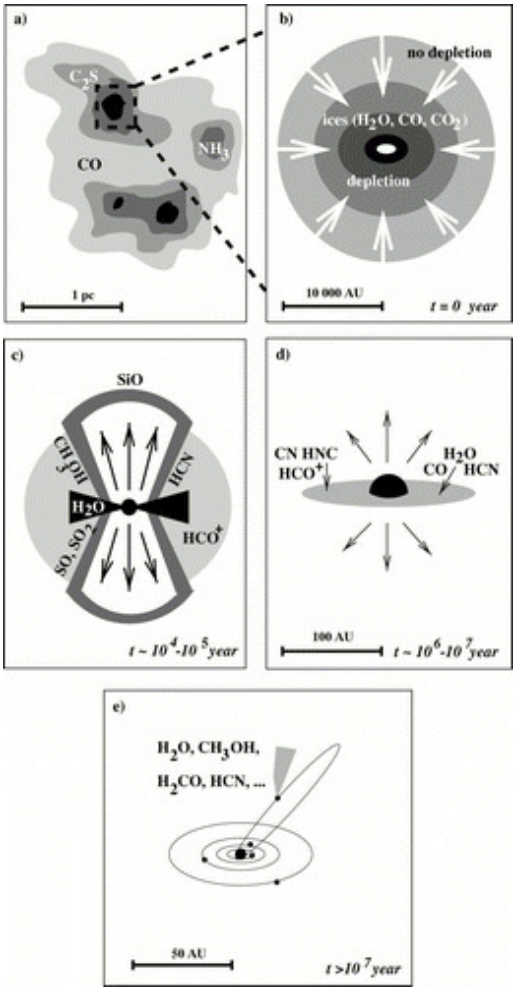

Figure 1.2: A schematic view of the chemistry characteristic of each stage of low-mass star formation: (a) Dense starless cores with different chemical evolution leading to chemical inhomogeneity throughout the region: C_2S and CO are anti correlated with NH_3. (b) A starless core starts contracting gradually until the envelope collapses dynamically onto a central hydrostatic object. Most species, specially C-bearing molecules, freeze out onto the grains at low temperatures and high densities. (c) High accretion and supersonic outflow occur in a deeply embedded protostar. The emergence of some new species, such as CH_3OH and SiO, is the result of the stellar feedback (i.e. protostellar heating and outflow). (d) The protostellar envelope is cleared out by the outflow and a Young T Tauri star and a residual accretion disk appear visible. The combination of ion-molecule chemistry and photon-dominated chemistry gives high abundances of species such as CN and HNC in the disk. (e) Planetary system resulting from the evolution of the residual accretion disk with a central star. While some molecular species are processed on the planetesimals, comets retain molecules in their ices, such as H_2O and CH_3OH, with abundances typical of earlier stages of protostellar evolution (Figure by MR Hogerheijde after Shu et al. (1987)).

heating (Pastor et al. 1991; Suzuki et al. 1992; Morata et al. 1997). These differences are attributed to different timescales for the species to form and destroy (Howe et al. 1996; Taylor et al. 1996). In addition, once the collapse starts, the increasing density accelerates this effect due to the freeze out of some molecular species onto the dust grains (Rawlings et al. 1992; Bergin and Langer 1997; Tafalla et al. 2002). An extreme case is found in the deuterated species, where for a particular gas conditions their abundance ratio with respect to their hydrogenated counterparts can be dramatically enhanced with respect to the standard D/H ratio (Roberts and Millar 2000; Bacmann et al. 2003; Roberts et al. 2003; Roueff et al. 2005). Second, there are some key molecules that are associated with particular environments or events. For instance, SiO and HCO^+ are associated with outflows (Martin-Pintado et al. 1992; Whyatt et al. 2010, see next section)

Molecules also provide information on the velocity fields present in the cloud. The velocity of a given parcel of gas causes a Doppler shift with respect to the rest frequency of the molecular line. If the velocity is due to unresolved turbulent motions (or thermal agitation at small scales) the observed line becomes broader. On the other hand if the line emission comes from gas with systematic, well-organized motions, the resulting line profile depends on the particular type of coherent motion (i.e. infall, outflow or rotation, Di Francesco et al. 2001). In addition, several velocity components can overlap in the same spectrum due to the finite angular and velocity resolution of instruments. Thus, a proper interpretation of line shapes requires sensitive interferometric observations with a good *uv* coverage.

1.3 Outflows and Herbig-Haro objects

The protostellar outflow activity was first observed at optical wavelengths through regions of excited plasma known as Herbig-Haro objects (HH objects) that are the result of shocks of the fast flowing gas with the interstellar medium (Herbig 1950, 1951; Haro 1952, 1953). There is a rich array of possible morphologies for HH objects: some have bow shapes and others have jet-like morphology, although such regular morphologies are rare and most HH objects present chaotic structures. HH objects are present at a wide range of distance from the protostar. Until the mid-1990s, HH objects were generally found around a fraction of parsec from low-mass protostars (Mundt et al. 1987). However, the advent of large field of view CCD

detectors reveal that some HH objects extend up to the scale of parsecs from young stars (e.g. HH 111, Reipurth et al. 1997). These objects belong to the so-called giant HH flows and are associated with the formation of massive protostars.

Due to the high excitation of HH objects, they emit practically in all the wavelengths and, hence, their study covers a wide range of observational techniques. For example, high angular resolution centimeter continuum observations reveal thermal radio-jets at scales very close to the exciting source (e.g. HH 1-2, Rodríguez et al. 1990). At these wavelengths, the emission is mainly free-free radiation coming from the shock-ionized material of the jet. The extinction caused by the dust is the principal obstacle for observing the region where the jet is launched. Therefore, interferometric observations of the free-free emission from the jet with radio interferometers, which can effectively sample regions within the circumstellar environment, offer an excellent opportunity to study the collimation process.

In addition, molecular line observations are commonly used to explore extended structures associated with outflow interaction with the cloud environment. For example, SiO (Sandell et al. 1994), H_2O, OH or HCO^+ (Neufeld and Dalgarno 1989) are key molecules to map shocked regions, while the swept gas is preferably traced by CS (Plambeck and Snell 1995) and CO (Moriarty-Schieven et al. 1987). Besides, other species such as SO, CH_3OH and HCO^+ are found to be good tracers of irradiated gas where the UV illumination generated in the shock is important (Girart et al. 2005; Viti et al. 2006). Indeed, claims for evidence of association of localized regions of molecular line emission with HH objects have been growing over the last decades (Rudolph and Welch 1988; Davis et al. 1990; Torrelles et al. 1992, 1993). These regions contains dense gas ($\geq 1 \times 10^4$ cm^{-3}) and have small filling factors when observed with single-dish telescopes (e.g. $\sim$10%, Whyatt et al. 2010). They are believed to be small transient clumps that condense and disperse in timescales of the order of 10^6 yr (Taylor and Williams 1996). These clumps do not show evidence for shock heating and therefore they are not connected dynamically with the jet. A possible explanation for the association of molecular clumps with HH objects, proposed by Wolfire and Koenigl (1993), is that the UV radiation is capable of evaporating icy mantles on dust grains, triggering a non-equilibrium chemistry that leads to an increase in abundance of specific molecular species. In this sense, HH objects are probes of clumpiness in molecular clouds (Whyatt et al. 2010).

1.4 The HH 80N region

1.4.1 The HH 80/81/80N jet

The region GGD 27 (Gyulbudaghian et al. 1978), located in Sagittarius at a distance of 1.7 kpc (Rodríguez et al. 1980), is an active star forming region. The most well-known observational signature of this region, the HH 80/81/80N jet, is one of the largest collimated jet systems known so far, spanning over a total length of ~ 5 pc (Martí et al. 1993, see Fig. 1.3). Synchrotron radiation, indicating the presence of relativistic electrons, has been found in this jet (Carrasco-González et al. 2010). The jet is powered by a young, high-luminosity protostellar object, IRAS 18162−2048 with a total luminosity, from the IRAS survey, of $1.7 \times 10^4\ L_\odot$. Recently, Fernández-López et al. (2011) detect compact millimeter emission towards this source, which is interpreted by these authors as arising from a massive ($\sim 4\ M_\odot$), and compact ($r \lesssim 300$ AU) disk. VLA observations carried out towards IRAS 18162-2048 by Rodríguez and Reipurth (1989) reveal that this source is elongated, pointing toward HH 80 and 81, the brightest Herbig-Haro objects known. Furthermore, they find several radio knots aligned with the central source and the HH objects, indicating that these condensations probably trace a highly collimated jet. Evidence of wiggling of the flow axis suggests that the driving source is precessing (Martí et al. 1993). HH 80 North (hereafter HH 80N) is the northern radio counterpart of HH 80 and 81. HH 80N, undetected at optical waveleghts because of the high extinction caused by a molecular cloud in the foreground, is located 3 pc to the north of IRAS 18162−2048.

The high outflow velocities, up to 1400 km s^{-1}, derived from proper motions measurements (Martí et al. 1995, 1998), suggest that the emission arising from the radio jet is due to very strong shocks (Heatcote et al. 1998). Strong UV radiation, generated in the Herbig-Haro shocks and the jet, is able to induce the formation of a photodissociation region (PDR) along the bipolar outflow (Molinari et al. 2001).

1.4.2 The HH 80N core

There is a large (0.3 pc in size) dense core ~ 0.3 pc ahead of HH 80N (hereafter HH 80N core, see Fig. 1.4) first detected in ammonia (Girart et al. 1994) and afterward in other molecular species (Girart et al. 1998, 2001; Masqué et al. 2009).

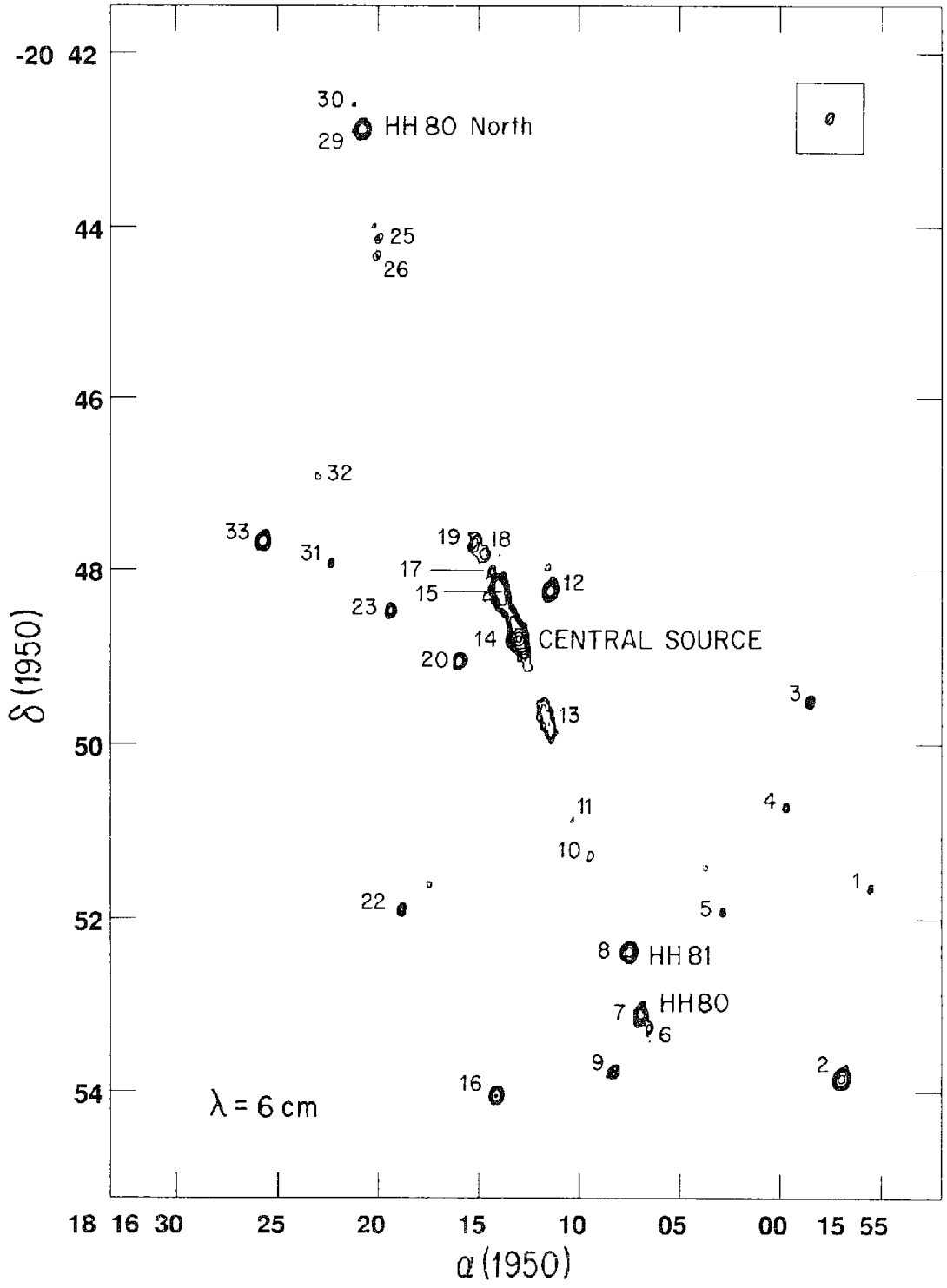

Figure 1.3: (From Martí et al. 2001). VLA 6 cm continuum emission of the GGD 27 region. Contour levels are -3, 3, 4, 5, 7, 10, 20, 50, and 100 times 20 μJy, the rms noise of the map. The beam is shown in the top right corner. Note the presence of small knots connecting the central source with the HH objects HH 80/81 and HH 80N.

A comparison between the CS, NH_3 and HCO^+ emission led Girart et al. (1998) to suggest an unusual chemistry for this core. A mass of roughly 20 $M_\odot$ and a rotational temperature of $\sim$ 17 K was estimated by Girart et al. (1994) from the ammonia emission of the core.

Interestingly, Girart et al. (2001) found evidence of a bipolar CO outflow centered near the peak of the HH 80N molecular core, suggesting the presence of an embedded protostar (hereafter, IRS1). In addition, Girart et al. (2001) and Masqué et al. (2009) interpreted the distribution and kinematics of CS and other molecular species observed in the outer parts of the HH 80N core as suggestive of an infalling ring-like molecular structure (probably caused by strong molecular depletion in the inner parts of the core) with a radius of $\sim$0.24 pc and infall velocities of $\sim$ 0.6 km s^{-1}. At 17 K, the isothermal sound speed is $\sim$0.2 km s^{-1}, implying that the contracting velocities of the ring are supersonic. This rises the question whether the HH 80/81/80N outflow has triggered or at least sped up the collapse of the core.

The location of the HH 80N core close to the most powerful jet system known up to date, combined with its peculiar properties described above, makes this region one of the most appropriate to study the triggering of star formation by an outflow.

1.5 About this work

1.5.1 Goals of the thesis

This thesis aims at probing the influence of protostellar outflows to nearby star forming cores by studying the particular case of the HH 80N core. To do so, we first study the chemical properties of the core in the frame of HH photoillumination. The HH 80N core is larger and more massive than other HH irradiated clumps, and harbors an embedded object, suggesting a different nature for this core. Our first goal is to see if the HH 80N core has a chemistry similar to that observed in other clumps ahead of HH objects.

In the following step, we study the physical properties of the HH 80N core in order to look for evidence of the influence of the HH 80/81/80N jet in the star formation process that is taking place in this core. While many studies on triggered

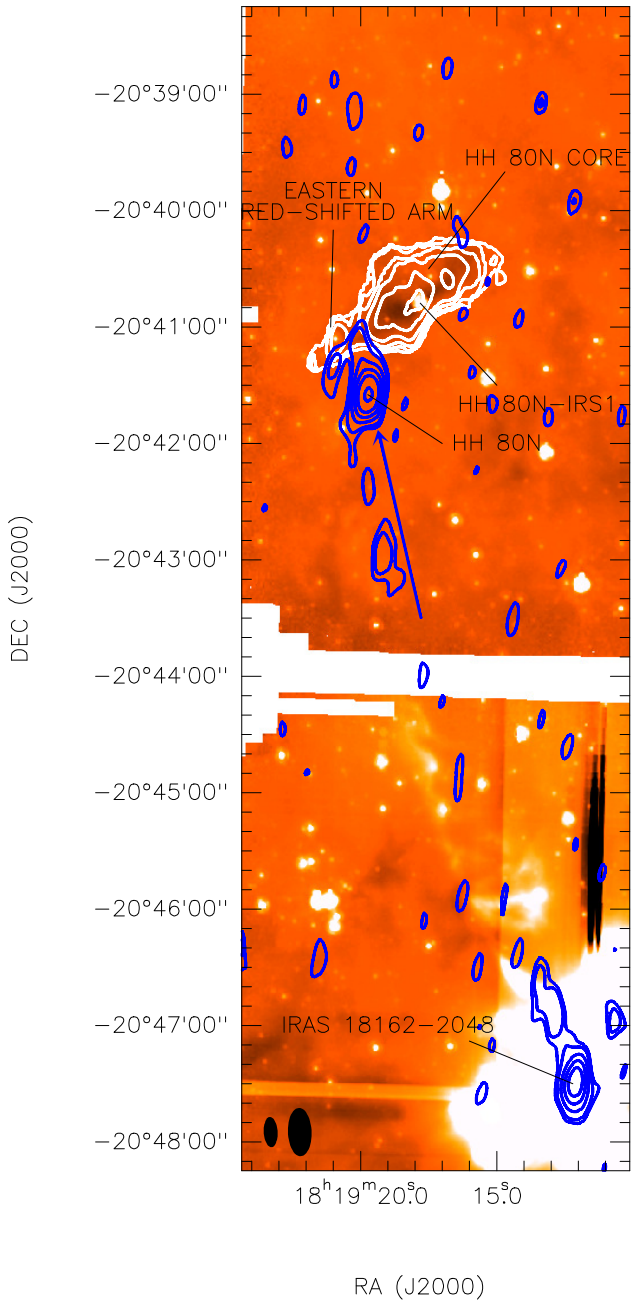

Figure 1.4: VLA 6 cm continuum emission (blue contours) of the GGD 27 region and integrated CS (2-1) emission (white contours) superimposed over the *Spitzer* 8 μm image of the GGD 27 region. The 6 cm continuum emission traces the HH 80/81/80N jet and HH 80N. The white contours traces the HH 80N core that is also seen in absorption against the background emission in the *Spitzer* image. The beams of the CS (left) and the continuum 6 cm (right) are shown in the bottom left corner. The blue arrow shows approximately the direction of the HH 80/81/80N flow. The bright 8 μm compact source seen approximately at the center of the absorption feature and the CS emission is associated with the embedded object within the HH 80N core powering the CO bipolar outflow detected in Girart et al. (2001).

star formation are based on the statistics of a large number of objects (e.g. Chauhan et al. 2011), in this thesis we focus our study on an isolated star-forming core to find direct evidence of interaction of the HH 80/81/80N outflow with the core.

1.5.2 Strategy

The previous works on the HH 80N region (Girart et al. 1994, 1998, 2001) have shown the complexity of this region. In order to understand the phenomena occurring in the region, we carried out a wide observational campaign of continuum and molecular line observations towards the HH 80N region, focusing on the study of the star formation process of the HH 80N core, the physical and chemical structure of the envelope and its kinematics.

We previously mapped the continuum centimeter emission of a region covering the northern head of the jet in order to measure its actual size. This is crucial to test the possibility of a cause-and-effect relationship between the HH 80/81/80N jet and the star forming signatures found in the HH 80N core. Then, we analyze the continuum emission of the HH 80N core using self-consistent standard models of protostellar collapse to see if the dynamical evolution of this core departs from the predictions of classic models of isolated star formation. In low-luminosity sources such as the HH 80N core, the continuum thermal emission is faint at mm wavelengths. High sensitivity receivers, such as bolometers, are needed to provide data with the required signal to noise for a proper modeling. In this thesis, we use bolometric data of SABOCA (APEX, 350 μm) and MAMBO-II (IRAM 30m, 1.2 mm). In addition, we complement these data with continuum observations at 3.5 mm wavelengths (PdBI), and at IR wavelengths (VLT and archival data of *IRAS*, *Spitzer* and *Akari* satellites).

We analyze a wide molecular dataset obtained with interferometric observations. Part of this dataset corresponds to archive BIMA data obtained from observations carried out by our group. The BIMA data are used to derive chemical properties along the HH 80N core (i.e. inspect chemical abundances in the core vs. the distance from HH 80N). In addition, in order to obtain a complete picture of the kinematics of gas in the HH 80N core, we carried out PdBI and VLA observations at D configuration that provides an angular resolution of 3″ and 5″ (i.e. ∼5000 AU and 8500 AU at 1.7 kpc of distance), respectively, of selected N-bearing molecules. The

supersonic infall velocities of the HH 80N core are derived from CS, which is strongly depleted in the densest regions of this core (Girart et al. 2001). N-bearing species, on the other hand, do not freeze out until very high densities (10^6–10^7 cm^{-3}). The analysis of N-bearing molecules allows us to study gas motions in regions of the core inaccessible to the observations of Girart et al. (2001).

The physical structure of the envelope of the HH 80N core is inspected from a multi-transition analysis of several molecular species using the non-LTE radiative transfer code RADEX. This analysis requires observations of several transitions of each species in order to constrain properly the physical conditions of the emitting gas. We derive physical parameters of several representative regions throughout the core. We used the IRAM 30m telescope receivers (heterodine AB and EMIR) that makes possible the observation of several transition lines simultaneously.

1.5.3 Thesis outline and status of different projects

The structure of the thesis is outlined in the following.

In Chapter 2 we map the northern head of the HH 80/81/80N jet at centimeter wavelengths in order to look for radio knots further north than HH 80N. This is required to inspect the possible cause-effect relationship between the passage of the jet near the HH 80N core and the presence of an embedded object in this core.

Chapter 3, we focus the study on the chemistry of the HH 80N core. Girart et al. (1998) find signatures of photochemical activity in the HH 80N core. We performed a follow-up study including additional species observed with better angular resolution than in the Girart et al. (1998) observations. This work, entitled *The molecular emission of the irradiated star forming core ahead of HH 80N* and authored by Josep M. Masqué, Josep M. Girart, Maria T. Beltrán, Robert Estalella, & Serena Viti, appeared in The Astrophysical Journal, 2009, volume 695, page 1505.

In Chapter 4, we analyze the continuum emission of the HH 80N core using self-consistent models of standard protostellar collapse. We inspect different model geometries, from spherical to sheet-like morphology, and discuss the inclusion of a protostelar disk. This work, entitled *A multi-wavelength study of the star-forming core ahead of HH 80N* and authored by Josep Maria Masqué, Mayra Osorio, Josep Miquel Girart, Guillem Anglada, Guido Garay, Robert Estalella, Nuria Calvet, &

Maria Teresa Beltrán, appeared in The Astrophysical Journal, 2011, volume 738, page 43.

In Chapters 5 and 6 we focus our study on the molecular envelope of the HH 80N core. We present the preliminary results of observations of N-bearing molecules and discuss the kinematics of the envelope. In Chapter 6 we perform a multi-transition analysis using single-dish data and derive the properties of the emitting gas in several parts of the HH 80N core.

Finally, in Chapter 7 we discuss the global results and summarize the main conclusions of this work.

Additionally to this thesis work, I have been involved in other projects that have resulted in several publication:

- Pau Frau, Josep Miquel Girart, Maria Teresa Beltrán, Oscar Morata, **Josep M. Masqué**, Gemma Busquet, Felipe de Oliveira Alves, Álvaro Sanchez-Monge, Robert Estalella, Gabriel A.P. Franco, & Aina Palau *Young starless cores embedded in the magnetically dominated Pipe Nebula.* 2010, The Astrophysical Journal, 723, 1665.

- John J. Tobin, Lee Hartmann, Hsin-Fang Chiang,Leslie W. Looney, Edwin Bergin, Claire J. Chandler, **Josep M. Masqué**, Sébastien Maret, & Fabian Heitsch *Complex Structure in Class 0 Envelopes II: Kinematic Structure from Single-Dish and Interferometric Molecular Line Mapping.* 2011, The Astrophysical Journal, 740, 45.

Chapter 2

Centimeter continuum observations of the northern head of the HH 80/81/80N jet

2.1 Introduction

Collimated HH flows arising from protostellar objects are among the most spectacular observed phenomena during the star formation process. These flows can extend over parsec-scale distances (Bally and Devine 1994; Reipurth et al. 1997). However, the measurement of the actual length of HH flows can be sometimes controversial, since it is not easy to associate distant and tentative HH objects to a specific HH flow without further evidence (e.g. through proper motions or physical properties of the object).

Here we report the results of recent cm continuum observations carried out with the VLA/EVLA toward the northern lobe of the HH 80/81/80N jet to look for knots further away than HH 80N. This is crucial to study a possible cause-effect relationship between the passage of the HH 80/81/80N jet near the HH 80N core and the presence of a protostellar object, IRS1, in this core. The IRS1 protostellar object has an age of 2×10^4 yr (see Chapter 4). Thus, the possibility that the HH 80/81/80N jet has influenced the dynamics of the dense molecular core around IRS 1 implies that the jet has a dynamical age similar or higher than the IRS 1 age.

2.2 Observations and results

VLA/EVLA continuum observations of the northern part of the HH 80/81/80N radio-jet were obtained as a part of a multi-frequency program composed of three blocks. The dates, wavelengths and configuration, as well as other observational parameters, are given in Table 2.1

Table 2.1: Summary of the VLA continuum observations.

Observing Epoch	Configuration	λ (cm)	Synthesized Beam ($''$)	P. A. (Deg.)	Phase Calibrator	Bootstraped Flux Density (Jy)	rms noise (μJy beam^{-1})
2009 Jun 21	C	6	6.6 × 3.5	-2.7	J1820-254	1.045 ± 0.009	30
	C	20	25.1 × 14.0	-2.9	J1833-210	13.97 ± 0.18	250
2009 Oct 25/26	D	6	19.9 × 9.7	10.0	J1820-254	1.20 ± 0.16	40

One observing run of seven hours, which consisted of two blocks, was carried out in June 2009 in the C configuration in the L and C bands. We set the phase center at the position of the HH 80N object, $\alpha(J2000) = 18^{\rm h}19^{\rm m}19\overset{\rm s}{.}74$ and $\delta(J2000) = -20°41'34\overset{''}{.}9$. In October 2009 we carried out an additional observing run of four hours in the D configuration at the C band. In this observing run we performed a two point mosaic with one field centered at the HH 80N position and the other offset ($81''$, $328''$). A bandwidth of 100 MHz (for the two polarizations) was employed in all the observing runs. The flux calibrator was always 3C286 with an adopted flux density of 7.47 Jy and 15.00 Jy at C and L bands, respectively. Data were edited and calibrated using the AIPS package of NRAO.

The maps were highly contaminated by the emission of a strong radio source with a flux density of 200 mJy and 110 mJy at L and C bands, respectively. This source was first reported by Furst et al. (1990) from a radio continuum survey at 11 cm obtained with Effelsberg 100m (their source num. 359). It is usually refereed in the literature as J1819−2036 and is located at $\alpha(J2000) = 18^{\rm h}19^{\rm m}36\overset{\rm s}{.}9$ and $\delta(J2000) = -20°36'31\overset{''}{.}0$, clearly outside the primary beam of the first observing block at C band (FHWM of $9'$). In order to avoid the strong side lobes generated by this source, in the second run we added a second pointing (81" East and 328" North of HH 80N), so the source is located only $163''$ from the phase center of this pointing. This allowed us to properly self-calibrate the visibilities of the second run using J1819−2036 as a reference and subtract the clean components.

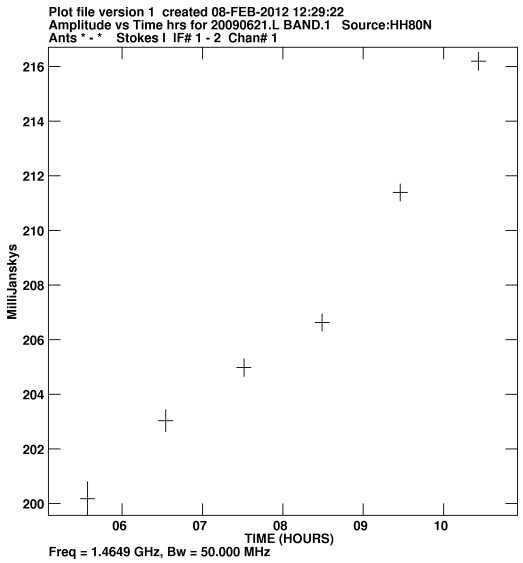

Figure 2.1: Plot of the visibility amplitude (averaged into 6 bins) vs. time for the L band observations. The flux level of 200 mJy corresponds to J1819−2036 that clearly dominates the flux of the region. The vertical bars represent the standard deviation of the bins.

However, the flux of J1819−2036 is time variable (see Fig. 2.1) that still generates residual side-lobes if we follow the procedure described above. In order to remove completely the J1819−2036 emission in the maps, each observing run was split in intervals of $\sim$ 30 min. Then, for each interval, we performed the self-calibration and clean component subtraction process as described above. As a comparison, the resulting maps corresponding to the northern pointing of the second observing run, after and before the subtraction of the clean components of J1819−2036, are shown in Fig. 2.2. The resulting final maps of the whole GGD 27 region for the three observing blocks are shown in Fig. 2.3. As seen in this Figure, IRAS 18162−2048 is elongated pointing to HH 80N. Several marginal knots appear in the map connecting both objects following the shape of a jet. At L band, contamination at short baselines, probably due to Galactic background emission, prevent to map properly the extended emission. About 10′ northeast of HH 80N, there is a northern source detected at all the wavelengths not reported before (Source 5).

Table 2.2 gives the measured position, flux at C and L bands, and the spectral index of the sources seen in the field. Our flux values are systematically slightly lower than the fluxes reported in Table 2 of Martí et al. (1993), possibly due to

calibration uncertainties. The spectral indexes are consistent with those derived in Martí et al. (1993) except for HH 80N, for which we found spectral index slightly more negative.

Source 5 appears to be located about 6′ north of HH 80N (10′ from IRAS 18162-2048), roughly in the direction of the HH 80/81/80N radio jet. This source has a negative spectral index of −0.46, similar to the values found for HH 80, HH 81 and HH 80N. Therefore Source 5 is possibly a radio knot belonging to the HH 80/81/80N radio jet.

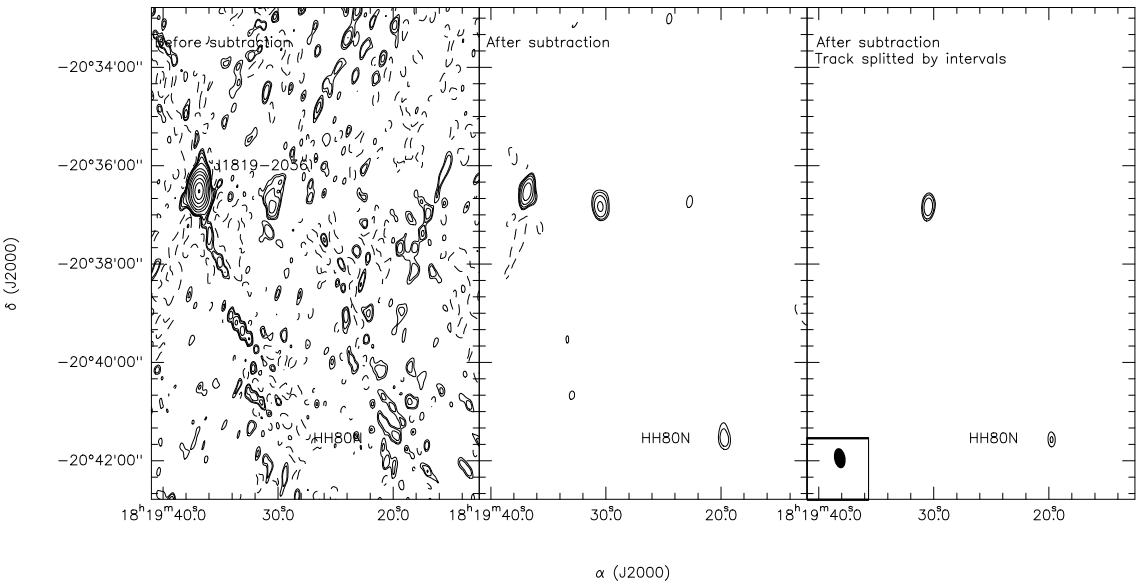

Figure 2.2: Maps of the region around J1819−2036 observed in the D configuration at C band. The left panel shows the resulting sidelobes after a standard CLEANing process. The middle panel shows the resulting sidelobes after self-calibrating the visibilities and subtracting the clean components of J1819−2036. The right panel show the resulting map after self-calibrating the visibilities and subtracting the clean components of J1819−2036 separately for each ∼ 30 min interval splitted out from the observing run. In all the maps, contours are -3, 3, 4, 6 and 10 times 100μJy. For the map of the left panel, the contours 18, 50, 100, 200, 400, 700 and 1100 times 100μJy have been added. The beam is shown in the bottom left corner of the right panel.

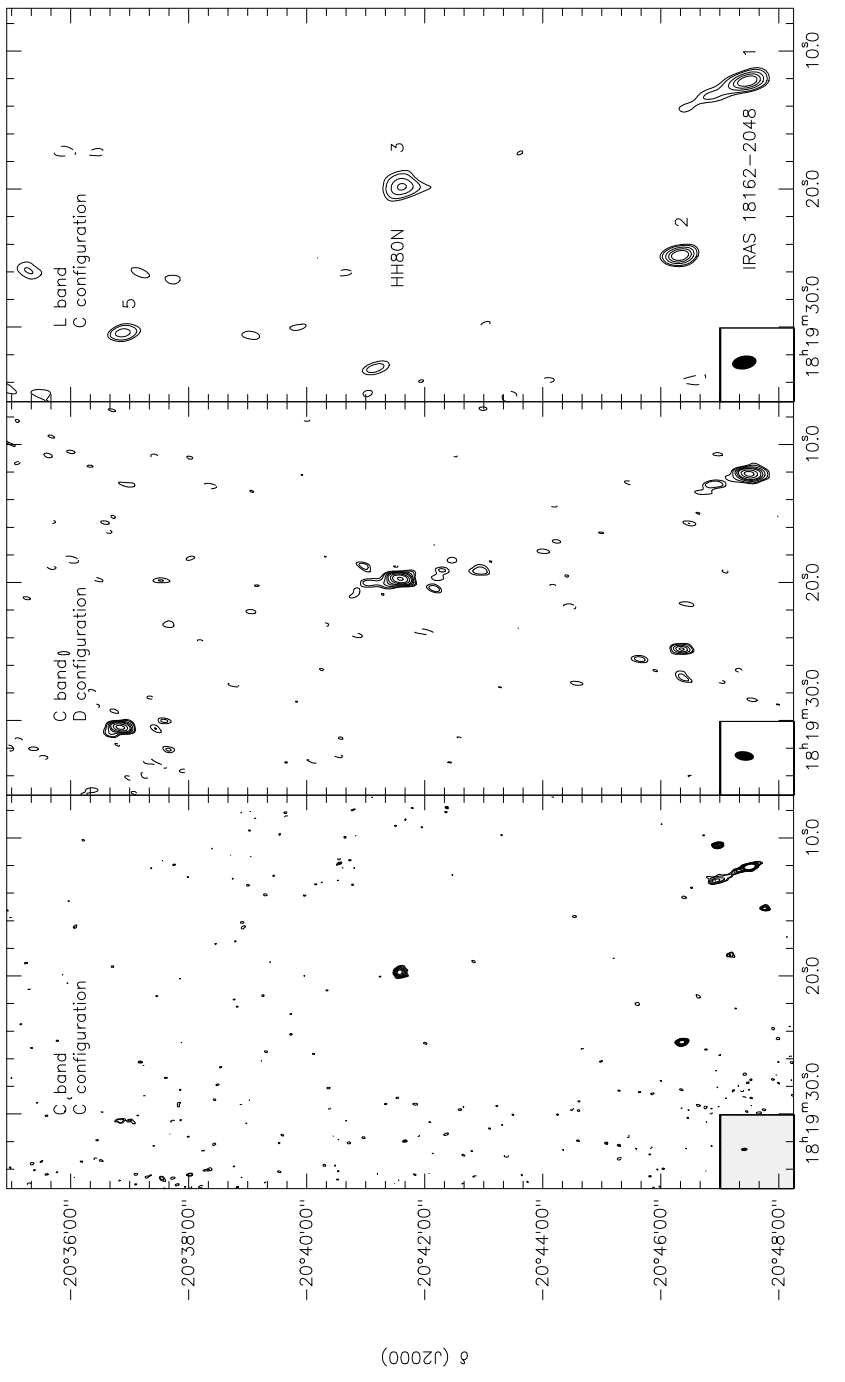

Figure 2.3: Northern lobe of the HH 80/81/80N jet mapped with centimeter continuum emission. The left panel shows the 6 cm continuum map obtained with C configuration. The middle panel shows the 6 cm continuum map obtained with D configuration. The right panel shows the 20 cm continuum map obtained with C configuration. Contour levels are -3, 3, 4, 6, 8, 10, 14, 18, and 25 times 30, 50 and 250 μJy, the rms noise of the left, middle and right maps, respectively. The beam is shown in the bottom left corner of each panel.

Table 2.2: Parameters of the sources found in the HH 80N region[a]

	Peak Position		$S_{\rm Lband}$	$S_{\rm Cband}$	
Source	α (J2000)	δ (J2000)	(mJy)	(mJy)	Spectral Index
1[b]	$18^{\rm h}19^{\rm m}12\overset{\rm s}{.}106$	$-20°47'30\overset{''}{.}834$	3.77 ± 0.10	4.29 ± 0.06	0.11 ± 0.01
2	$18^{\rm h}19^{\rm m}24\overset{\rm s}{.}812$	$-20°46'21\overset{''}{.}751$	3.13 ± 0.06	1.12 ± 0.04	-0.84 ± 0.03
3[c]	$18^{\rm h}19^{\rm m}19\overset{\rm s}{.}780$	$-20°41'33\overset{''}{.}343$	3.72 ± 0.20	2.05 ± 0.15	-0.49 ± 0.04
4[d]	$18^{\rm h}19^{\rm m}36\overset{\rm s}{.}743$	$-20°40'29\overset{''}{.}094$	1.52 ± 0.02	0.62 ± 0.03	-0.73 ± 0.01
5[e]	$18^{\rm h}19^{\rm m}30\overset{\rm s}{.}489$	$-20°36'51\overset{''}{.}315$	1.82 ± 0.05	1.03 ± 0.03	-0.46 ± 0.02
6[d]	$18^{\rm h}19^{\rm m}08\overset{\rm s}{.}862$	$-20°32'00\overset{''}{.}286$	21.63 ± 1.5	8.13 ± 0.04	-0.80 ± 0.06

Notes.
[a]Derived from a Gaussian fit
[b]IRAS 18162 − 2048
[c]HH 80N
[d]Sources with position outside the field of view of Fig. 2.3
[e]New reported source

In order to test this possibility we extrapolated the expected path of the jet measured by Martí et al. (1993). They found that the different radio knots of the HH 80/81/80N radio jet are not completely aligned but rather follow a shape compatible with a precessing jet. We used the sinusoidal expression, $y = \tan(\theta/2)\sin(x/\lambda)$, to represent the path of the jet, where θ is the precession angle, λ is the wavelength of the jiggling, and x and y are orthogonal coordinates in the sky being x parallel to the jet main axis. We found that the extrapolated sinusoidal path derived by Martí et al. (1993) ($\lambda = 900''$, $\theta = 7°$) misses Source 5 by about $20''$ (see blue dotted line in Fig. 2.4). However, considering a phase shift of -60° with respect Martí et al. (1993) (i.e. adding this value to the phase of the sin function of the above expression), Source 5 appears close to the jet path (see red dotted line in Fig. 2.4).

2.3 Brief discussion

Assuming that HH 80N is the northern end of the HH 80/81/80N jet moving with a constant projected velocity of 700 km s^{-1}, Martí et al. (1993) derived a dynamical age of the jet of $\sim$ 5500 yr for the jet. Since the estimated age of IRS1 is $\sim 2\times10^4$ yr

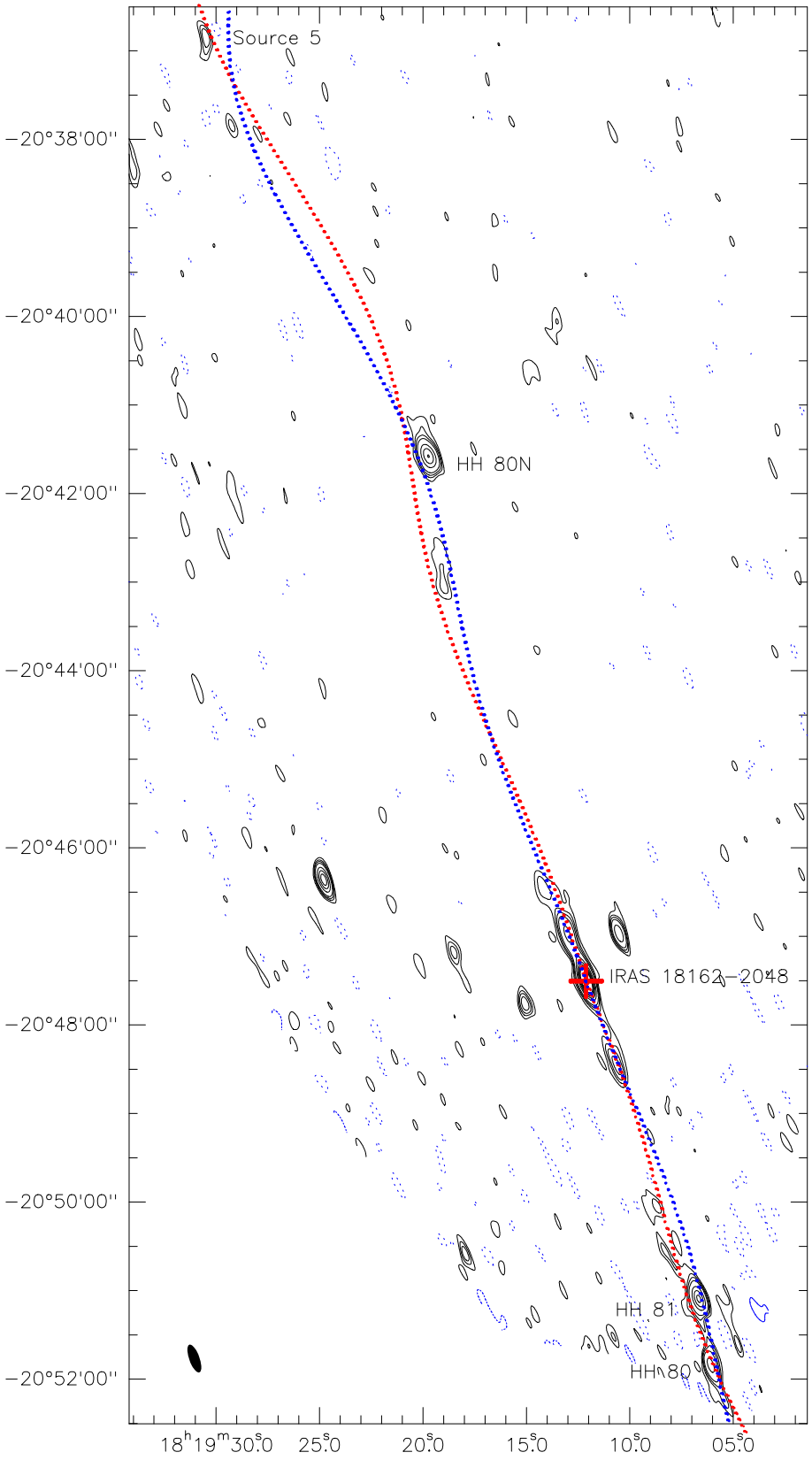

Figure 2.4: Fit of a precessing jet to the knots of the HH80/81/80N complex overimposed over the C band map obtained with the C configuration. The blue dotted line shows the precessing jet path derived by Martí et al. (1993). The red dotted line shows the precessing jet path using the same parameters values of Martí et al. (1993) but adding a phase shift of -60°.

(see Chapter 4), about a factor of 5 older than the jet, the possible influence of the jet in the dynamics of the molecular core (e.g. by triggering the star formation) seems unlikely.

However, this conclusion can change if we consider the possibility that Source 5 belongs to the HH 80/81/80N jet. Assuming the same tangential velocity for the northern source as for HH 80N, the dynamical age of the jet increases about a factor of two, 1.1×10^4 yr . Furthermore, in some flows, the mean velocities of HH objects decrease with increasing projected distance from the source, resulting in dynamical ages up to 10^5 yr (Reipurth et al. 1997; Devine et al. 1997). If this is the case of the HH 80/81/80N jet, its influence on the formation of IRS1 would be then possible. Regardless this possibility, the HH 80N core was a condensation, probably starless, already existing before the HH 80N/81/80N jet arrival (see Chapter 6).

Chapter 3

The molecular emission of the HH 80N core

3.1 Introduction

In recent years, observations show that a number of HH objects have associated molecular condensations (Rudolph and Welch 1988; Davis et al. 1990; Torrelles et al. 1992, 1993; Girart et al. 1994, 1998, 2002, 2005; Viti et al. 2006; Whyatt et al. 2010). These clumps do not show evidence of shock heating as indicated by their narrow linewidths ($\leq$ 1 kms), low temperatures ($<$ 20 K) and radial velocities close to the ambient cloud velocity (e.g. Whyatt et al. 2010), which rules out the possibility of a dynamical perturbation. However, BIMA observations towards the HH 2 region reveal that despite the generally quiescent nature of the molecular condensations ahead of the HH objects, complex dynamical and radiative interactions occur in this region (Girart et al. 2005).

In a scenario proposed by Wolfire and Koenigl (1993) and extensively modeled by Taylor and Williams (1996) and Viti and Williams (1999a), the molecular clump is exposed to a strong UV radiation generated in the HH objects. This radiation is capable of evaporating icy mantles of dust grains, triggering a non-equilibrium chemistry that leads to an increase in abundance of specific molecular species (e.g. CH_3OH, NH_3, HCO^+). Possibly, the nature of the clumps found ahead of HH objects is transient and they will most likely disperse afterwards. Similar clumps with derived masses well below the virial mass were found by Morata et al. (2005)

in L673, supporting the idea that molecular clouds are formed by small transient clumps. The clumps ahead of HH objects may belong to the same population as these transient clumps but they exhibit different chemistry because they are photoilluminated. The chemical properties of the HH 80N core suggest that it is one examples of irradiated core (Girart et al. 1994, 1998), but it is significantly larger and more massive than other molecular condensations observed ahead of HH objects, which have typically sizes and masses $\simeq 0.1$ pc and $M \simeq 1\ M_{\odot}$, respectively. In addition, the HH 80N core shows star formation signatures with supersonic infall velocity suggesting that this core has a different nature than other cores found ahead of HH objects (Girart et al. 2001).

In this chapter we present a study of the emission of different molecular species observed in the HH 80N core with the BIMA interferometer. Our aim is to characterize the properties of the emission for different molecular tracers and to establish their differences from the CS (2–1) emission analyzed in Girart et al. (2001). We also attempt to provide some possible explanations for the origin of these observed differences by means of a qualitative comparison with other regions, considering the nearby location of the HH 80N object to the HH 80N core. In § 2.2 we present our observations. Their analysis is shown in § 2.3 In § 2.4 we discuss the results. Finally, in § 2.5, we summarize our conclusions.

3.2 Observations

The 10-antenna BIMA array observations were carried out between November 1999 and May 2001. The phase calibrator used was the QSO J1733−130 and the flux calibrators were Mars, Uranus or Neptune depending on the epoch. A total of 12 frequency setups were used, one at 218.2 GHz and the rest covering frequencies between 85.1 and 109.8 GHz. All the frequency setups were observed in the C configuration apart from the 93.1 GHz frequency setup which was observed in the D configuration. The C configuration had baselines between 6.3 to 100 m, providing an angular resolution of $\sim 5''$ and $\sim 9''$ at 1 mm and 3 mm, respectively. The D configuration had baselines between 6.3 and 30 m, providing an angular resolution of $\sim 25''$ at 3 mm. Each frequency setup has upper and lower frequency bands. The digital correlator was configured to sample part of the 800 MHz wide IF passband in several windows. The typical window for the line observation was configured

Table 3.1: Characteristic Values of BIMA Channel Maps.

Transition	ν (GHz)	Observed configuration	Beam[a] (arcsec×arcsec)	PA (deg)	rms (Jy beam^{-1})	Δv_{ch} (km s^{-1})	Peak emission[b] (Jy beam^{-1})
HCO^+ (1–0)	89.1885	C	14.1 × 6.9	1.2	0.13	0.33	3.65
HCN (1–0)	88.6319	C	14.2 × 6.7	1.7	0.13	0.33	1.55
C_3H_2 ($2_{1,2}$–$1_{0,1}$)	85.3389	C	14.7 × 7.0	1.8	0.13	0.34	0.87
CS (2–1)	97.9810	C	15.6 × 7.1	3.0	0.18	0.30	2.36
$C^{18}O$ (1–0)	109.7822	C	13.9 × 6.5	−2.9	0.29	0.27	2.77
SO (2_3–1_2)	109.2522	C	14.2 × 6.6	−2.0	0.24	0.40	≤0.72
SO (2_1–1_1)	86.7543	C	18.1 × 7.8	0.6	0.15	0.58	≤0.45
SO (3_2–2_1)	99.2999	C	15.6 × 7.2	0.7	0.21	0.29	3.05
SO (5_5–4_4)	215.2207	C	7.8 × 3.8	−2.4	0.93	0.41	≤2.79
CH_3OH (2_n–1_n)	96.7414[c]	C	16.9 × 7.5	−6.0	0.18	0.30	1.33
N_2H^+ (1–0)	93.1738[d]	D	32.1 × 18.8	10.0	0.73	0.16	6.01
$H^{13}CO^+$ (1–0)	86.7543	C	16.2 × 7.6	2.0	0.16	0.34	0.99
C_2S (6_7–5_6)	86.1841	C	17.2 × 7.9	1.1	0.12	0.58	≤0.36
SiO (2–1)	86.8461	C	18.1 × 7.9	−0.8	0.12	0.32	≤0.36
HCOOH ($4_{0,4}$–$3_{0,3}$)	89.5792	C	17.6 × 7.8	−0.9	0.16	0.55	≤0.48
H_2CS ($3_{0,3}$–$2_{0,2}$)	103.0404	C	14.5 × 6.2	2.0	0.15	0.57	≤0.45
H_2CO ($3_{0,3}$–$2_{0,2}$)	218.2222	C	7.7 × 3.7	−9.5	0.94	0.40	≤2.82
Continuum (1.3 mm)	217.0	C	7.3 × 3.0	−4.5	0.016	...	0.061
Continuum (3.1 mm)	99.5	C	15.5 × 6.8	−6.7	0.004	...	≤0.012

Notes.

[a] A taper function of 4″ was used in all the channel maps except for $C^{18}O$(1–0) (2.0″), SO(5_5–4_4) (2.5″), SiO(2–1) (2.0″),H_2CS(3_{03}–2_{02}) (2.0″), H_2CO(3_{03}–2_{02}) (2.5″) and continuum (1.4 mm) (1.0″) maps.

[b] Upper limits are three times the rms.

[c] Frequency for the 2_0–1_0–A line. The 2_{-1}–1_{-1}–E line was also detected.

[d] Frequency for the F_1 F=2 3–1 2 hyperfine line. All the hyperfine 1–0 components were detected.

with a 25 MHz bandwidth and 256 channels, giving a spectral resolution typically of $\sim$ 100 kHz, which corresponds to a velocity resolution of $\sim$ 0.15 km s^{-1} and $\sim$ 0.3 km s^{-1} observing at 1 mm and 3 mm, respectively. For the continuum maps, typical windows of 0.1 GHz divided in 32 channels were used.

The phase tracking center of the observations was set at $\alpha(J2000) = 18^h19^m18\overset{s}{.}618$ and $\delta(J2000) = -20°40'55\overset{''}{.}00$. The data were calibrated using the MIRIAD package. Maps were made with the visibility data weighted by the associated system temperature and using natural weighting. Different taper functions were used to improve the signal-to-noise ratio depending on the transition. Table 5.2 lists characteristic parameters of channel as well as continuum emission maps. The table gives the frequency of the transition, the resulting synthesized beam, the channel resolution and the rms noise of the maps at the channel resolution.

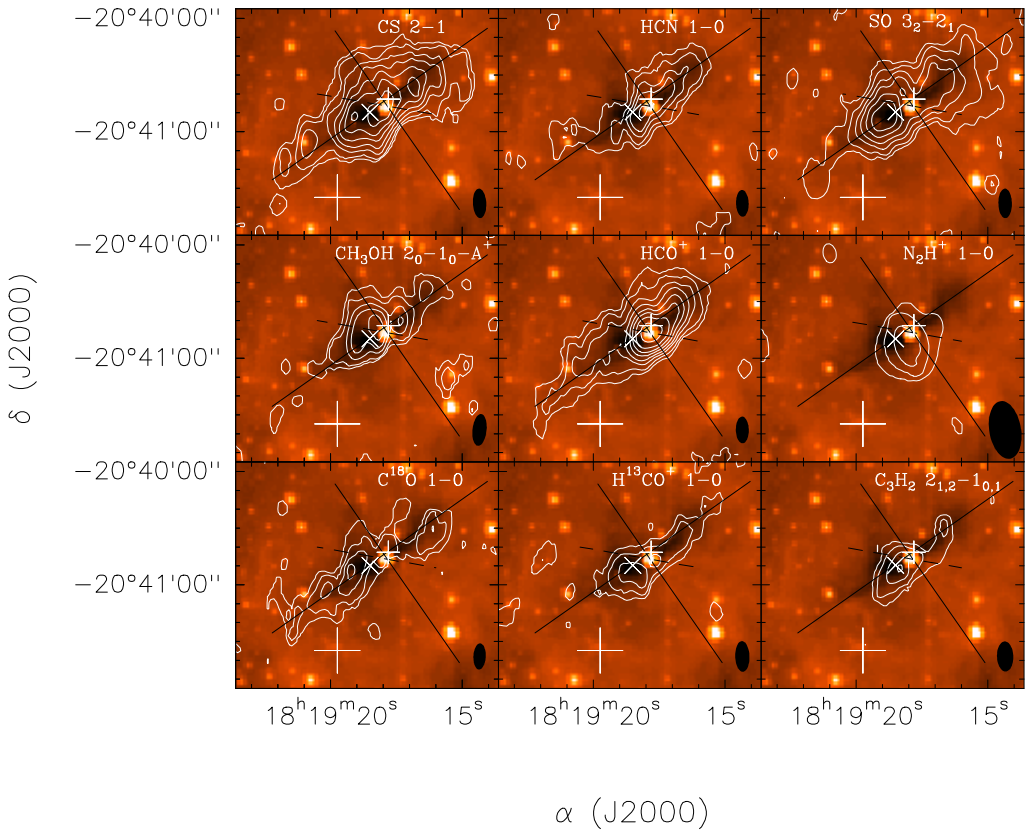

Figure 3.1: Superposition of the *Spitzer* image (8 μm; color scale) and the zero-order moment (integrated emission; white contours) over the 9.5–14.09 km s^{-1} velocity range of the species detected with BIMA in the HH 80N core. The *Spitzer* image shows the HH 80N core in absorption of the background emission (black color). The contour levels are 2, 4, 7, 10, 14, 18, 23, and 30 times 0.14 (CS and SO), 0.11 (HCN, CH_3OH and HCO^+), 0.1 ($H^{13}CO^+$ and C_3H_2), 0.17 ($C^{18}O$) and 0.40 (N_2H^+) Jy beam^{-1} km s^{-1}. The beam is shown in the bottom right corner in each panel. The large and small crosses mark the HH 80N object and the continuum peak at 1 mm, respectively. The tilted cross marks the NH_3 peak (Girart et al. 1994). The solid lines represent the minor (P.A. = 32°) and the major (P.A. = 122°) axis of the core. The dashed line gives approximately the orientation and extension of the outflow detected by (Girart et al. 2001) (P.A. $\sim$ 80°). The central bright source is likely associated with the source powering the molecular outflow.

3.3 Results and analysis

Table 5.2 lists the transitions (excluding hyperfine components) of all the detected molecules: $C^{18}O$, HCO^+, $H^{13}CO^+$, HCN, CS, SO, N_2H^+, C_3H_2 and CH_3OH. The Table also lists the transitions of several molecules that were undetected, among them SiO and H_2CO. The 1.4 mm continuum emission was detected marginally with a flux density of 61 ± 16 mJy, peaking at $\alpha(J2000) = 18^h19^m17\overset{s}{.}81$ and $\delta(J2000) = -20°40'42\overset{''}{.}70$, while no continuum emission was detected at 3.1 mm with an upper limit of $\sim$ 12 mJy beam^{-1} (at the 3–σ level). Very Large Array 2 cm continuum observations with the D configuration (beamsize $8.1'' \times 4.9''$) do not show emission towards the 1.4 mm continuum peak up to 0.27 mJy beam^{-1} (at the 3–σ level) (Martí et al. 1993). The combination of 2 cm and 1.4 mm flux density yields $\alpha \geq 1.8$ where α is defined as $S_\nu \propto \nu^\alpha$, being S_ν the flux density at frequency ν. This lower limit value obtained for the spectral index is clearly compatible with having thermal dust emission. Figure 3.1 shows the integrated emission of the detected lines superimposed on the 8 μm *Spitzer* image retrieved from the *Spitzer* archive. For reference, we define the bright central source seen in the 8 μm *Spitzer* image as the core center ($\alpha(J2000) = 18^h19^m17\overset{s}{.}81$ and $\delta(J2000) = -20°40'47\overset{''}{.}74$).

As seen in Fig. 3.1, all the detected molecules (except for N_2H^+) present an elongated structure with a position angle of $\sim 120°$ (i.e. the direction of the major axis) following approximately the same morphology revealed by the dark lane seen in the 8 μm *Spitzer* image. Clearly, the CS is the most extended molecular tracer showing half-power angular dimensions of $60'' \times 25''$. SO, HCN and HCO^+ behave similarly to CS showing approximately the same angular size, while CH_3OH, $C^{18}O$, $H^{13}CO^+$ and C_3H_2, present smaller sizes, typically $50'' \times 15''$.

Figure 3.2 shows the channel maps for the different species over the $\sim$10.5 km s^{-1} to $\sim$13.1 km s^{-1} velocity range. The 1.4 mm continuum emission is included in the last row of this figure. The emission of most of the species has a clumpy morphology with different substructures along the core. As mentioned above, Girart et al. (2001) analyzed the CS (2–1) emission and found that the flattened structure is consistent with a ring-like structure seen edge on. Thus, on basis of this result and for clarity, we divided the core in the different parts of the ring analyzed by Girart et al. (2001), plus some other structures.

The features indicated in the first row of Fig. 3.2 belonging to the ring are:

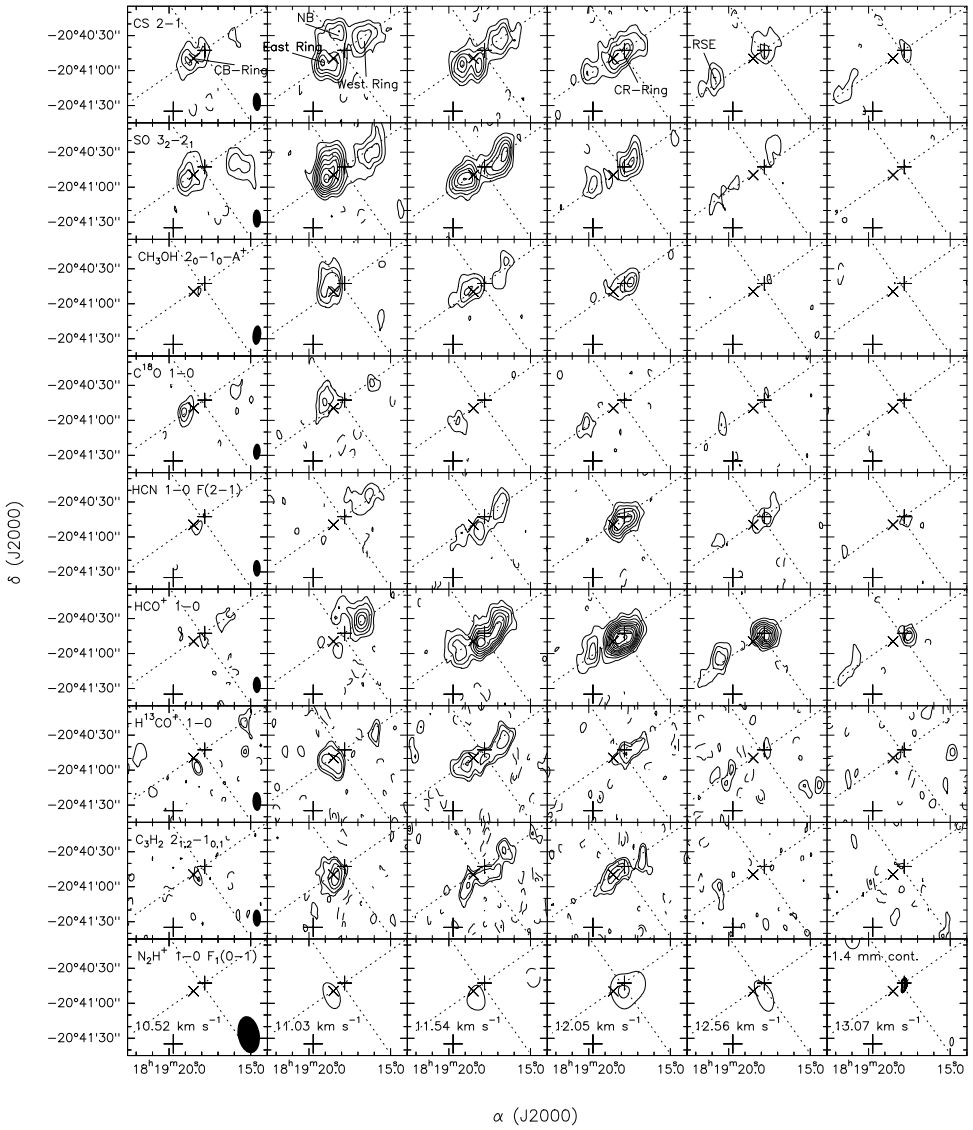

Figure 3.2: Channel velocity maps of the species shown in Fig. 3.1 over the 10.5 km s^{-1} to 13.0 km s^{-1} velocity range with a velocity resolution of ~ 0.5 km s^{-1}. The level contours are -3, 3, 5, 7, 9, 11, 13, 15, 18, and 21 times the rms noise level for each species. For $H^{13}CO^+$ and C_3H_2 the contours -2 and 2 times rms are also shown. The labels shown in the first row indicate the parts of the ringlike morphology (see Section 3.3) as well as other structures. The thick solid contour shown in the bottom right panel represents the two times the rms of the 1.4 mm continuum emission. The beam for each species (filled ellipse) is shown in the bottom right corner of the panels of the first column. The beam of the 1.4 mm continuum emission (open ellipse) is shown in the bottom right corner of the bottom right panel. The symbols are the same as in Fig. 3.1.

(1) the eastern side of the ring that appears as a clump seen at 11.0–11.5 km s^{-1} (hereafter we will call this component East Ring); (2) the western side of the ring, that consists of a clump visible at the same velocities as the East Ring (hereafter, West Ring); (3) the red-shifted side of the ring that is seen at 12 km s^{-1} as a clump spatially coincident with the core center (hereafter, CR-Ring); (4) in addition, we define the blue-shifted side of the ring at the center of the core as the CB-Ring, seen in 10.52 km s^{-1} channel. The other features that do not seem to belong to the ring are: (5) the eastern elongated structure found at red-shifted velocities, 12.6–13.1 km s^{-1}, eastwards of the East Ring structure (hereafter, RSE, following the nomenclature used in Girart et al. 2001); (6) the northern blue-shifted clump seen only at 11 km s^{-1} (hereafter, NB). This nomenclature will be followed in the forthcoming analysis.

The inspection of channel maps of Figure 3.2 reveals an interesting differentiation between molecular tracers. In addition, the kinematic complexity becomes evident along the major axis of the core. The molecules can be grouped according to the morphology of their emission:

(a) CS, SO and CH_3OH. CS and SO are characterized by having the brightest emission in the East Ring. They also trace other structures such as the West Ring, the NB and the RSE. CH_3OH shows a similar morphology to CS and SO even though its emission is more compact and it is weaker. In particular, the emission of CH_3OH in the RSE and CB-Ring is very marginal.

(b) HCO^+ and HCN. The strongest emission of these species, especially HCO^+, arises in the CR-Ring where it shows a prominent clump. In addition, these two species trace the RSE structure. However, the peculiarity of this group of species is that they show little or no emission in the East Ring, unlike the rest of species. The emission of $H^{13}CO^+$, the optically thin isotopologue of HCO^+, appears more compact being only significant in the 11.0 to 12.0 km s^{-1} velocity channels. The $H^{13}CO^+$ emission is consistent with the HCO^+ and HCN emission. However, the East Ring shown faintly by HCO^+ and missed by HCN is clearly traced by $H^{13}CO^+$.

The rest of the species exhibit peculiar features and can not be included in any group: the emission of C_3H_2 is quite similar to that of $H^{13}CO^+$ and traces all the structures except RSE and NB. On the other hand, $C^{18}O$ only traces the East Ring and the RSE structures. Finally, the N_2H^+ emission is significantly more compact than the other species not only due to the poor angular resolution, but to the poor

signal-to-noise ratio of the observations that would prevent us from detecting any extended emission.

3.3.1 Analysis of the morphology and kinematics

To better study the kinematic signatures as well as the morphological differences between the detected species, we performed a set of position-velocity (PV) plots along the major (P.A. = 122°) and minor (P.A. = 32°) axis of the core. Subsequently, we analyzed the properties of the emission for the different species by modeling the emission as an optically thin and uniform contracting ring-like structure. This model has been found to fit well the CS emission (Girart et al. 2001). The model consists, basically, in a spatially thin disk seen edge-on. A similar model was first used by Ohashi et al. (1997) to study the emission of the contracting core associated with IRAS 04368 + 2557 in L1527. The parameters of our model are the inner and outer radii of the ring, $R_{\rm in}$ and $R_{\rm out}$, respectively, the infall velocity, $V_{\rm inf}$, and the intrinsic line width ΔV. Our model does not account for rotation because Girart et al. (2001) found it to be negligible ($\leq$ 0.2 km s^{-1}), neither for dynamical infalling, for simplicity. For clarity, we show in Fig. 3.3 a 3D view of the model geometry. This figure indicates the components of the ring defined in § 3, as well as the directions of minor and major axis. Our strategy is to obtain synthetic PV plots in the minor and major axis of the edge-on ring-like structure, and to compare them with the PV plots taken from the data. Although the ring model is assumed to be spatially thin, we convolved the spatial axis of all the PV plots taken from the model with the angular resolution of our observations. A similar procedure was performed in Girart et al. (2001) in their attempt to study the CS emission. The authors obtained an inner and outer radii of $R_{\rm in}$= 23″ and $R_{\rm out}$= 35″ ($\sim$ 4$\times$10^4 AU and $\sim$ 6$\times$10^4 AU, respectively), an infall velocity of $\sim$ 0.6 km s^{-1}, and a line width of 0.8 km s^{-1}. In our analysis, we adopted the same model parameters as Girart et al. (2001) but leaving the inner and outer radii of the ring as free parameters. For consistency, we first analyzed the CS (2–1) data. Once the CS emission is modeled, it becomes a reference for the rest of species. We found a $R_{\rm out}$ of 35″ ($\sim$ 6$\times$10^4 AU) and a $R_{\rm in}$ of 15″ ($\sim$ 2.5$\times$10^4 AU) being the latter value somewhat smaller than that obtained by Girart et al. (2001) . For other species, the use of different values of $R_{\rm in}$ and/or $R_{\rm out}$ does not improve significantly the appearance of the residual PV plots. Thus, in those cases we adopted the same $R_{\rm in}$ and $R_{\rm out}$ as for the CS.

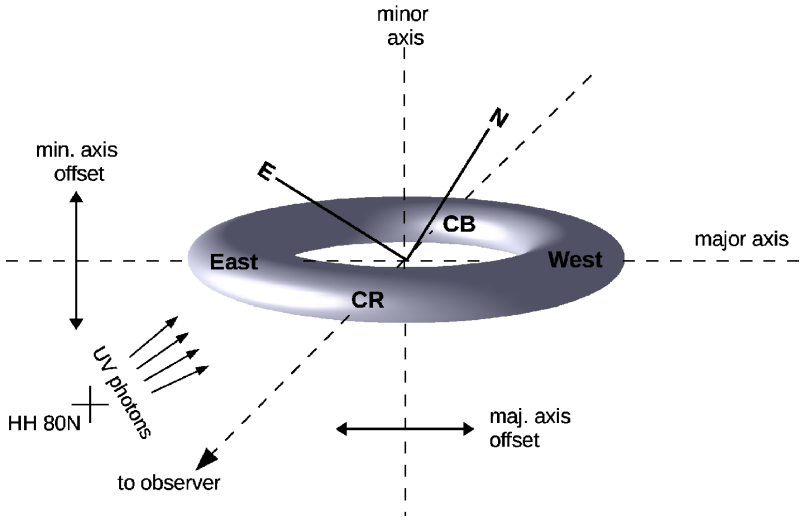

Figure 3.3: Sketch of the model geometry used in the analysis of the PV plots, including a schematic representation of the HH 80N scenario that we propose in order to account for the observed chemistry in the ring components discussed in Section 2.4.2.2. Note that this figure is not plotted to scale.

Figure 3.4 shows the PV plots along the major and minor axis of the emission, as well as the residual PV plots after subtracting the data and the model for several species. It also shows the PV plots of the best fit model ($R_{\rm in} = 15''$ and $R_{\rm out} = 35''$). As found by Girart et al. (2001), the model fits reasonable well the CS emission. However, the PV plots for the other species reveal that they trace the contracting ring–like structure in a non-uniform fashion. The residual PV plots show some of the structures defined above as important features of emission and *absorption* for most species:

- *RSE*. This eastern elongated structure, which is visible in CS, SO, HCO^+, $C^{18}O$ and marginally in HCN, is clearly independent from the contracting ring as pointed out by GEVWH. The RSE exhibits a clear linear velocity gradient with increasing velocity toward the east, i.e., as it gets closer to HH 80N.

- *NB*. It is clearly seen in the PV plots along the minor axis of CS, SO and CH_3OH (and marginally $C^{18}O$). Due to its position ($20''$ east from the emission expected from the ring in the minor axis PV plot) this clump is probably independent from the ring structure.

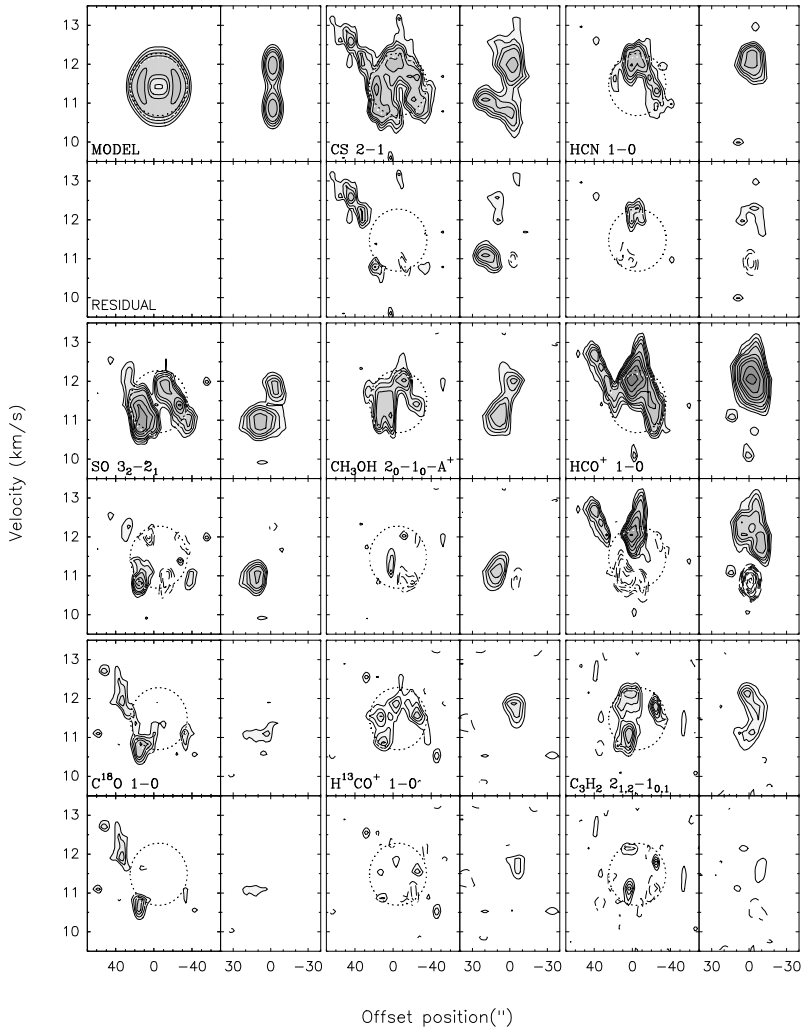

Figure 3.4: Sets of PV plots for *from left to right and from top to bottom*): model, CS (2–1), HCN (1–0), SO (3_2–2_1), CH_3OH (2_0–1_0–A^+), HCO^+ (1–0), $C^{18}O$ (1–0), $H^{13}CO^+$ (1–0) and C_3H_2 ($2_{1,2}$–$1_{0,1}$). For each set, the PV plots of the BIMA data are shown at the top and the residual PV plots resulting from subtracting the data and the model are shown at the bottom. The panels on the left represent the PV plots along the major axis while the panels on the right represent the PV plots along the minor axis of the core. For the set of PV plots obtained from the model, the two panels at the top show the best fit model (see text) for the major (left) and minor (right) axis of the ring-like structure seen in an edge-on view. The positive offsets of the PV plots corresponds to South-East and to North-East directions for the major and minor axis, respectively. The contour levels are -10, -8, -6, -4, -3, 3, 4, 6, 8, 10, 12, 14, 16, and 20 times the rms noise for each species. For $H^{13}CO^+$ and C_3H_2 the contours -2 and 2 times the rms noise have been added. The dashed ellipse, drawn to highlight the best fit model for the major axis, corresponds to a ring with a radius of 30″.

- *East Ring.* It appears as a spot seen in the residual PV plots along the major axis of CS, SO and $C^{18}O$ (and marginally CH_3OH) located at 11 km s^{-1} at the eastern part of the ring. Although its position indicates that the East Ring seems to belong to the ring structure, the residual PV plots show that its emission clearly exceeds the emission generated by the uniform ring model.

- *West Ring.* Contrary to the other structures, the West Ring does not show significant emission in the residual PV plots for almost all the species. Only CS, SO and $C^{18}O$ seem to show marginal emission in the western part of the ring structure. This implies that for the majority of the species the molecular emission cancels out the emission expected for the ring model in this part of the ring.

- *CR–Ring.* The CR-Ring seems to be physically part (at least partially) of the ring structure but it exhibits stronger emission than that expected from the ring model for HCN and, especially HCO^+, as clearly seen in the residual PV plots.

- *CB–Ring.* This structure is visible as negative contours in the residual PV plots for the major and minor axis for most of the species. The CB-Ring component is best traced by CS, but presents an important lack of emission for the rest of species, being most evident for HCO^+.

3.3.2 Relative abundances

Table 3.2 lists the positions that we consider most representative of the structures defined previously. Figure 3.5 shows the spectra of the detected transitions taken in the five selected positions shown in Table 3.2. Note that some of the spectra taken at the center of the core present two velocity components, separated by ~ 1 km s^{-1}. This result, especially evident for CS, is perfectly compatible with the contracting ring-like morphology found previously for the core and, in fact, these two velocity components appear to coincide with the CB–Ring and CR–Ring components. Another general feature is that the spectra show narrow linewidths, with a FWHM ranging from 0.6 to 1.4 km s^{-1}, that indicates that the gas in the cores is not shocked (typical linewidths found in shocked regions are 6-7 km s^{-1}, e.g. Bachiller et al. 1995).

Table 3.2: Representative Positions.

	Position		
Structure	α (J2000)	δ (J2000)	Map Counterpart[a]
RSE	$18^h19^m21\overset{s}{.}10^a$	$-20°41'15\overset{''}{.}0^a$	CS (2–1) > 12 km s^{-1} eastern elongation
NB	$18^h19^m18\overset{s}{.}10$	$-20°40'26\overset{''}{.}9$	CS (2–1) 11 km s^{-1} northern peak
East Ring	$18^h19^m19\overset{s}{.}03$	$-20°40'53\overset{''}{.}0$	SO (3_2–2_1) 11 km s^{-1} eastern peak
CB-Ring & CR-Ring	$18^h19^m17\overset{s}{.}81$	$-20°40'47\overset{''}{.}7$	HCO^+ (1–0) 12 km s^{-1} center peak
West Ring	$18^h19^m16\overset{s}{.}57$	$-20°40'31\overset{''}{.}5$	CS (2–1) 11 km s^{-1} western peak

Notes.

[a] Molecule used to better highlight the structure.

From the spectra of Fig. 3.5 we derived the column densities in all the components. To do so, we used RADEX, a non-LTE excitation and radiative transfer code that can provide us constraints on the gas density, kinetic temperature and/or the column density (van der Tak et al. 2007). RADEX was used adopting the temperature of 17 K, which is close to the rotational temperature obtained from ammonia (Girart et al. 1994). We used the HCO^+ (3–2) and $H^{13}CO^+$ (3–2) lines observed by Girart et al. (1998) in combination with the $H^{13}CO^+$ (1–0) (smoothed to the CSO angular resolution) of our dataset to constrain the range of possible values for the average gas density. In this calculation, we performed line intensity ratios of these lines assuming a comparable beam dilution. Then, we ran RADEX exploring the densities that yield brightness temperatures ratios compatible with our measured values (within a 20 per cent range due to uncertainties).

We found a range of 5×10^4 – 1.3×10^5 cm^{-3} of possible values for the average gas density in the core. Once the possible density range is constrained and the kinetic temperature fixed, using RADEX again we were able to search for the column density range that yields the line intensities measured in the spectra of Fig. 3.5. For the HCO^+, the column density was derived using the optically thin isotopologue $H^{13}CO^+$ and adopting an abundance carbon isotope abundance ratio, C^{12}/C^{13}, of 63 (Langer and Penzias 1990, 1993). The results are presented in Table 3.3.

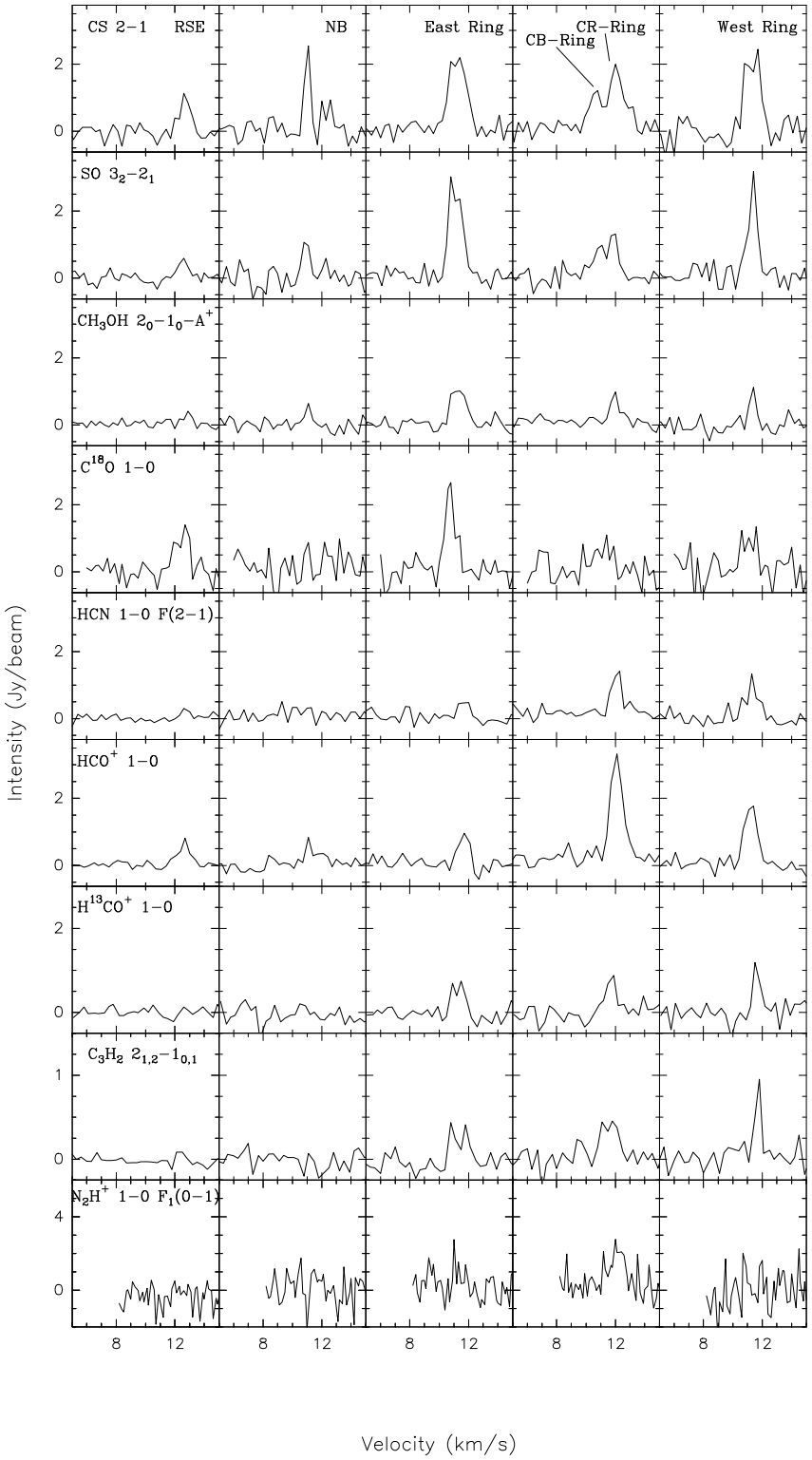

Figure 3.5: Spectra of (*from top to bottom*) CS (2–1), SO (3_2–2_1), CH_3OH (2_0–1_0)-A^+, $C^{18}O$ (1–0), HCN (1–0, F(2–1)), HCO^+ (1–0), $H^{13}CO^+$ (1–0), C_3H_2 ($2_{1,2}$–$1_{0,1}$), and N_2H^+ (1–0, F_1(0–1)) towards (*from left to right*) RSE, NB, East Ring, CB-Ring, CR-Ring, and West Ring components given in Table 3.2. For RSE, the spectra were obtained for a box of $\sim 15'' \times 25''$.

Table 3.3: Column Densities[a] (in units of 10^{13} cm^{-2})

Molecule	CS		SO		CH_3OH[b]		HCN		HCO^+[c]		C_3H_2		$C^{18}O$	
	N_m	N_M	N_m	N_M	N_m	N_M	N_m	N_M	N_m	N_M	N_m	N_M	N_m	N_M
RSE	0.9	0.5	1.2	0.7	≤ 1.8[d]	≤ 2.1[d]	0.6	0.3	≤ 2.5[d]	≤ 1.8[d]	≤ 0.2[d]	≤ 0.1[d]	171	180
NB	2.2	1.0	2.1	1.1	≤ 3.0[d]	≤ 3.4[d]	≤ 1.0[d]	≤ 0.5[d]	≤ 2.2[d]	≤ 1.6[d]	≤ 0.5[d]	≤ 0.2[d]	≤ 154[d]	≤ 162[d]
East Ring	4.6	2.4	13.6	6.4	10.0	11.4	1.8	0.7	7.2	5.1	0.8	0.4	280	293
CB-Ring	1.2	0.7	2.1	1.2	≤ 2.6[d]	≤ 2.9[d]	≤ 1.2[d]	≤ 0.5[d]	≤ 4.8[d]	≤ 3.4[d]	≤ 0.5[d]	≤ 0.3[d]	≤ 123[d]	≤ 130[d]
CR-Ring	2.8	1.5	3.1	1.7	2.7	3.1	6.6	2.2	6.9	4.7	0.5	0.2	≤ 123[d]	≤ 130[d]
West Ring	4.1	2.1	8.7	4.0	5.1	5.8	6.2	2.2	9.1	6.0	1.0	0.5	166	175

Notes.
[a] N_m and N_M are the column densities derived for the lower (5×10^4 cm^{-3}) and upper (1.3×10^5 cm^{-3}) values of the density range derived from the RADEX analysis (see § 3.3.2).
[b] Including CH_3OH-A and CH_3OH-E.
[c] Derived from $H^{13}CO^+$.
[d] Upper limits are 3 times the rms noise.

Table 3.4: Relative Abundances with Respect to CS[a]

Molecule	SO		CH_3OH[b]		HCN		HCO^+		C_3H_2		$C^{18}O$	
	X_m	X_M	X_m	X_M	X_m	X_M	X_m	X_M	X_m	X_M	X_m	X_M
RSE	1.3	1.3	≤ 2.0[c]	≤ 4.0[c]	0.7	0.5	≤ 2.7[c]	≤ 3.4[c]	≤ 0.2[c]	≤ 0.2[c]	190	346
NB	1.0	1.1	≤ 1.4[c]	≤ 3.3[c]	≤ 0.5[c]	≤ 0.4[c]	≤ 1.0[c]	≤ 1.6[c]	≤ 0.2[c]	≤ 0.2[c]	≤ 72[c]	≤ 157[c]
East Ring	3.0	2.7	2.2	4.8	0.4	0.3	1.6	2.2	0.2	0.2	61	125
CB-Ring	1.7	1.7	≤ 2.1[c]	≤ 4.1[c]	≤ 1.0[c]	≤ 0.7[c]	≤ 4.0[c]	≤ 4.8[c]	≤ 0.5[c]	≤ 0.4[c]	≤ 103[c]	≤ 183[c]
CR-Ring	1.1	1.2	1.0	2.1	2.4	1.5	2.5	3.2	0.2	0.2	≤ 45[c]	≤ 89[c]
West Ring	2.1	1.9	1.3	2.7	1.5	1.0	2.2	2.8	0.3	0.2	40	83

Notes.
[a] X_m and X_M are the abundance values derived for the lower (5×10^4 cm^{-3}) and upper (1.3×10^5 cm^{-3}) limits of the density range derived from the RADEX analysis (see § 3.3.2).
[b] Including CH_3OH-A and CH_3OH-E.
[c] 3–sigma upper limits.

In order to clarify the scenario that leads to the chemical properties observed in each structure we computed the relative abundances with respect to CS. The reason for adopting such a scale is that CS appears to be the most fiducial molecule since its chemistry seems to be directly related to dense gas. In fact, it is the molecule that more regularly traces the contracting edge-on ring. In addition, as the lines involved in this analysis were taken with the same configuration and beam sizes, then the missing flux effects are probably canceled out. Another advantage of using the molecular abundances relative to CS is that most of the observed transitions have a high critical density similar to CS (2–1) and, hence, they trace approximately the same gas (with the possible exception of $C^{18}O$). The resulting ranges of fractional abundances with respect to CS corresponding to the density range derived above are shown in Table 3.4.

We also calculated the logarithmic median and the standard deviation of the relative abundances for the same molecules detected in the HH 80N clump over a sample for three types of environments related with dense gas: molecular clumps associated with HH objects, low-mass star-forming cores and dark molecular clouds. Figure 3.6 shows the comparison of the fractional abundances of these three types of environments with the values of Table 3.4.

The description of the chemical properties seen in Fig. 3.6 led us to classify the observed molecules depending on the variability of their relative abundances between the different components of the core:

(a) $C^{18}O$ is the molecule that presents the major variability between components. It exhibits a notoriously high relative abundance with respect to CS towards RSE (between a factor of 2 to 5 with respect to the rest of components) although it is undetected or has low relative abundances in the rest of the components.

(b) SO, CH_3OH and HCO^+ have their abundances higher than CS but presents a moderate variability. The comparison between their relative abundances with respect to CS in the different components of the core for the different species in this group never exceeds a factor of 3. There is, however, a difference between the molecules in this group: while SO and CH_3OH relative abundances are maximum at the East Ring position, HCO^+ presents the highest abundances towards CR-Ring and West Ring.

(c) C_3H_2 and HCN exhibit a moderate variability and each molecule shows a dis-

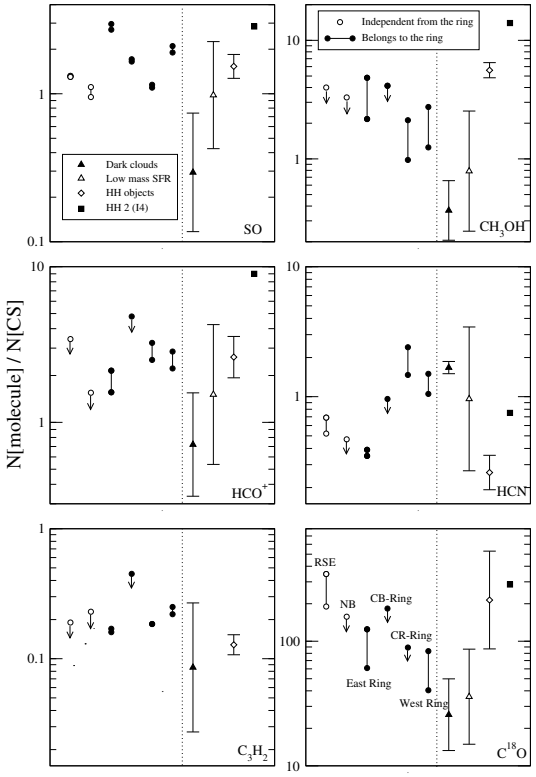

Figure 3.6: Relative molecular abundances (with respect to CS) for (*from left to right and from top to bottom*) SO, CH_3OH, HCO^+, HCN, C_3H_2 and $C^{18}O$. In each panel the circles represent the structures found for the HH 80N region: (from left to right) RSE, NB, East Ring, CB-Ring, CR-Ring and West Ring,and the bars between circles represent the range of relative abundances derived from the possible averaged density range for the core (see § 3.2). The rest of the symbols and the bars represents the logarithmic median and the standard deviation, respectively, of the relative molecular abundances for each sample (from left to right): dark clouds (i.e. without star formation activity), low–mass star–forming cores, regions close to HH objects, and I4 is a position close to HH 2 (Girart et al. 2005). The sample for the quiescent dark molecular clouds is OMC-1N (Ungerechts et al. 1997), TMC-1 (Pratap et al. 1997), L1498 and L1517B (Tafalla et al. 2006), L1544 and L1689B (Jørgensen et al. 2004), and B68 (Di Francesco et al. 2002) The sample for the low mass star forming molecular clouds is: IRAS 16293−2422 (van Dishoeck et al. 1995), NGC 1333 IRAS 4A (Blake et al. 1995), IRAS 05338−0624 (McMullin et al. 1994), Serpens S68 (McMullin et al. 2000), several cores from Jørgensen et al. (2004) and Schöier et al. (2002), and CH_3OH data from Maret et al. (2005). The sample of the regions close to HH objects is: HH 2 (Girart et al. 2005), HH 1, several positions towards HH 7-11, and HH 34 (Viti et al. 2006). The HH 2 data were taken in the SO_2 clump (see Girart et al. 2005).

tinct behavior. Clearly, C_3H_2 is poorly detected along the core. On the other hand, as seen in § 3, HCN has a similar morphology as HCO^+. Since both molecules have comparable dipole moments, the HCN emission may be considerably self-absorbed, similarly as HCO^+. Therefore, HCN relative abundances are likely underestimated in most components of the core.

3.4 Discussion

3.4.1 Star formation activity within the core

This work presents the results of a molecular survey carried out with BIMA towards HH 80N, for which the CS and CO data were already reported in GEVWH. From the CS data, Girart et al. (2001) detected an elongated dense core with 0.24 pc of radius seen edge on. The properties of the CS emission suggested that it was tracing a ring structure contracting with a striking supersonic infall velocity (0.6 km s^{-1}). The central 'hole' of the ring is presumably the result of molecular depletion due to the high central density that might be reached in this core. From the CO data, Girart et al. (2001) found a bipolar outflow that is a signpost of an ongoing star forming process in the core. The *Spitzer* 8 μm and the BIMA 1.4 mm dust images show a bright source located at the center of the bipolar CO outflow. This strongly suggests the presence of an embedded protostellar object within the core, which powers the bipolar outflow.

The CS emission was used in Girart et al. (2001) to derive the mass of the ring structure. Their obtained value, which is 12 $M_\odot$ assuming $X(\mathrm{CS}) = 2\times10^{-9}$ (10 $M_\odot$ belonging to the main core, and 2 $M_\odot$ to RSE), is somewhat lower than the value obtained from NH_3 (20 $M_\odot$, Girart et al. 1994). The 1.4 mm continuum emission is barely resolved, which implies that it arises from a region with a size of $\sim 10^4$ AU in diameter. The mass of the dust can be estimated using the formula

$$M_d = \frac{S_{1.4} D^2 c^2}{2kT_{\mathrm{d}}\nu^2 k_{1.4}} \tag{3.1}$$

where $S_{1.4}$ is the continuum flux measured at 1.4 mm, D is the distance to the source, T_{d} is the dust temperature, and $k_{1.4}$ is the mass opacity coefficient at 1.4 mm. In our calculations we assume a $k_{1.4}$ of 0.96 cm^2 gr^{-1} for a density of $n_{\mathrm{H_2}} \simeq 10^6$ cm^{-3}

(Col. 2 in Table 2 of Ossenkopf and Henning 1994) and a temperature range of 20–40 K Jennings et al. 1987, which is among the temperatures expected from classical theoretical models of protostellar envelopes (e.g. Adams and Shu 1985). Note that this expression uses the Rayleigh-Jeans approximation, valid at millimeter wavelengths. For our values the mass of the dust is 0.016-0.031 $M_{\odot}$. Adopting a gas-to-dust ratio of 100, the total mass of the envelope traced by the dust emission is 1.6-3.1 $M_{\odot}$

Bontemps et al. (1996) found a relationship between the outflow momentum flux, the envelope mass and the bolometric luminosity. Girart et al. (2001) found that the envelope mass was almost an order of magnitude higher than the values predicted by Bontemps et al., for the measured CO momentum flux. However, Bontemps et al. derived the mass of the envelope for the sources in their sample by integrating the 1.4 mm emission over a region corresponding to $\sim$ 0.05 pc (10^4 AU), whereas Girart et al. (2001) used the mass derived from the CS emission, which traces a region with a radius of 0.24 pc. The derived mass from the 1.4 mm dust corresponds to a region of size approximately similar to that used in Bontemps et al. Thus, if we use the total mass of the envelope derived from the 1.4 mm flux, then the relationship between the envelope mass and the CO outflow momentum flux fits very well.

The study of the circumstellar mass surrounding the YSOs at several radii is a useful tool to track their evolution (e.g. Andre and Montmerle 1994). Class 0 YSOs are best interpreted as very young protostars whose dense circumstellar envelope still contains an important reservoir of mass to be accreted. Therefore the fact that the bulk of the mass of the HH 80N core is found at large radii from its central embedded YSO suggests that this object should be at the beginning of the main accretion phase and, hence, it is another signpost of being an extremely young YSO found probably in the Class 0 stage.

3.4.2 Chemical properties

The analysis of the other species of the molecular survey confirms that their morphology is consistent with the ring-like morphology seen in CS, contracting with a supersonic infall velocity ($\sim$ 0.6 km s^{-1}), though this is a first-order result: a more accurate analysis reveals that most of the molecular species, although tracing approximately the same region as CS, show important local differences. This devia-

tion reflects a possible combination effect of excitation, optical depth and molecular abundance, being the latter the most plausible candidate to explain most of the observed differences.

In this section, we attempt a simple discussion on the possible origin of the observed differentiation by means of a qualitative comparison with the chemistry observed in several environments associated with the dense gas. We considered that the chemistry observed in the HH 80N core may be the result of the strong central depletion and the photochemical scenario caused by the UV radiation coming from the HH 80N object, as pointed out by Girart et al. (2001). The second possibility is consistent with the presence of a PDR found by Molinari et al. (2001).

The ring-like morphology and the central depletion

As suggested by Girart et al. (2001), the ring-like structure is likely due to the freeze–out of the molecules onto the dust grains at the inner regions of the core, where high densities are expected. In addition, there is a young protostellar object embedded in the core. Thus, the conditions of the central part of the core should resemble those found in protostellar cores. In this section we analyze the inner structure of the core by comparing it qualitatively with other similar regions.

When modeling the radial variation of molecular abundances in a circumstellar envelope one has to take into account the effects of the central embedded YSO, heating the inner part of the core, which causes partial sublimation of the icy dust mantles (e.g. IRAS 16293-2422: Ceccarelli et al. 2000, Schöier et al. 2002; NGC1333: Maret et al. 2002, 2004; Jørgensen et al. 2005, Bottinelli et al. 2007). However, we do not see any signpost of a warm component (temperatures of several tens of K) in the HH 80N core, which could be due to either the low luminosity or the youth of the YSO, as well as the distance of the region (in other words, the expected warm region is likely highly beam diluted).

Outside the undetected warm inner region, the HH 80N core exhibits a large region where molecules seem to be strongly frozen in the icy mantles, except possibly for NH_3 (Girart et al. 1994) and N_2H^+, molecules that seem to exhibit a more compact emission. Unfortunately, from the analysis of the PV plots we are not able to determine whether other species deplete at different radii from the center of the core than that of CS. In any case, the depletion radius of the HH 80N core

($\sim 2.5\times10^4$ AU) is significantly larger (by 3–4 times) than those obtained for prestellar cores by Tafalla et al. (2006). Because the most dense gas traced by molecular species is expected to be found at the inner radius of the ring, the lower value of the possible range of average densities for the HH 80N core found in § 3.2 (5×10^4 cm^{-3}) can be taken as a lower limit for the density at the depletion radius (i.e. depletion density). As the Class 0 object forming inside the HH 80N core is very young, the core probably still retains the initial conditions for star formation. Hence, there might be some physical connection with the prestellar cores, specially with those that are found on the verge of dynamical collapse. However, the CS is depleted at densities of the order of a few 10^4 cm^{-3} in prestellar cores (Tafalla et al. 2002; Pagani et al. 2005), slightly below the lower limit for the depletion density in the HH 80N core. The large depletion radius and densities found for the HH 80N core suggests high central densities. This could be due to a more evolved stage of the HH 80N core with respect to prestellar cores, favored by its rapid collapse.

Surrounding the "frozen" region, the HH 80N core has a molecular shell or ring-like structure. Since a minimum gas density is required to observe a given molecular transition, the detection of some specific transitions of our dataset can provide an estimation of the lower possible densities of this shell (i.e. at outer radius 6×10^4 AU). In particular, the detection of HCO^+ (1–0) line implies densities higher than 2.4×10^3 cm^{-3} (for which this transition is easily detectable, Evans 1999). In summary ,we conclude that the densities traced by the molecular emission associated with the ring-like structure are above $\sim 2 \times 10^3$ cm^{-3}, reaching values likely higher than 5×10^4 cm^{-3} at the inner radius.

The components of the ring-like structure

In Figure 3.3 we present the most likely scenario as seen by an hypothetical observer. In the following we analyze the enhancement of some species on the basis of this scenario and in the frame of the UV irradiation. Our basic inspection is the effect of the distance of each component with HH 80N. The fact that HH 80N may not lie in the same plane of sky as the core does not affect qualitatively our analysis. Clearly, this picture implies higher photochemical activity in the East Ring and moderate or low photochemical effects for the CR-Ring, West Ring and CB-Ring. In particular, Table 3.3 shows that the column densities of CS, CH_3OH, $C^{18}O$ and SO follow fairy well this trend: most of them are higher in the East Ring than in the West Ring.

One of the most evident results of Fig. 3.6 is that the enhancement of SO in the East Ring component (the closest in projection to HH 80N) resembles that obtained for the clump ahead of the HH 2 jet (Girart et al. 2005) and determined to be due to chemical effects induced by an enhanced radiation field. This trend is also observed for CH_3OH and $C^{18}O$. Figure 3.7 also shows that SO and CH_3OH are higher than the typical range of values of low mass star forming cores. The caveat to this scenario is HCO^+, which presents similar column densities in all the components of the ring (with the exception of CB-Ring) instead of being greater in the East Ring and CR-Ring, as one would expect if the radiation field impinging on the ring were higher than the interstellar radiation field. This result indicates that other parameters, apart from the effect of the distance to HH 80N, also play a role on the chemistry of the core. Clearly, a detailed modeling, which is however beyond the scope of this study, is required in order to characterize the chemistry of the core ahead of HH 80N.

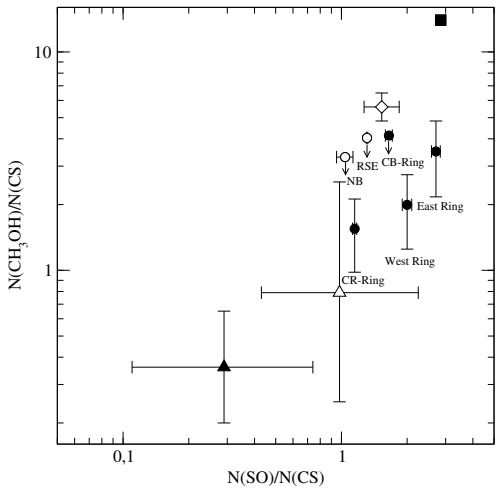

Figure 3.7: CH_3OH vs. SO relative molecular abundances (with respect to CS). The circles represent the structures found for the HH 80N region and the bars associated with the circles represent the range of relative abundances for the density range found in § 3.2. The rest of the symbols and bars are the same as in Fig. 3.6.

Molinari et al. (2001), using a simple model, derived a value of 670 Habing for the FUV field emanating from the recombination region in HH 80N. From this value, only the fraction of photons that impinges to the HH 80N core over the total has to be taken in account. Taking 0.2 pc as the distance between the core and the HH object, and assuming that the core is seen edge on from HH 80N, we obtain a dilution factor of 1/16, which yields $\sim$ 45 Habing for the side of the core facing HH 80N (the East Ring). Interestingly, this value is found within the range of possible values for the radiation field expected to impinge the clump ahead of HH 2 (Viti et al. 2003). However, note that the dilution factor derived above is based on a projected distance. Therefore, its value as well as the estimated FUV are upper limits.

On the other hand, based on the range of average density values estimated in § 3.2, the derived column density through the ring seen from the edge of the core is $N(\mathrm{H_2}) = 2.5 - 6.5 \times 10^{22}$ cm^{-2}. Then, the derived the visual extinction, A_v, from the relationship $N(\mathrm{H_2}) \simeq 10^{21} A_\mathrm{v}$ (Spitzer 1978) is between 25–65 mag, much greater than the values where the photochemical effects are attenuated (e.g. Viti and Williams 1999a) Although HH 80N does not lie exactly on the same plane of the ring, these high extinction values are only approximate and indicate that the UV photons hardly penetrate deeply inside of the core. Therefore, the photochemical effects observed in the East Ring are likely to happen on the "surface" of the ring. This is consistent with the lack of molecular emission at the central region of the core encompassed by the inner radius of the ring.

The decrease of photochemical activity in the parts of the ring further away than the East Ring is possibly a combined effect of geometrical dilution and the presence of low density cloud component. In fact, the distance from HH 80N to the western parts of the ring is a factor of 2-3 greater than to the illuminated side ($\sim$ 0.2 pc), and much larger than the typical distances between other HH objects and their respective associated clumps ($\sim$ 0.05 pc, Viti et al. 2006).

Other molecular clumps in the region

The RSE and NB structures were poorly detected in the species of our survey. Both structures appear to be spatially independent from the ring structure in addition of being smaller. Therefore, these components may present different chemistry simply

because their basic physical structure might be different from the physical structure of the ring. There is, however, an important difference between RSE and NB: while $C^{18}O$ exhibits a high relative abundance with respect to CS in RSE reaching values typical of those found in the HH 2 region (I4 position), it is undetected in NB. In addition, HCO^+ is not enhanced with respect to standard molecular cloud values in NB, implying that the UV radiation does not play a significant role in the chemistry in this structure.

3.5 Conclusions

We have carried out an observational study with the BIMA array of the star forming dense core ahead of HH 80N in order to characterize its morphological and chemical properties. We present maps of the different molecular species detected with BIMA (CS, HCO^+, $H^{13}CO^+$, HCN, CH_3OH, SO, $C^{18}O$, and C_3H_2). These maps reveal a complex morphology and kinematics for this core. In an attempt to understand this complexity, we obtained PV plots for all the species along the major and minor axis of the core and modeled them in a similar procedure as in Girart et al. (2001). Subsequently, we derived the column density and the relative abundances with respect to CS in some selected positions along the core. Our main conclusions can be summarized as follows.

1. The 1.4 mm dust emission was detected marginally in a position close to the *Spitzer* 8 μm source. This source is located at the center of the CO bipolar outflow found by Girart et al. (2001) and, therefore, it is likely its powering source. The 1.4 mm dust emission traces the inner and denser region ($\lesssim 10^4$ AU) of the dense core around the protostar. The mass of the dense core (1.6–3.1 $M_\odot$) at scales up to $\simeq 10^4$ AU and the momentum flux of the CO bipolar outflow correlate well with what is expected for very young Class 0 sources (Bontemps et al. 1996).

2. The integrated emission for most of the molecular tracers reveals a clumpy and elongated morphology with a size of $\sim 60'' \times 25''$ (0.5 pc $\times$ 0.2 pc) and a position angle of $\sim 120°$. Three main structures can be distinguished: the central core around the protostar and two smaller clumps (RSE and NB). As previously observed in CS by Girart et al. (2001), the molecular emission

associated with the central core arises from the outer shell of the dense core. This molecular shell has a ring-like morphology seen edge-on, which is well-traced by CS and partially traced by the other molecular species. The inner and outer radii of the ring are $\sim 2.5 \times 10^4$ and $\sim 6.0 \times 10^4$ AU, respectively, and the estimated averaged density ranges between 5×10^4 and 1.3×10^5 cm^{-3}. The ring structure has been divided in four regions, following the CS clumpy morphology: the East Ring, Central Red-shifted Ring (CR–ring), the Central Blue-shifted Ring (CB–ring) and the West Ring. The kinematics traced by the different molecules is similar to that found for CS by Girart et al. (2001), which is indicative of contraction with a supersonic infall velocity of 0.6 km s^{-1}.

3. The relative abundances with respect to CS derived in different positions were compared with those obtained for a sample of dark clouds, low-mass star-forming cores and other molecular clumps ahead of HH objects. This comparison suggests that the relative abundances of SO, $C^{18}O$ and, slightly CH_3OH, are partially compatible with the high level of UV irradiation generated by HH 80N. In particular, the section of the molecular ring facing HH 80N (East Ring), as well as RSE, seem to be the regions more exposed to the UV radiation, whereas in the other sections of the ring and NB the photochemical effects seem to be less important. The molecular ring has a visual extinction, A_v, between 25 and 65 mag seen from the edge. These values are much higher than the maximum extinction at which the UV radiation can effectively penetrate in the ring and release the molecular species from the dust mantles triggering the photochemistry (Viti et al. 2003). Thus, the photochemical process likely happens on the "surface" of the ring. Inside the molecular ring, at scales of $\lesssim 2.5 \times 10^4$ AU, where extremely high densities are found, the dense core exhibits a "frozen" region, where the observed molecules are significantly depleted onto icy dust mantles.

Chapter 4

A multi-wavelength study of the HH 80N core.

4.1 Introduction

The standard theory of star formation describes the gravitational collapse as an expanding wave that moves outward into the static core and sets the gas into motion toward the central protostar (Shu 1977). This picture provides a good description of protostellar collapse in star-forming regions like Taurus (Motte and André 2001), but some of its predictions are difficult to reconcile with specific observational features. For instance, observations of dense cores show that inward motions can exist already in the prestellar phase (e.g. Tafalla et al. 1998), in contrast to the static initial conditions assumed by the standard theory. The infall velocities inferred in the HH 80N core ($\sim$ 0.6 km s^{-1}), significantly larger than those expected in the standard protostellar collapse (e.g. ambipolar diffusion models predict gas inward motions of a fraction of the isothermal sound speed, $\sim$ 0.2 km s^{-1}, at scales similar to those of the HH 80N core (Basu and Mouschovias 1994), suggest a peculiar dynamical evolution of this core. Given the location of the HH 80N core (see Chapter 1), we question whether the HH 80/81/80N outflow has triggered, or at least sped up in some way, the collapse of the core.

In order to unveil the nature of the HH 80N core, we carried out an extensive set of mm and submm continuum and ammonia line observations over the last few years using several instruments, among them VLT and APEX. Using radiative transfer

models of collapsing protostellar envelopes, we compare the synthetic spectral energy distribution (SED) and spatial intensity profiles of the dust emission with the data. From this comparison, we derive the mass and luminosity of the collapsing envelope, mass infall rate, and mass of the embedded object under the hypothesis that a young stellar object (YSO) is forming inside the HH 80N core. We explore several density profiles for the initial configuration of the collapsing envelope, and discuss whether the inclusion of an accretion disk is needed to simultaneously explain the observed emission at different wavelengths. Our results point to a new picture for the HH 80N core, which consists of a "classic" Class 0 object (IRS1) surrounded by a reservoir of material where other clumps, potentially forming stars, are found.

4.2 Observations

4.2.1 VLA

We observed the $(J, K) = (1,1)$ and (2,2) ammonia inversion transitions (at 23.69 GHz and 23.72 GHz, respectively) using the Very Large Array (VLA) of the NRAO[1] in D configuration on 2007 January 31. The 4IF spectral correlator mode was used, which allows to observe both transitions simultaneously in two polarizations. The correlator was set to observe a bandwidth of 1.56 MHz with 63 spectral channels of 24.4 kHz (which gives 0.115 km s^{-1} velocity resolution at 1.3 cm) plus a continuum channel that corresponds to 75% of the bandwidth. The phase center of the observations was set to $\alpha(J2000) = 18^{\rm h}19^{\rm m}18\overset{\rm s}{.}81$ and $\delta(J2000) = -20°40'55\overset{''}{.}0$. The flux calibrator was 3C286 with a flux of 2.59 Jy, the phase calibrator was 1832-105 with a bootstrapped flux of 0.88 ± 0.01 Jy and the bandpass calibrator was 0319+415. Maps of the ammonia (1,1) transition were obtained with natural weighing and using a Gaussian taper of 35 kλ, which gives a beam size of $6\overset{''}{.}3 \times 4\overset{''}{.}4$ (P.A. = 20°0) and an rms noise level of 5×10^{-3} Jy beam^{-1} per channel. In this Chapter, we only present the map of the velocity-integrated flux density of the (1,1) transition, which presents extended emission with a good signal-to-noise ratio (see § 4.2), for comparison with the continuum data. A more complete analysis including the ammonia (2,2) transition, which is sensitive to warmer gas, is presented in Chapter 5.

[1]The National Radio Astronomy Observatory is a facility of the National Science Foundation operated under cooperative agreement by Associated Universities, Inc.

4.2.2 IRAM 30m

The 1.2 mm continuum observations were carried out with the 117-channel bolometer array (MAMBO 2) installed at the 30m IRAM telescope (Pico Veleta, Spain) on 2008 January 27 and 28 and March 3. The data were taken under low sky-noise conditions with the zenith opacity at 250 GHz ranging from 0.14 to 0.28. The on-the-fly technique was used with a scanning speed of $4''$ s^{-1}. Chopping was performed with throws of $58''$ and $70''$. The angular resolution of the map is $10\farcs5$ and the achieved rms noise level at this angular resolution is 1.5 mJy beam^{-1}. Data reduction was carried out with the MOPSIC software.

4.2.3 Plateau de Bure

The Plateau de Bure Interferometer (PdBI) observations were carried out on 2010 April 3 and 10 in C configuration. Two tracks were performed under good weather conditions. We made a six-point mosaic with the phase tracking center of the observations set at $\alpha(J2000) = 18^{\rm h}19^{\rm m}17\fs81$ and $\delta(J2000) = -20°40'47\farcs7$, coincident with the *Spitzer* 8 μm peak position (see § 3.1). The receivers were tuned to the rest frequency of the N_2D ($1_{1,1}$–$1_{0,1}$) line. The correlator was configured in four widex units (two units for each polarization) that gives a total continuum bandwidth of 8 GHz, plus two narrow windows of 20 kHz covering the N_2D ($1_{1,1}$–$1_{0,1}$) (85.926263 GHz) and $HN^{13}C$ (1–0) (87.090859 GHz) transitions, with a velocity resolution of ~ 0.15 km s^{-1}. The phase calibrator was QSO 1911−201, which has a flux density of 1.09 Jy at the observed frequency, and the flux and bandpass calibrator was MWC349. The data were calibrated using CLIC following the baseline-based mode, since antenna-based solutions were not optimal for the shortest baselines. The continuum map was obtained using MAPPING with natural weighting, that gives a synthesized beam (HPBW) of $7\farcs0 \times 2\farcs9$ (P.A. = 11°) at 86 GHz. The spectral line data are presented in Chapter 5.

4.2.4 VLT

In the nights of 2009 May 2 and June 12, $Q-$band (20 μm) imaging of the HH 80N region was carried out in service mode using the VISIR instrument installed

at the Cassegrain focus of the UT3 telescope (Melipal) of the Very Large Telescope (VLT). The observations covered a field of view of $32\farcs5 \times 32\farcs5$ at a pixel scale of $0\farcs127$ pixel^{-1}.

The sky conditions were good: for the night of May 2 the optical seeing ranged from $0\farcs8$ to $0\farcs9$ and the air mass was $\sim$1.05 on average; for the night of June 12, the average optical seeing varied from $1\farcs0$ to $1\farcs5$ and the air mass was always less than 1.05. Under these conditions, the extrapolated seeing at the $Q-$band according to the Roddier formula ($\propto \lambda^{0.2}$) is $< 0\farcs5$. Taking into account that the VLT diffraction limit at the same band is $0\farcs5$, this implies that the angular resolution of our $Q-$band data is basically dominated by diffraction.

During the first observing night our target was observed for one hour through the Q1, Q2, and Q3 filters (covering 17.65 ± 0.83 μm, 18.72 ± 0.88 μm, and 19.50 ± 0.40 μm, respectively). However, due to the low luminosity of the target, it was not detected in any of these filters. On the second night, our target was observed solely in the Q2 filter for one hour and was detected with a signal-to-noise ratio of 17. In order to remove the atmospheric and telescope background the standard chopping and nodding technique in perpendicular directions was carried out with chop throws of $14''$. The standard star for photometric calibration, HD178345 (3.52, 3.15, and 2.88 Jy through Q1, Q2, and Q3 filters, respectively), was observed immediately after our target. A preliminary reduction of the data was carried out using the standard ESO reduction software including the graphical user interface to the pipeline, GASGANO. The final image resulting from shifting and combining the chopping and nodding cycles was obtained with the IRAF package.

The photometric calibration was performed using the 'visir_img_phot' recipe with the combined image of the cataloged standard star as an input. We obtained conversion factors of 11923.3 (Q1), 11235.0 (Q2, first night), 13379.4 (Q2, second night) and 2446.2 (Q3) between the number of detector counts per second and the source flux in Jy. $Q2-$band flux density of the target was obtained with standard aperture photometry using the PHOT task of IRAF with a circular aperture of radius $1\farcs9$ although we inspected values between $1\farcs5$ and $2\farcs5$. For the background subtraction, the sky contribution was fitted to an annulus situated between radii of $1\farcs9$ and $2\farcs8$ from the center of the aperture. Applying the conversion factor derived above, we obtain a flux density value of 0.175 mJy at 18.7 μm. The flux uncertainty was derived exploring the variation of the flux density value when measured using

different apertures.

4.2.5 APEX

The sub-mm data were obtained with the SABOCA camera, a 39 pixel bolometer array located on the Atacama Pathfinder EXperiment (APEX) telescope in the Chilean Andes. Each SABOCA pixel consists of a composite bolometer with superconducting thermistor on silicon nitride membranes. The pixels are arranged in a hexagonal layout consisting of a central channel and three concentric hexagons. The array is installed at the Cassegrain focus, where it has an effective field of view of 90″. SABOCA operates at 850 GHz (350 μm), which gives a beam size (FWHM) of 7.″7. The observations were carried out on 2009 October 7 in raster spiral mode with four scans, each providing a fully sampled area of $\sim 120'' \times 120''$. Two skydips, taken in between and after on-source observations, yielded values of ∼1.1 for the atmospheric zenith opacity. Pointing was checked on secondary calibrators G10.62, G5.89, and HD-163296.

All the scans were reduced using the miniCRUSH software, a reduced version for the APEX bolometers of the SHARC-2 data reduction package CRUSH. We used the default reduction procedure and the data were smoothed using a 4.″0 Gaussian that gives an angular resolution of 8.″5 and an rms noise of 0.09 Jy beam^{-1} for the final map.

4.2.6 Infrared archive data from *IRAS*, *Spitzer* and *Akari*

The *IRAS* Point Source Catalog (PSC) reports a weak source, IRAS 18163−2042, whose position uncertainty includes the HH 80N core. According to the catalog, this source was detected only at 60 μm with a flux density of ∼5 Jy and remained undetected in the rest of the bands ($\leq$ 0.5 Jy at 12 and 25 μm, and $\leq$ 250 Jy at 100 μm). However, these values are not reliable because of the presence of strong side lobes generated by the nearby luminous source IRAS 18162-2048. These side lobes create a complex background around IRAS 18163−2042, which may cause an underestimate of the flux values reported in the *IRAS* PSC. This motivated us to reprocess the four IRAS bands covering the HH 80N region with SCANPI. SCANPI, a utility provided by the Infrared Processing and Analysis Center (IPAC), performs

one-dimensional scan averaging of the *IRAS* raw survey data. As it combines all the scans passed over a specific position, its outcome has a higher sensitivity, ideal for obtaining fluxes of confused or faint sources. In particular, among all the possible input processing parameters of SCANPI, we gave special attention to the "local background fitting range". By default, an interval of radius $60'$ from the scan center is used to fit the background. From this interval, a central range depending on the band is excluded in the fitting in order to prevent contamination from the target: $2'$ (12 μm and 25 μm), $4'$ (60 μm) and $6'$ (100 μm). Using this default SCANPI yields values similar to the fluxes of the *IRAS* PSC for all the one-dimensional scans that pass through the HH 80N region. However, IRAS 18162−2048 is located $6'$ south-east from IRAS 18163−2042 and, hence, the default range for the background subtraction includes clearly the emission from this luminous source. Adopting $12'$ for the "source exclusion range" in the background fitting for all the bands, we obtained significantly higher flux values than those derived above. Other values for the "source exclusion range" yielded similar results provided that IRAS 18162−2048 is excluded from the background fitting range.

To better determine the flux at the *IRAS* bands we checked the Summary Tables in the Result Details page within the SCANPI Web site. The Summary Tables present single scan data. From these data, we plotted the flux after background subtraction versus sky offset for each single scan and manually inspected each plot in order to select the scan that showed the best detection. From the selected scan we adopted as the flux value the maximum value of the plot found within the offset interval passing through the target position. We performed this process for all the *IRAS* bands and obtained new flux values.

We also retrieved observational data of the HH 80N region from the *Spitzer* archive at the 4.5 and 8 μm IRAC bands that are part of a large sample of high-mass star-forming regions (PID: 3528). The data at these wavelengths complement our VLT observations very well.

Following the same procedure as for the $Q-$band data, we estimated the flux density at 4.5 and 8 μm with the aperture photometry technique using PHOT of IRAF. We found that significantly larger apertures must be used for the *Spitzer* data compared to the apertures used for the VLT data: $11''$ and $12''$ for 4.5 and 8 μm images, obtaining flux values of 0.026 and 0.041 Jy for 4.5 and 8 μm, respectively. As for the VLT data, the flux uncertainty was derived by monitoring the variation

of the flux value when measured using different apertures.

Finally, we made use of the recently available data from the Infrared Astronomical Satellite *Akari*. *Akari* is equipped with two instruments, IRC, covering several bands at near and mid-infrared wavelengths, and FIS, covering several bands at far-infrared wavelengths. From a total of six observable bands, in this Chapter we present the data of 18, 140 and 160 μm bands. The rest of the bands have bad-quality data or null detection for our source.

4.3 Results

4.3.1 Continuum emission

Figure 4.1 presents the mid-IR images of the HH 80N region. The *Spitzer* images at 4.5 and 8 μm show a bright compact source dominant in the two wavelengths (HH 80N-IRS1). Two other compact sources, located $\sim 20''$ southeast (HH 80N-IRS2) and $\sim 15''$ northwest (HH 80N-IRS3) of HH 80N-IRS1, may belong to the region. The positions of these compact sources are given in Table 4.1. HH 80N-IRS1 is also detected in the VLT image at 18.7 μm, but without any extended structure, probably due to the short exposure time of our observations. Taking into account that the source is not resolved, and given the angular resolution of VLT at the $Q-$band ($\sim 0\farcs5$), the warm part of the envelope remains within $\sim$425 AU (for 1.7 kpc of distance) from the core center.

HH 80N-IRS1 is located at the center of the HH 80N core that is seen in absorption against the emission of the Galactic background in the 8 μm image. This observational picture resembles that of Infrared dark clouds (IRDCs), being the size of the silhouette of the HH 80N core ($\sim$0.4 pc) comparable to the lower limit of the range derived for a sample of IRDCs (0.4$-$15 pc Carey et al. 1998). However, while IRDCs harbor the earliest evolutionary stages of high-mass star formation (Rathborne et al. 2010), the mass estimated for the HH 80N core (see § 4.4 and below) seems too low to identify this core as a potential site for the formation of high-mass protostars.

As seen in Figure 4.2, the 350 μm emission is elongated with an angular size of

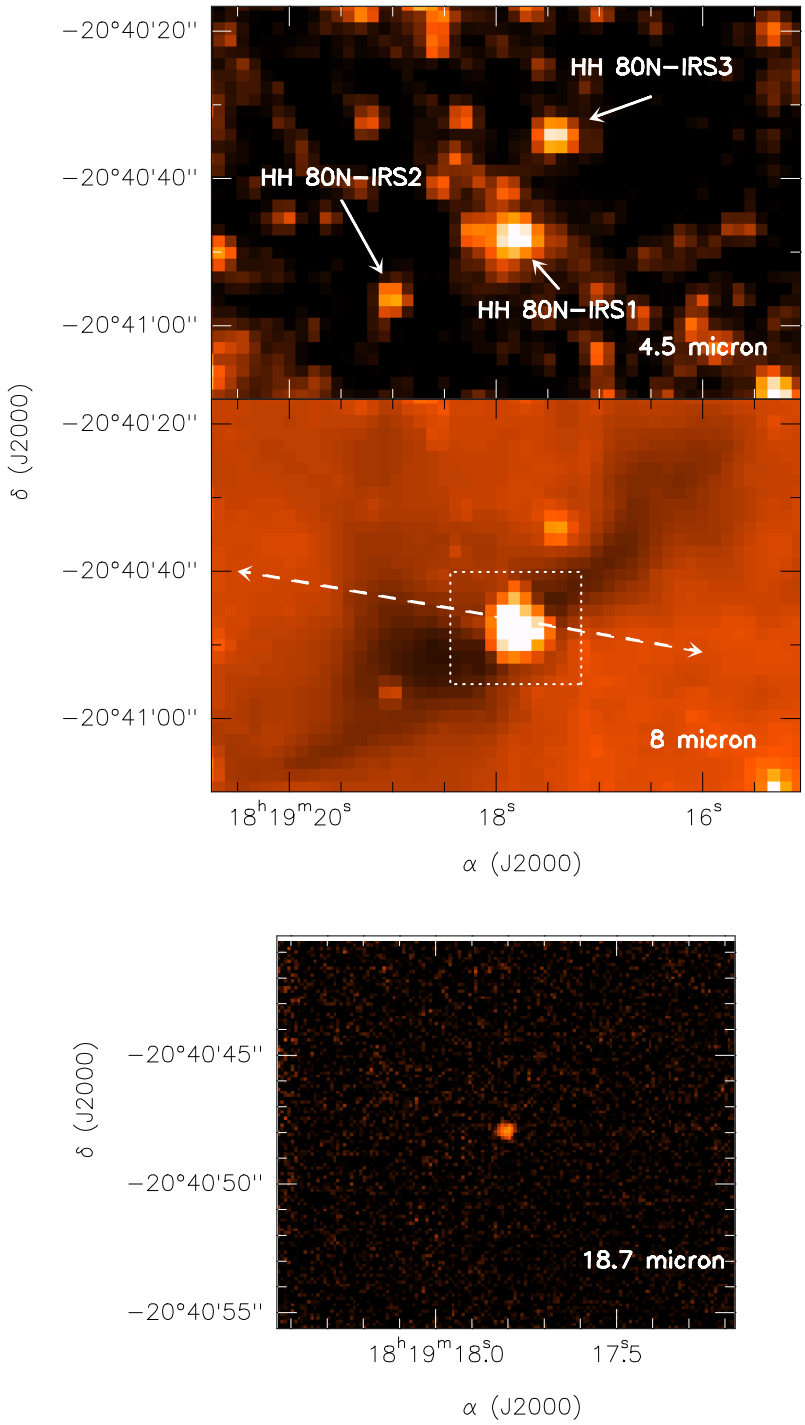

Figure 4.1: Images of the HH 80N region at 4.5 μm (top panel) and 8 μm (middle panel), retrieved from the *Spitzer* archive, and 18.7 μm (bottom panel) obtained with the VLT. In the middle panel, the dashed square shows the limits of the VISIR (VLT) field of view and the dashed arrow gives approximately the orientation and extent of the outflow detected by Girart et al. (2001).

Table 4.1: Positions of the Compact *Spitzer* Sources[a]

	Peak Position	
Source	R.A. (J2000)	Decl. (J2000)
HH 80N-IRS1	$18^h19^m17\overset{s}{.}81$	$-20°40'47\overset{''}{.}7$
HH 80N-IRS2	$18^h19^m19\overset{s}{.}01$	$-20°40'56\overset{''}{.}4$
HH 80N-IRS3	$18^h19^m17\overset{s}{.}42$	$-20°40'34\overset{''}{.}3$

Note.
[a] The HH 80N-IRS1 position was derived from the 8 μm image. HH 80N-IRS2 and HH 80N-IRS3 positions were derived from the 4.5 μm image.

$20'' \times 15''$ (FWHM) and P.A. $\sim$120°, and peaks at the position of HH 80N-IRS1. Apart from HH 80N-IRS1, the 350 μm emission traces additional material toward the southeast. The 1.2 mm emission peaks at the same position and traces fairly well the silhouette of the absorption feature of the 8 μm image including the northwestern tail expanding up to $35''$ from the central peak. The detection of this tail in emission at 1.2 mm and in absorption at 8 μm excludes the possibility of being an artifact of the 1.2 mm map. In the PdBI 3.5 mm map, the dust emission splits into two main sources, one clearly associated with HH 80N-IRS1, plus another southeastern component (hereafter Southeastern Condensation). Table 4.2 gives the results of Gaussian fits of the 3.5 mm emission for HH 80N-IRS1 and the Southeastern Condensation. In addition, the 3.5 mm map shows two marginally detected sources located $\sim 10''$ northwest and $\sim 20''$ southeast of HH 80N-IRS1.

Table 4.3 gives a summary of the flux density measurements toward HH 80N-IRS1. Since at mm and submm wavelengths it is difficult to discriminate which fraction of the emission of the HH 80N core corresponds to HH 80N-IRS1, in the table we report a range of possible values for the flux densities at these wavelengths. The upper limit of the range at 1.2 mm and 350 μm is an estimate of the HH 80N-IRS1 flux density avoiding the contamination from the Southeastern Condensation. To do this, we integrated the flux density of the western half of the HH 80N core and multiplied the resulting value by 2. The lower limit is the intensity peak that would coincide with the flux density of HH 80N-IRS1 if it were an unresolved source (i.e., the lowest possible contribution). For the 3.5 mm measurement, we take into account the missing short spacings of the PdBI. We made a crude analysis simulating the filtering effects of the u-v coverage of our PdBI observations. Using the UVMODEL

task of the MIRIAD package, we tested these filtering effects on several synthetic maps of artificially generated ellipses that mimic the HH 80N core appearance. We find that a maximum of 50% of the total flux is missed. Thus, in the range of flux densities given for the 3.5 mm emission, the lower limit corresponds to the flux density measured in the map and the upper limit corresponds to this value corrected by a factor of two. The data obtained with low angular resolution (i.e., all the *IRAS* data and the *Akari* 140 and 160 μm bands) are likely contaminated by background sources. Therefore, we considered these fluxes as upper limits. Finally, note that the complex background of the 8 μm image (see Figure 4.1) makes the estimate of the flux at this wavelength somewhat uncertain.

Table 4.2: Source Parameters Derived from the PdBI 3.5 mm Map[a].

	Peak Position		I_ν(peak)[b]	S_ν[c]	Deconvolved Size	P. A.
Source	R.A. (J2000)	Decl. (J2000)	(mJy beam^{-1})	(mJy)	($''$)	($^\circ$)
HH 80N-IRS1	$18^h19^m17\overset{s}{.}81$	$-20^\circ40'47\overset{''}{.}7$	2.03 ± 0.11	3.75 ± 0.19	5.0×3.0	-17.4
Southeastern Condensation	$18^h19^m18\overset{s}{.}31$	$-20^\circ40'52\overset{''}{.}2$	0.58 ± 0.06	2.48 ± 0.09	11.1×5.8	-17.0

Notes.
[a] Derived from a Gaussian fit with the task IMFIT of MIRIAD.
[b] Peak Intensity.
[c] Integrated flux density.

4.3.2 The nature of NH_3 emission

Figure 4.2 (bottom panel) presents the NH_3 (1,1) emission superimposed on the *Spitzer* 8 μm image. The ammonia is very well correlated with the 8 μm absorption feature. It is also well correlated with the 1.2 mm emission. This is not the case for other molecular tracers such as CS or SO presented in previous works (Girart et al. 2001; Masqué et al. 2009), whose emission is significantly more extended ($\sim 60'' \times 25''$). These studies also show that, in general, the molecular tracers do not peak all at the same position, probably because these molecules are depleted in the densest and inner part of the HH 80N core, which is well traced by the dust continuum emission.

The clear correlation between the NH_3 emission and dust emission indicates that NH_3 traces fairy well the material of the HH 80N core. Girart et al. (2001) detected star-forming signatures in the core, such as a bipolar outflow traced by CO. In addition, the dust continuum emission shows a compact source, HH 80N-IRS1, in

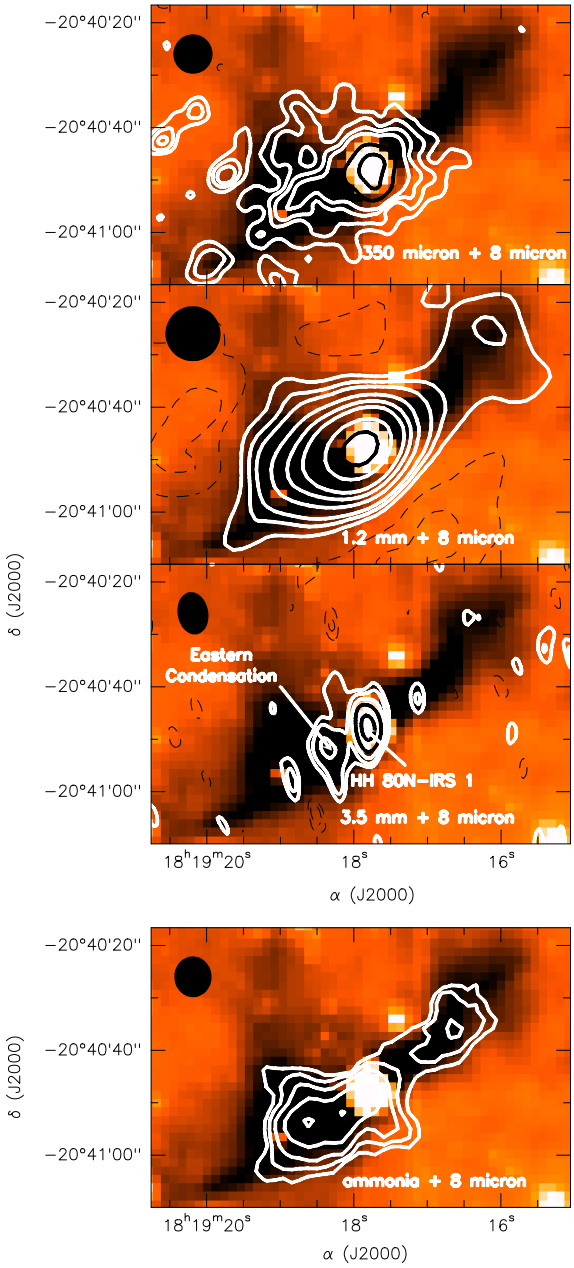

Figure 4.2: Maps of the HH 80N region taken at 350 μm (top panel), 1.2 mm (second panel), 3.5 mm (third panel) and the velocity integrated (zero-order moment) of the main line of NH_3(1,1) emission (bottom panel), superimposed on the *Spitzer* 8 μm image. Contour levels are 3, 4, 6, 9, 15, and 21 times 90 mJy beam^{-1} (350 μm); −6, −3, 3, 6, 9, 15, 21, 27, 39, and 50 times 1.5 mJy beam^{-1} (1.2 mm); −3, −2, 2, 3, 5, 7, and 10 times 0.11 mJy beam^{-1} (3.5 mm); 3, 6, 10, 16, and 24 times 0.24 Jy beam^{-1} km s^{-1}(NH_3). The beams are shown in the upper left corner of the panels. The color scale of the infrared image has been modified with respect to Figure 4.1 in order to highlight the absorption feature (see text).

Table 4.3: Summary of the Continuum Data of HH 80N-IRS1

Wavelength (μm)	Instrument	Angular Resolution[a] ($''$)	Aperture Size[b] ($''$)	Flux Density[c] (Jy)	Observing Epoch	Notes
3500	IRAM PdBI	2.9×7.0	$\sim 5 \times 10$	0.004–0.006	2010April	This paper
1200	IRAM 30m (MAMBO II)	10.5		0.084–0.177	2008 March	This paper
350	APEX (SABOCA)	8.5[d]	$\sim 30 \times 50$	2.1–5.9	2009 October	This paper
160	*Akari* (FIS)	~ 60	...	≤ 33.88	2006−2007	Archive data
140	*Akari* (FIS)	~ 55	...	≤ 36.11	2006−2007	Archive data
100	*IRAS*	180×300	...	≤ 108	1983	Archive data
60	*IRAS*	90×282	...	≤ 22.08	1983	Archive data
25	*IRAS*	45×276	...	≤ 1.24	1983	Archive data
18.7	VLT (VISIR)	~ 0.5	1.5	0.175 (0.01)	2009 June	This paper
18.0	*Akari* (IRC)	~ 7	...	0.170 (0.009)[e]	2006−2007	Archive data
12	*IRAS*	45×270	...	≤ 0.46	1983	Archive data
8	*Spitzer* (IRAC)	1.7	12	0.041 (0.010)	2005 September	Archive data
4.5	*Spitzer* (IRAC)	1.9	11	0.026 (0.003)	2005 September	Archive data

Notes.

[a] For the mm and submm data, the reported angular resolution corresponds to the FHWM of the beam size. For far-IR and mid-IR data, it corresponds to the point-spread function. For *Spitzer*, it corresponds to the pixel size, which is larger than the angular resolution.

[b] The box for the 350 μm and 1.2 mm data has a P.A. of 120° and it is chosen to include only HH 80N-IRS1 (see § 4.3.1). The values given for the IR data are the diameter of a circular aperture.

[c] For the 350 μm, 1.2 mm, and 3.5 mm measurements, we give a range in order to account for contamination effects from the Southeastern Condensation (see § 4.3.1). For the mid-infrared points, uncertainties are included into parentheses. We adopted the *IRAS* and *Akari* flux values as upper limits because of possible contamination by background sources.

[d] After smoothing with a Gaussian of FWHM = $4''.0$.

[e] Adopting a 5% of calibration uncertainty as indicated in the IRC Data User Manual.

all the observed wavelengths, suggesting the presence of an embedded YSO. All these results suggest that the HH 80N core is currently undergoing active star formation and that the observed distribution of NH_3 emission arises as a consequence of the high gas densities likely reached in the core, similar to other star-forming cores, and not as a consequence of photochemical effects. Ammonia emission arising as a consequence of a dynamical perturbation is excluded by the narrow NH_3 (1,1) linewidth ($\sim$ 1 km s^{-1}) observed. Nevertheless, we note that the strongest NH_3 emission is found in the southeastern part of the core, close to HH 80N, coinciding with the emission detected in the lower sensitivity ammonia observations of Girart et al. (1994). This could be due to a local increment of abundance in this part of the core as found in some species (Masqué et al. 2009); indeed, NH_3 is one of the species predicted to be enhanced by HH radiation (Viti et al. 2003). Understanding these local departures of the ammonia emission from the global distribution of gas and dust in the HH 80N core is an issue that will require further investigation.

4.4 Modeling

In the following we analyze this region assuming that an YSO is forming inside the HH 80N core. To do that, we calculate the dust emission arising from a envelope of dust and gas that is collapsing onto a central star. We consider three possible density profiles for the envelope. We first investigate the collapse of a singular logatropic sphere (SLS; McLaughlin and Pudritz 1996; Osorio et al. 1999, 2009). The SLS has a logarithmic relationship between pressure and density, introduced by Lizano and Shu (1989) to empirically take into account the observed turbulent motions in molecular clouds. In the SLS collapse solution an expansion wave moves outward into the static core and sets the gas into motion toward the central star. Outside the radius of the expansion wave the SLS envelope is static, with a dependence of the density on radius as $\rho \propto r^{-1}$. Inside the radius of the expansion wave the gas falls onto the central star with a nearly free-fall behavior ($v \propto r^{-1/2}$, $\rho \propto r^{-3/2}$) at small radii.

As a second approach, we adopt the collapse solution of the singular isothermal sphere (SIS; Shu 1977). In this case, the collapse occurs in a similar fashion as in the logatropic case but the radial dependence of the density in the static region is $\rho \propto r^{-2}$. Nevertheless, there are important differences in the evolution of both types

of collapses as both the speed of the expansion wave and the mass infall rate are constant in the SIS collapse while they increase with time in the SLS collapse.

As a third approach we use the solution for the collapse of a slowly rotating core described in Terebey et al. (1984), hereafter the TSC collapse (see also Cassen and Moosman 1981; Kenyon et al. 1993). In this model, the initial equilibrium state corresponds to the uniformly rotating analog of the SIS. To first order, the collapse proceeds similarly to the isothermal case beginning at the center of the core and propagating outward at sound speed as an expansion wave. Material outside the radius of the expansion wave remains in hydrostatic equilibrium (with $\rho \propto r^{-2}$) while inside this radius the infall velocity and density approach those of free fall. However, the angular momentum of the infalling gas becomes important in the vicinity of the centrifugal radius, where motions become significantly non radial and material then falls onto a circumstellar disk rather than radially onto the central object. The centrifugal radius is given by $R_c = r_0\Omega_0/(GM_*)$, where Ω_0 is the angular velocity at a distant reference radius r_0.

The HH 80N core has a moderate bolometric luminosity, but relatively strong mm and submm emission. By integrating the area below the observed SED, constructed with the flux densities of Table 4.3, we can derive a possible range of luminosities for HH 80N-IRS1. Considering the lower limits of the mm and submm points and excluding the rest of the continuum data in this calculation, we obtain 10 $L_\odot$ as the luminosity lower limit. Similarly, taking the upper limits of the mm and submm range and including the 60 μm $IRAS$ point, which is the most restrictive upper limit in the IR part of the SED, we obtain an upper limit of 110 $L_\odot$ for the luminosity. We are assuming that the total luminosity, which is responsible for internal heating of the core, is the sum of the stellar luminosity and the infall luminosity caused by the infalling gas onto the protostar. The stellar luminosity can be related to the mass of the central star using the Schaller et al. (1992) evolutionary tracks. The upper limit of the luminosity range deduced above (110 $L_\odot$) restricts the mass of the central embedded object to $\leq$3 $M_\odot$, according to the tables of Schaller et al. (1992); this mass upper limit corresponds to the hypothetical case that all the luminosity of the source was due entirely to the stellar luminosity.

For the SLS and SIS envelopes, the dust temperature is self-consistently calculated from the total luminosity using the dust opacity and the procedures described in Osorio et al. (1999, 2009). These authors calculate the dust opacity at short

wavelengths ($\lambda < 200$ μm) assuming that the dust in the envelope is a mixture of graphite, silicates, and water ice, with abundances taken from D'Alessio (1996), and assuming a power law of the form $\kappa_\lambda \propto \lambda^{-\beta}$, with $1 \leq \beta \leq 2$, for $\lambda \geq 200$ μm.

The temperature in the TSC case is also self-consistently calculated from the total luminosity, following the procedures described in Calvet et al. (1994) and Osorio et al. (2003). The latter authors obtain the dust opacity over the whole wavelength range assuming a mixture of graphite, silicates, and water ice, whose parameters (grain size and abundance) are obtained by fitting the well sampled SED of the prototypical class I object L1551 IRS5.

We computed the SEDs of the models and compared them with the observed values of the flux density of HH 80N-IRS1 (Table 4.3). Additionally, we produced synthetic maps of the model emission at 3.5 mm, 1.2 mm, and 350 μm bands. In order to fully simulate the observations, the synthetic maps at 1.2 mm and 350 μm were convolved with Gaussians with FHWMs of $10\farcs5$ and $8\farcs5$, respectively. For the synthetic map at 3.5 mm, the effect of the missing short spacings of the interferometric observations was taken into account. We used the UVMODEL task of MIRIAD to compute the visibility tables of the 3.5 mm models with the same $u-v$ plane coverage as our PdBI observations. Then, from the model visibility tables, we obtained synthetic maps following the standard data reduction routines of the MIRIAD package.

Finally, to check the goodness of our results, we compared selected models with the data by means of spatial intensity profiles obtained using the task CGSLICE of the MIRIAD package, for both the synthetic and observed maps at 1.2 mm, 3.5 mm, and 350 μm. We present two cuts of the observed intensities with P.A. $\simeq 120°$ and $\simeq 30°$ (mainly along the major and minor axes of the HH 80N core seen at 1.2 mm and 350 μm). An intensity profile obtained with a cut with a selected P.A., instead of averaging the emission over an annulus, prevents including contamination of the Southeastern Condensation. In practice, the synthetic maps of the models in the three approaches have radial symmetry since, in the TSC case, the angular scale of the flattening of the envelope is small enough that it only affects the central pixel of the map. Therefore, for the synthetic maps, we obtained a cut along the diameter of the modeled source.

We explore the SLS and SIS cases separately by running a grid of models taking the mass infall rate ($\dot{M}_{\rm i}$), mass of the central embedded object (M_*), and the external

radius of the core ($R_{\rm ext}$) as free parameters. Because of the complex morphology of the source (see Figure 4.2) we do not adopt a fixed value of $R_{\rm ext}$; rather, its value is constrained in the fit. The opacity index (β) was derived to get a tradeoff to reproduce simultaneously the emission at 1 mm and 350 μm. This yields $\beta \sim 1.6$ for the SLS case and $\beta \sim 1.1$ for the SIS case. For the stellar radius (R_*) we chose a standard value of 5 $R_\odot$ (Schaller et al. 1992). Given the space of parameters ($R_{\rm ext}$, $\dot{M}_{\rm i}$), we tested values of M_* from 0.5 to 1 $M_\odot$. Because a fraction of the luminosity is due to infall, higher values of M_* would yield luminosities that exceed the upper limit of 110 $L_\odot$ derived above, assuming that $\dot{M}_{\rm i} > 10^{-5} M_\odot$ yr^{-1}.

The best-fit model can be determined by calculating the χ^2-statistics obtained from the residual map resulting from subtracting the synthetic from the observed maps. This process was performed for all the sub/mm bands. To find the best fit to the images, we do not include contamination of the Southeastern Condensation in the χ^2 analysis. For the 350 μm band, the χ^2 function was calculated over a region comprising only the western part of the HH 80N core, roughly a semicircle with a radius of $\sim 20''$. In the 1.2 mm map, HH 80N-IRS1 cannot be separated from the Southeastern Condensation due to the lower angular resolution of the IRAM 30m observations with respect to the APEX observations. For this case we fit the intensity profile obtained along the minor axis of the emission (i.e., toward NE). For the 3.5 mm map, as HH 80N-IRS1 appears detached from the Southeastern Condensation in the map, a box of $\sim 5'' \times 10''$ enclosing the entire source was used. Additionally, we calculated the χ^2 function for the SED by comparing the fluxes of Table 4.3 with the predicted SED of the model.

Because the TSC models predict the development of a flattened rotating structure at the innermost part of the envelope, we carried out the modeling assuming a TSC envelope falling onto a disk surrounding the central object. We browsed an appropriate disk model from the online catalog of models of irradiated accretion disks around pre-main-sequence stars (D'Alessio et al. 2005). For consistency, the orientation of the disk is chosen to coincide with the rotation axis of the TSC envelope and the disk radius is fixed to the value of the centrifugal radius R_c. To obtain the SED of the total composite model, we added the fluxes of the disk and envelope at each wavelength, accounting for the extinction of the envelope, which is important at short wavelengths. Since the disk is unresolved even in the images with the highest angular resolution, to obtain the synthetic maps we added the disk to the envelope as a point source at the central pixel.

Due to computational limitations, the fitting process of the TSC envelope plus circumstellar disk could not be automated. Our strategy, then, was to perform a case-by-case exploration varying the external radius of the core ($R_{\rm ext}$), the radius of the expansion wave ($R_{\rm ew}$), and the reference density (ρ_1) (this latter parameter is the density the envelope would have at a radius of 1 AU for the limit $R_c = 0$, and it is related to the mass infall rate and the central mass through Equation (3) of Kenyon et al. (1993), until we find a model that explains satisfactorily the SED and the intensity profile at 350 μm, 1.2 mm, and 3.5 mm. The caveat of this method is that there is no assurance of finding a unique best-fit model. However, the goal of this section is to prove that the observed properties of the continuum emission observed in the HH 80N core can be explained in terms of a protostar plus an infalling envelope that is embedded inside the HH 80N core. Constraining a unique model with a flattened envelope and a disk requires additional mid-IR observations with high angular resolution and is beyond the scope of this study.

4.4.1 Results for the SLS model

We tested the logatropic density distribution by using 1080 different models within the following set of ranges for the external radius, mass infall rate, and mass of the central embedded object: 0.04 pc $\leq R_{\rm ext} \leq$ 0.18 pc, $7 \times 10^{-6} M_\odot$ yr^{-1} $\leq \dot{M}_{\rm i} \leq$ $5 \times 10^{-5} M_\odot$ yr^{-1}, and 0.5 $M_\odot \leq M_* \leq$ 1.0 $M_\odot$. In this space of parameters we expect to find meaningful physical solutions. To establish the goodness of the fit we calculated χ^2 as discussed in the previous section. Figure 4.3 shows the best set of solutions for the χ^2 estimated separately for the SED and for the 1.2 mm and 350 μm intensity distributions. We also calculated the χ^2 function for the 3.5 mm band but the results are not included in the figure because no set of parameters can provide reasonable χ^2 values at this band. We consider those as good solutions where the χ^2 values of the intensity distributions and of the SED are all within the 90% level of confidence.

Figure 4.3 shows that there are no solutions that fit together the SED and the intensity distribution of the 1.2 mm and 350 μm maps (i.e., there is no overlap between the χ^2 contours of the maps and those of the SED). As an example, Figures 4.4 and 4.5 show, respectively, the predicted SED and intensity profiles (dash-dotted lines) of the SLS model that gives the minimum χ^2 for the SED, compared with the observed data. Except for the mid-IR wavelengths, the observed SED is reproduced

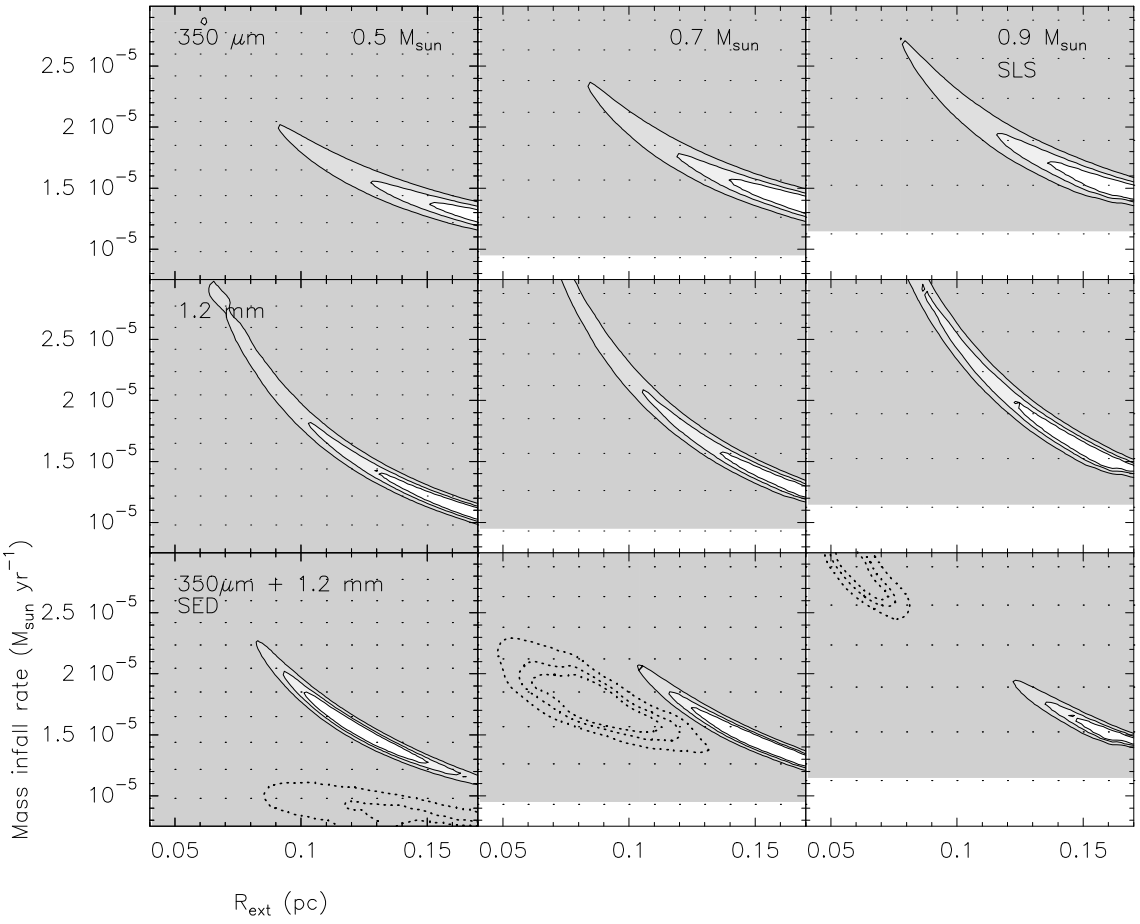

Figure 4.3: Contour plots (solid line and gray scale) of the χ^2 function derived for the fitting of the models of the collapse of the Singular Logatropic Sphere to the observed images. Rows correspond to the 350 μm band (top), the 1.2 mm band (middle), and the sum of the χ^2 function for the 350 μm and 1.2 mm bands (bottom). The dotted contours shown in the bottom panels correspond to the χ^2 function derived for the SED. Columns correspond to $M_* = 0.5\ M_\odot$ (left), 0.7 $M_\odot$ (middle), and 0.9 $M_\odot$ (right). In all the cases, the contour levels correspond to the confidence levels of 99%, 90%, and 68% (1σ). These contours are relative to the minimum χ^2 value of each panel, which may vary significantly for different masses. For instance, in the bottom row, where we compare the results of the SED and single-dish maps, the minimum χ^2 values of the SED are 53.4, 33.2, and 19.2 for 0.5, 0.7, and 0.9 $M_\odot$, respectively; the sums of the minimum χ^2 values of the 350 μm and 1.2 mm maps are 102.2, 119.0, and 122.2 for 0.5, 0.7, and 0.9 $M_\odot$, respectively.

reasonably well by the model. However, as Figure 4.5 shows, this model produces intensity profiles too flat and cannot reproduce the observed intensity profiles in any of the bands. Given these discrepancies, we conclude that in the logatropic case the mass is not distributed adequately in the envelope to match the observations.

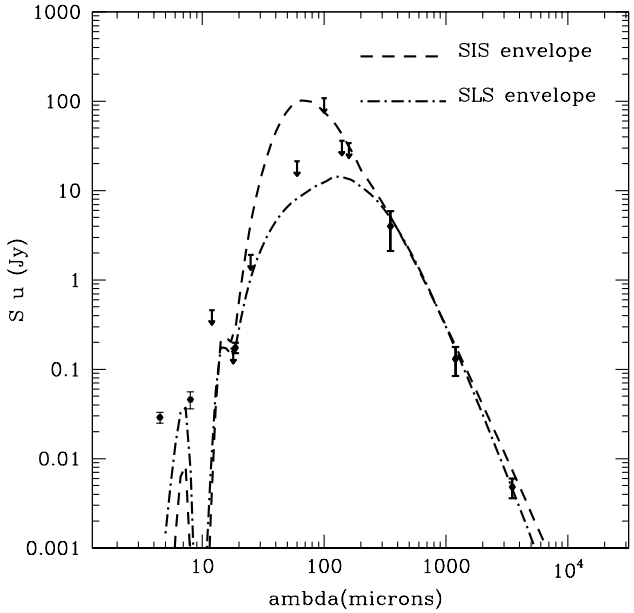

Figure 4.4: Observed flux densities (dots; see Table 4.3) and predicted SEDs for HH 80N-IRS1, assuming models of the collapse of the Singular Logatropic Sphere (SLS; dash-dotted line) and of the Singular Isothermal Sphere (SIS; dashed line). Bars represent the uncertainties and arrows represent the upper limits. The SLS model corresponds to the model that minimizes the χ^2 of the SED ($R_{\rm ext}$ = 0.1 pc, M_*= 0.7 $M_\odot$, $\dot{M}_{\rm i}$= 1.57 $\times 10^{-5}$ $M_\odot$ yr^{-1}, $L_{\rm bol}$ = 69 $L_\odot$, $M_{\rm env}$ = 25.5 $M_\odot$, and β = 1.6). The SIS model corresponds to the model that minimizes the χ^2 function for the maps at 1.2 mm and 350 μm ($R_{\rm ext}$ = 0.05 pc, M_* = 0.8 $M_\odot$, $\dot{M}_{\rm i}$ = 1.05 $\times 10^{-4} M_\odot$ yr^{-1}, $L_{\rm bol}$ = 527 $L_\odot$, $M_{\rm env}$ = 4.6 $M_\odot$, and β = 1.1).

4.4.2 Results for the SIS model

We tested the isothermal density distribution by using 1800 different models within the following set of ranges for external radius, mass infall rate, and mass of the central embedded object: 0.03 pc $\leq R_{\rm ext} \leq$ 0.22 pc, $1.2 \times 10^{-5} M_\odot$ yr^{-1} $\leq \dot{M}_{\rm i} \leq$

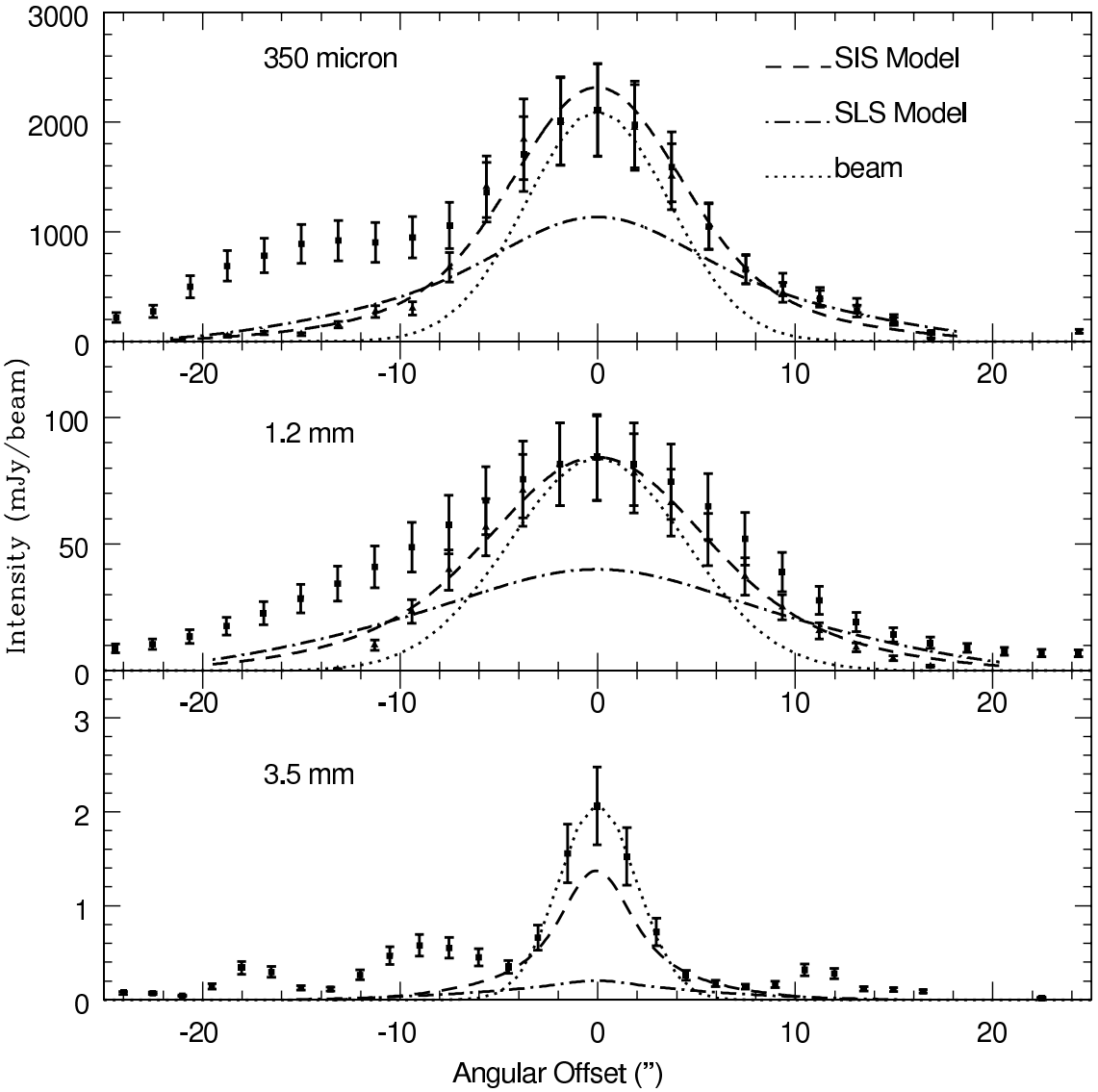

Figure 4.5: Observed and modeled intensity profiles of HH 80N-IRS1 at 350 μm (top), 1.2 mm (middle) and 3 mm (bottom). The squares and triangles represent observed cuts along the major (P.A. $\simeq 120°$) and minor (P. A. $\simeq 30°$) axes of the HH 80N core, respectively. Bars represent the uncertainties. At 3.5 mm, as the source appears unresolved, we present only a cut along the major axis of the core (P.A. $\simeq 120°$). The dash-dotted lines correspond to cuts along the diameter of the synthetic maps of the Singular Logatropic Sphere model that minimizes the χ^2 for the SED (see Figure 4.4). The dashed lines correspond to cuts along the diameter of the synthetic maps of the Singular Isothermal Sphere model that minimizes the χ^2 for the maps (see Figure 4.4). The dotted line represents the beam.

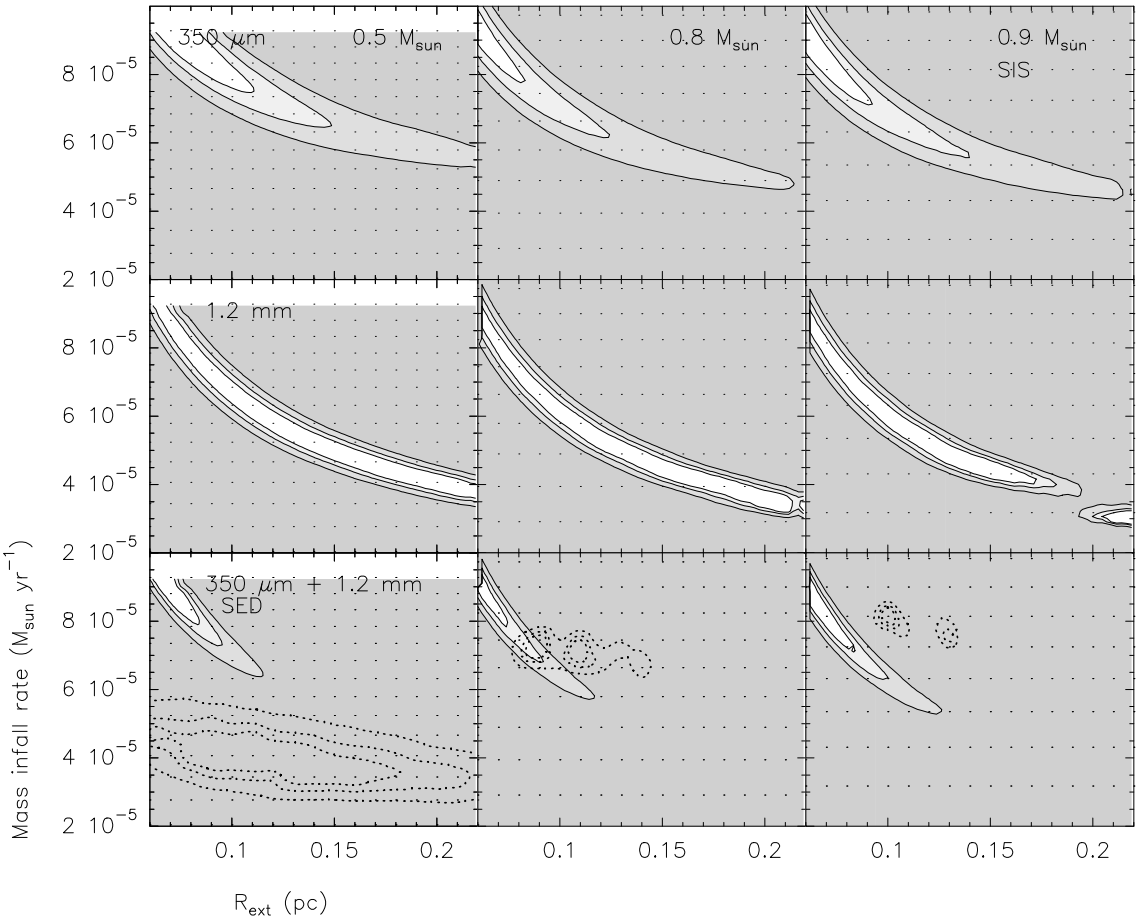

Figure 4.6: Contour plots (solid line and gray scale) of the χ^2 function derived for the fitting of the models of the collapse of the Singular Isothermal Sphere to the observed images of HH 80N-IRS1. Rows correspond to the 350 μm band (top), the 1.2 mm band (middle), and the sum of the χ^2 function for the 350 μm and 1.2 mm bands (bottom). The dotted contours shown in the bottom panels correspond to the χ^2 function derived for the SED. Columns correspond to $M_* = 0.5\ M_\odot$ (left), 0.8 $M_\odot$ (middle), and 0.9 $M_\odot$ (right). In all the cases the contour levels correspond to the confidence levels of 99%, 90%, and 68% (1σ). These contours are relative to the minimum χ^2 value of each panel, which may vary significantly for different masses. For instance, in the bottom row, where we compare the results of the SED and single-dish maps, the minimum χ^2 values of the SED are 47.1, 278.6, and 600.3 for 0.5, 0.7, and 0.9 $M_\odot$, respectively; the sums of the minimum χ^2 values of the 350 μm and 1.2 mm maps are 40.6, 36.1, and 36.7 for 0.5, 0.7, and 0.9 $M_\odot$, respectively.

$1.6 \times 10^{-4} M_\odot$ yr^{-1}, and 0.5 $M_\odot \leq M_* \leq 1.0$ $M_\odot$. Figure 4.6 shows the best models from the χ^2 analysis for the SIS case. For the same reasons as in the logatropic case, we have not included the 3.5 mm results in the figure.

The mass infall rates considered for the SIS collapse are higher than those considered in the logatropic case. This is because, for a given value of the mass infall rate, the SIS models yield less massive envelopes than the SLS models; so, in order to fit properly the mm flux densities higher values of the mass infall rate are required in the SIS models (see Osorio et al. 1999). For this reason, $R_{\rm ext}$ becomes almost irrelevant and $\dot{M}_{\rm i}$ takes the dominant role in the fitting. Figure 4.6 (bottom panels) shows that for the $M_* = 0.8\ M_\odot$ case, there are solutions that apparently satisfy both the SED and (sub)mm intensity distribution constraints (i.e., for 0.8 $M_\odot$, the χ^2 contours of the SED overlap those of the maps for $R_{\rm ext} \simeq$ 0.08-0.1 pc and $\dot{M}_{\rm i} = (6.5 - 8.0) \times 10^{-5}\ M_\odot$ yr^{-1}). Nevertheless, despite these solutions yielding reasonable intensity distributions in the 1.2 mm and 350 μm bands, they overestimate the total luminosity, specially at far-IR wavelengths. In Figure 4.4 (dashed line) we show an example that illustrates this behavior (the predicted flux is almost one order of magnitude above the observed flux at 60 μm). As in the SLS case, the modeled intensity profile at 3.5 mm (dashed line in Figure 4.5) is significantly weaker than the observed profile. These results are general and we can find solutions that can fit the single–dish intensity distribution of the envelope but they predict an excess of luminosity and fail to reproduce the compact emission seen in the 3.5 mm PdBI map. In conclusion, as in the SLS case, there is no SIS model that can fit the SED and the maps simultaneously.

4.4.3 Results for the TSC model

One of the caveats of the SLS and SIS models is that they are unable to fit the intensity of the compact source seen in the PdBI 3.5 mm map. This compact source could have a significant contribution from a circumstellar disk. In this section we model the source assuming a TSC envelope falling onto a disk surrounding the central object obtained from the catalog of D'Alessio et al. (2005). Apart from using a more realistic model, such a configuration is ideal for two reasons. First, if the circumstellar disk is populated by millimeter-size grains, its emission can be significant at mm wavelengths and, because it is compact, it will be less affected by the interferometric filtering that affects the envelope emission. Second, because

the SED at short wavelengths is very sensitive to the geometry of the source, the TSC envelope and a disk with the proper inclination can provide the extinction required to fit the mid-IR part of the SED, depending on the inclination of the axis of the system (envelope plus disk). This would give luminosities similar to or below 110 $L_{\odot}$. In addition, the infall luminosity is reduced because the material lands on a disk instead of falling directly onto the protostar.

We tested several TSC envelopes exploring values of the central luminosity 50 $L_{\odot} < L_{*} < 250$ $L_{\odot}$, outer radius of the envelope 0.07 pc$< R_{\rm ext} <$ 0.18 pc, the radius of the expansion wave 0.03 pc$< R_{\rm ew} <$ 0.09 pc, and reference density 4.1×10^{-13}g cm^{-3} $< \rho_1 < 1 \times 10^{-12}$ g cm^{-3} (these values of ρ_1 are equivalent to densities at 1000 AU between 7.8×10^5 and 7.4×10^6 cm^{-3}, and correspond to values of the mass infall rate between 3.2×10^{-5} and 3.3×10^{-4} $M_{\odot}$ yr^{-1} for a 3 $M_{\odot}$ star). For the circumstellar disk we explored accretion rates from the disk to the protostar between 10^{-9} and $10^{-6} M_{\odot}$ yr^{-1}, and we assume that the disk is irradiated with a similar luminosity and has a similar inclination as the envelope. In Table 4.4 we give the parameters of our favored model. Figures 4.7 and 4.8 show the observed SED and intensity profiles, respectively, predicted by our favored TSC model. These figures show that the SED is reproduced well by the model at almost all the data points and that the modeled intensity profiles fit the observations reasonably well within the calibration uncertainties.

At 3.5 mm, the inclusion of a disk provides the flux needed to explain the observed intensity peak. We note that, possibly, a fine tuning of the mass accretion rate could provide a more accurate fit for the intensity profiles. However, the range of accretion rates of the online disk model grid is sampled in steps that vary one order of magnitude and the next available model has an accretion rate too small and provides too faint mm emission. Nevertheless, in this analysis we aimed to prove that our continuum observations can be explained in the frame of standard star-forming models and our favored model presented above fulfills this requirement. Table 4.5 shows a summary of the χ^2 analysis (SED, single-dish and interferometric maps) for this TSC (+disk) model (Figures 4.7, 4.8), as well as for the SLS and SIS models shown in Figures 4.4 and 4.5. The reduced χ^2 values show that in the TSC case we obtain a better fit.

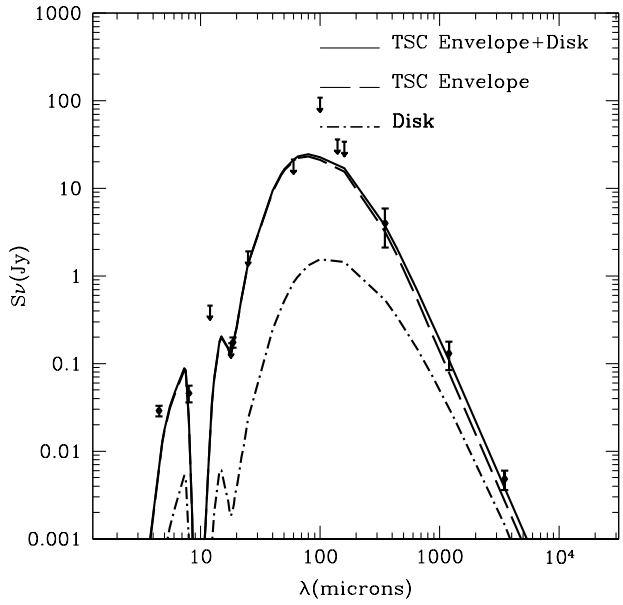

Figure 4.7: Observed flux densities (dots; see Table 4.3) and predicted SED for HH 80N-IRS1, assuming the Terebey, Shu, and Cassen (TSC) envelope model plus an accretion disk. Bars represent the uncertainties and arrows represent upper limits. The dashed line represents the SED of our favored TSC envelope model ($R_{\rm ext} = 1.8 \times 10^4$ AU, M_*= 3 $M_\odot$, $\dot{M}_{\rm i} \simeq 1.6 \times 10^{-4} M_\odot$ yr^{-1}, $L_{\rm bol} = 105\ L_\odot$, and $M_{\rm env} = 20\ M_\odot$). The point dashed line represents the SED of the selected disk model ($\dot{M}_{\rm acc} = 10^{-7} M_\odot$ yr^{-1}, R_c = 300 AU, and $i = 30°$). The solid line represents the resulting SED of our favored TSC envelope plus the disk model.

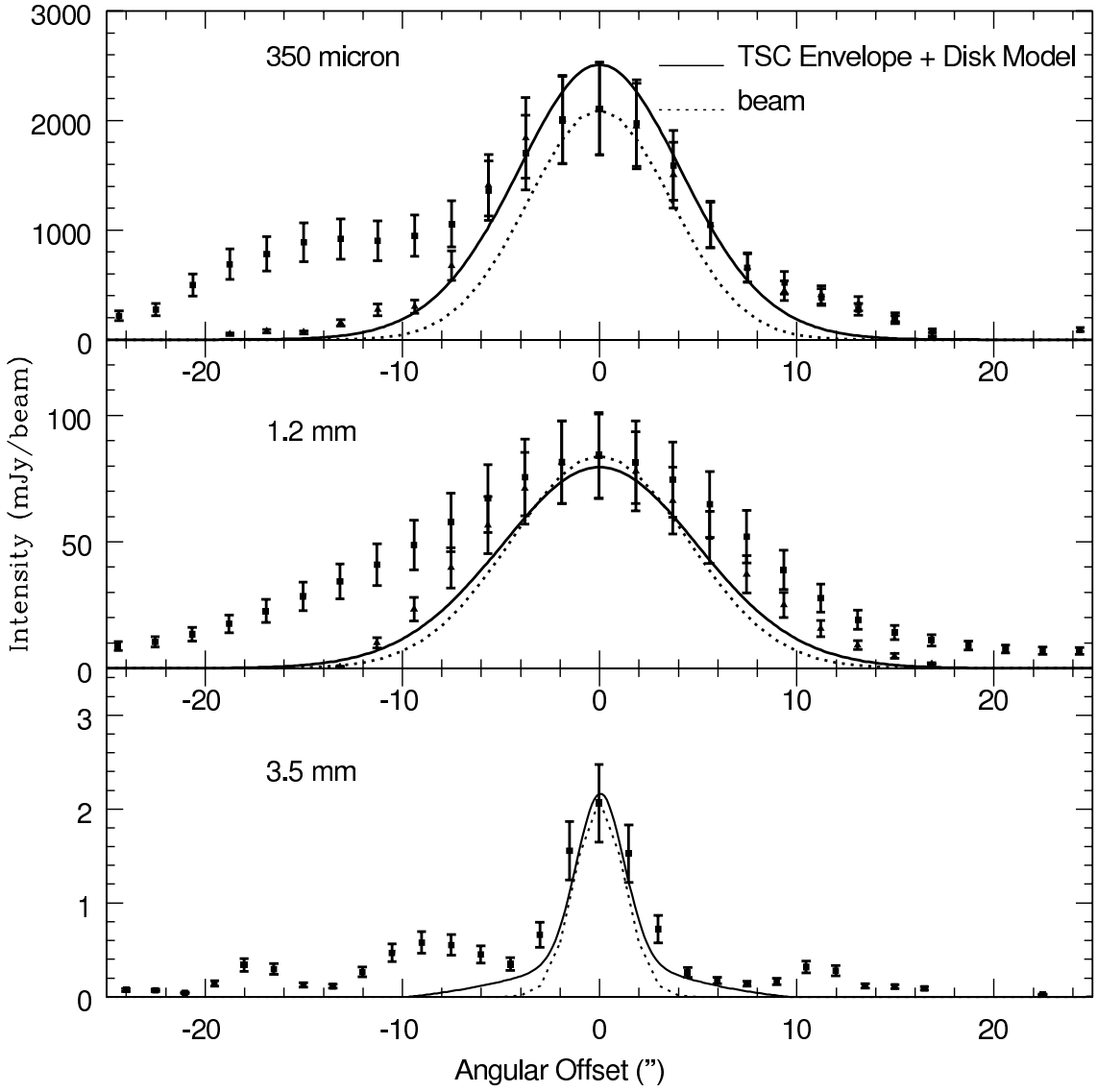

Figure 4.8: Observed and modeled intensity profiles of HH 80N-IRS1 at 350 μm (top), 1.2 mm (middle), and 3 mm (bottom). The squares and triangles represent observed cuts along the major (P.A. $\sim 120°$) and minor (P. A. $\sim 30°$) axes of the HH 80N core, respectively. Bars represent the uncertainties. At 3.5 mm, as the source appears unresolved, we present only a cut along the major axis of the core (P.A. $\sim 120°$). The solid lines correspond to cuts along the diameter of the synthetic maps of our favored Terebey, Shu, and Cassen envelope plus a disk model (see Figure 4.7). The dotted line represents the beam.

Table 4.4: Results of the TSC Modeling.

Envelope parameter	Symbol	Value
Mass	M	20 $M_\odot$
Central luminosity	L_*	105 $L_\odot$
Radius of the expansion wave[a]	$R_{\rm ew}$	1.5×10^4 AU
Outer radius	$R_{\rm ext}$	1.8×10^4 AU
Inclination angle	i	30°
Centrifugal radius	R_c	300 AU
Reference density	ρ_1	5×10^{-13} gr cm^{-3}
Density at $r = 1000$ AU	n (1000 AU)	4.1×10^6 cm^{-3}
Mass infall rate [b]	$\dot{M}_{\rm i}$	$1.6 \times 10^{-4} M_\odot$ yr^{-1}
Disk parameter[c]	Symbol	Value
Mass	$M_{\rm disk}$	0.6 $M_\odot$
Radius[d]	$R_{\rm disk}$	300 AU
Inclination angle[e]	i	30°
Mass accretion rate	$\dot{M}_{\rm acc}$	$10^{-7} M_\odot$ yr^{-1}
Viscosity parametrization	α	0.01
Slope of grain size distribution	p	3.5
Minimum grain size	$a_{\rm min}$	0.005 μm
Maximum grain size	$a_{\rm max}$	1 mm

Notes.

[a] Radius of the infalling region. Outside this radius the envelope remains static.

[b] Obtained adopting a mass of $M_* = 3\ M_\odot$ for the embedded protostar (i.e., the infall rate value is an upper limit).

[c] Obtained assuming that the disk is irradiated by a luminosity equal to the central luminosity $L_* = 105\ L_\odot$.

[d] Assumed to coincide with the centrifugal radius derived for the envelope.

[e] Assumed to coincide with the inclination angle derived for the envelope.

Table 4.5: Reduced χ^2 Results.

Model	SED	Single-dish Maps[a]	Interferometric Map[b]
SLS model	34.1	31.5	68.3
SIS model	441.4	3.3	13.3
TSC+disk model	3.5	8.1	5.5

Notes.
[a] The 1.2 mm map obtained with MAMBO at the IRAM 30 m telescope, and the 350 μm map obtained with LABOCA at the APEX 12 m telescope.
[b] The 3.5 mm map obtained with the PdBI.

4.5 Discussion

The derived physical parameters of the selected TSC model listed in Table 4.4 suggest that HH 80N-IRS1 is a very young Class 0 protostar. First, the predicted volume density for HH 80N-IRS1 at 1000 AU, $n(H_2) \simeq 4 \times 10^6$ cm^{-3}, is typical of Class 0 sources (Jørgensen et al. 2002), and greater than Class I sources (Jørgensen et al. 2002) and prestellar cores (Kirk et al. 2005; Tafalla et al. 2002); second, the estimated upper limit of the mass infall rate, $\sim 2 \times 10^{-4} M_\odot$ yr^{-1} (see Table 4.4), is compatible with the high values of the mass infall rate typical of young Class 0 protostars (Maret et al. 2002), and yields an age of $\sim 2 \times 10^4$ yr for HH 80N-IRS1; finally, HH 80N-IRS1 fulfills the criteria proposed by Andre et al. (1993) for Class 0 objects, $L_{\rm submm}/L_{\rm bol} \geq 5 \times 10^{-3}$, which in our case is about 0.1. On the other hand, the derived luminosity of 105 $L_\odot$ for HH 80N-IRS1 is found in the threshold between low-mass and intermediate-mass protostars. Given the large reservoir of mass of the HH 80N core (see 1.2 mm and 350 μm maps of Figure 4.2) and the youth of the HH 80N-IRS1, we cannot discard further accumulation of material toward the central object.

From the integrated emission of the residual map at 1.2 mm (resulting from the subtraction of the emission of the synthetic map of the TSC model from the map observed with MAMBO) we can obtain a crude estimate of the mass of the HH 80N core outside the HH 80N-IRS1 envelope. Assuming optically thin dust emission with $\beta = 2$ and a temperature of $\sim$14 K (the boundary temperature of the HH

80N-IRS1 envelope) we derive a mass of ∼10 $M_\odot$ for this material. As we noted above, the HH 80N core, with a size of 0.16×0.12 pc and an estimated total mass of ∼30 $M_\odot$ (20 $M_\odot$ of HH 80N-IRS1 + 10 $M_\odot$ of the rest of the HH 80N core), contains more material than the infalling envelope associated with IRS1. According to the results of our TSC modeling (see Table 4.4) the mass of the envelope is 20 $M_\odot$, and the infall occurs within a radius of $R_{\rm ew} = 1.5 \times 10^4$ AU with the envelope being static outside this radius. Furthermore, the molecular emission of tracers such as CS, SO, and HCO^+ extends over a region considerably larger than the HH 80N core, as traced by the dust continuum and ammonia line emissions. Indeed, the emission of these molecular tracers has been interpreted as arising from a contracting ring around HH 80N-IRS1 with an inner radius (the radius of the region where these molecular species appear to be depleted) of 2.5×10^4 AU and an outer radius of 6×10^4 AU (Girart et al. 2001; Masqué et al. 2009). The estimated average volume density of the molecular ring is in the $5 \times 10^4 - 1.3 \times 10^5$ cm^{-3} range (Masqué et al. 2009), which seems too high, given the estimated density in the static part of the HH 80N-IRS1 envelope ($\sim 6 \times 10^4$ cm^{-3}, according to our modeling). Therefore, the kinematics and physical conditions in the molecular ring-like structure proposed by Girart et al. (2001) and Masqué et al. (2009) appear puzzling. The role of the HH 80/81/80N outflow in the properties of this molecular ring-like structure and the relationship with the onset of the star-forming process in the HH 80N core, in particular with the HH 80N-IRS1, protostar is an interesting issue that deserves further observational and theoretical investigation.

4.6 Conclusions

We have carried out dust continuum and ammonia line observations of the dense core ahead of HH 80N, complemented with archive data, covering a wide range of wavelengths. We analyzed the continuum data by means of self-consistent models using several approaches for the envelope structure and we discuss the inclusion of a protostellar disk. Additionally, we compare ammonia observations of the (1,1) transition with continuum emission (and absorption) maps. Our main conclusions are summarized as follows.

1. The NH_3 (1,1) emission shows a striking correlation with the dust continuum emission and with the absorption silhouette seen in the 8 μm *Spitzer* image.

This indicates that the ammonia traces fairly well the distribution of gas and dust in the HH 80N core. Pending a proper analysis of the NH_3 abundances, this preliminary assessment shows that there is no need to invoke photochemical effects caused by the nearby HH 80N object to explain the distribution of ammonia in the HH 80N core. However, a detailed inspection of the ammonia map shows that an important part of the NH_3 emission arises from the southeastern part of the core, close to HH 80N, which could be due to a slight abundance enhancement.

2. The continuum emission presents a peak at the same position ($\alpha(J2000) = 18^{\rm h}19^{\rm m}17\overset{\rm s}{.}81$, $\delta(J2000) = -20^{\circ}40'47\overset{''}{.}7$) in all the bands (4.5 μm, 8 μm, 350 μm, 1.2 mm and 3.5 mm). This emission peak is located at the center of the CO bipolar outflow found by Girart et al. (2001) suggesting the presence at this position of an embedded YSO (HH 80N-IRS1) that powers the outflow.

3. We find that the SED and the intensity distribution of the mm and submm emission of HH 80N-IRS1 can be reproduced by a slowly rotating infalling envelope described by the Terebey, Shu, and Cassen (TSC) solution, plus a circumstellar accretion disk. The mass of the envelope is 20 $M_{\odot}$, the central luminosity is 105 $L_{\odot}$, and the radius of the infalling region is $1.5{\times}10^4$ AU. The disk has a mass of 0.6 $M_{\odot}$ and a radius of 300 AU. Such a configuration, together with the derived high values of the mass infall rate ($1.7 \times 10^{-4}\,(M_*/3\,M_{\odot})^{1/2}\,M_{\odot}$ yr^{-1}), and young age ($\sim 2 \times 10^4$ yr), suggests that HH 80N-IRS1 may be a young Class 0 source.

4. The APEX map at 350 μm and, especially, the PdBI map at 3.5 mm, where the extended emission is resolved out, show signs of possible fragmentation suggesting that other sources, in addition to HH 80N-IRS1, could be embedded inside the HH 80N core. On the other hand, previous studies reveal that the molecular emission of some tracers is considerably more extended than the dust and NH_3 emission presented in this work. This suggests that the HH 80N core is surrounded by a larger molecular structure whose properties could be influenced by the proximity of the HH 80/81/80N outflow.

Chapter 5

Interferometric observations of the HH 80N core with N-bearing molecular species

5.1 Introduction

In Chapter 3, it is assumed that the molecular emission of the HH 80N core arises from a ring-like structure of 6×10^4 AU of radius, contracting with a supersonic infall velocity of $\sim$0.6 km s^{-1}, falling onto a central embedded object, IRS1. However, in Chapter 4, the continuum emission of IRS1 is modeled as a slowly rotating envelope, with an infalling region of $1.5{\times}10^4$ AU of radius and the rest of the envelope being static outside this radius, apparently in contradiction with the results of Chapter 3. The two scenarios can be consistent with each other if we consider that IRS1 undergoes a protostellar infall regime independent from the kinematics of the rest of the HH 80N core, the later interpreted in Girart et al. (2001) and in Chapter 3 of this work as supersonic infall motions. Actually, these kinematics could be associated with large velocity gradients along the envelope of the HH 80N core, possibly affected by the HH 80/81/80N outflow.

In order to investigate further on the kinematics of the HH 80N core, we need to disentangle the gas motions belonging to the protostellar collapse of IRS1 from those associated to large scale kinematics of the envelope, possibly reminiscent of

the velocity field of the initial conditions of the core prior to the onset of collapse. However, the study of star-forming cores at scales down to the region of collapse encounters one main problem: the freeze out of the molecules onto dust icy mantles that, at densities higher than 10^5 cm^{-3}, becomes dramatically efficient for a number of species (Bergin et al. 1995; Aikawa et al. 2001). Indeed, the ring-like structure observed with the molecular tracers of Chapter 3 has been interpreted by Girart et al. (2001) as the result of a strong molecular depletion at the inner region of the core. On the other hand, nitrogen bearing molecules have little or no depletion at such densities (Tafalla et al. 2002, 2004; Aikawa et al. 2003). In this sense, deuterated molecules are found to be key probes for extremely cold ($\simeq$10 K) and dense (10^5–10^6 cm^{-3}) gas (e.g. Caselli et al. 2002).

In this Chapter we present NH_3, NH_2D and $HN^{13}C$ observations aiming to recover the kinematic information of the densest regions of the HH 80N core (i.e. the regions missed by CS). In § 5.2 we describe the observations. The results are shown in § 5.3 In § 5.4 the ring-like morphology is discussed. Finally, in § 5.5, we present derived column densities and discuss the deuteration fractionation of the HH 80N core.

5.2 Observations

5.2.1 VLA

VLA observations are described in Chapter 4. Maps were obtained with natural weighing and using a Gaussian taper of 35 kλ, which gives a beam size of $6.3'' \times 4.4''$ (P.A. = 20.0°) for the NH_3 (1,1) transition maps and $6.3'' \times 4.3''$ (P.A. = 18.0°) for the NH_3 (2,2) transition maps. The *rms* noise level is 5 mJy beam^{-1} and 6 mJy beam^{-1} *per* channel for the NH_3 (1,1) and NH_3 (2,2) maps, respectively.

5.2.2 Plateau de Bure

The Plateau de Bure Interferometer (PdBI) observations and data calibration and reduction are described in Chapter 4. In this Chapter we present the spectral line data. N_2D ($1_{1,1}$–$1_{0,1}$) and $HN^{13}C$ (1–0) channel maps were obtained using MAPPING with natural weighting, that gives a synthesized beam (HPBW) of $7.0'' \times 2.9''$

(P.A. = 11°). We obtained additional N_2D ($1_{1,1}$–$1_{0,1}$) channel maps with uniform weighing that gives a synthesized beam (HPBW) of $6.3'' \times 2.7''$ (P.A. = 7.1°), which are presented in Chapter 7.

5.3 Results

Table 5.1: Interferometric observations.

Transition	ν (GHz)	Beam ($''\times''$)	PA (°)	rms (Jy beam^{-1})	Δv_{ch} (km s^{-1})	Telescope
NH_3 (1,1)	23.6945	6.4 × 4.2	17.2	4	0.30	VLA
NH_3 (2,2)	23.7226	6.3 × 4.3	18.3	5	0.30	VLA
$HN^{13}C$ (1–0)	87.0909	6.9 × 2.9	10.9	20	0.15	PdBI
NH_2D (1,1)	85.9263	7.1 × 2.9	10.0	23	0.15	PdBI

Table 5.2 lists the observational parameters of the transitions of the N-bearing species observed in the HH 80N region. All the listed species are detected in the 10.5 to 12.3 km s^{-1} velocity range. The integrated intensity maps are shown in Figure 5.1. The morphology of the integrated emission of the N-bearing species is consistent with the morphology seen in the maps of the species presented in Chapter 3, displaying the same elongated morphology along the SE-NW direction, and following approximately the dark lane seen in the *Spitzer* image. NH_3 (2,2) is detected marginally and shows two spots, one associated with IRS1 and other located ∼10″ to the east (hereafter, eastern hot spot, EHS).

Despite this similarity, the emission of the N-bearing species appears more compact than the emission size of the species of Chapter 3. NH_3 (1,1) is the most extended having a FHWM angular size of 50″× 15″. $HN^{13}C$ and NH_2D present smaller FHWM sizes of 25″× 10″. The maps of Fig. 5.1 also reveal two main trends: NH_3 (2,2) and $HN^{13}C$ peak at the IRS1 position while NH_3 (1,1) and NH_2D are brightest in the southeastern part of the core, around the Southeastern Condesnation (see Chapter 4, hereafter SE).

Figure 5.2 shows the channel maps over the 10.5 to 12.3 km s^{-1} velocity range, where most of the emission of the N-bearing species is detected, overlapped with

the continuum 3.5 mm PdBI map. There is an instrumental velocity shift between the PdBI and VLA data because our VLA observations were carried out during the VLA-EVLA transition, when the Doppler tracking was not available. Therefore, the NH_3 data will be excluded from the kinematic analysis presented in § 5.4.

From Fig. 5.2 we can compare the 3.5 mm continuum map (Chapter 4) with the emission of N-bearing molecules. From 10.5 to 11.4 km s^{-1} the emission of these molecules is mainly distributed to the southeast of IRS1, in the vicinity of SE. In the rest of channels, from 11.5 to 12.3 km s^{-1}, the emission is widely distributed from southeast up to regions northwest of IRS1 not traced by the 3.5 mm continuum emission. Besides, $HN^{13}C$ and NH_2D exhibit differences between them: while most NH_2D emission appears concentrated in the southeast of the core, $HN^{13}C$ emission is present in more channels than NH_2D and shows discrete peaks one of them coinciding with IRS1. In Figure 5.3 we show the maps of the first-order moment (bottom panel) and second-order moment (top panel) overlapped with the zero-order moment. This figure reproduces the distinctive properties of line emission between the blue-shifted and red-shifted channels of Fig. 5.2: the eastern part of the HH 80N core is blue-shifted about 0.5 km s^{-1} and presents significant line broadening with respect the western part. Interestingly, IRS1 is located in the transition between these two velocity shifts.

In order to compare the kinematics of the HH 80N core traced by N-bearing species with the kinematics derived in Chapter 3, in Figure 5.4 we show the channel maps of the same lines of Figure 5.2 overlapped with the BIMA CS channel maps. The channel maps of all the species of this figure have the same angular resolution corresponding to the angular resolution of the BIMA CS data. As seen in the Figure, while NH_3 (1,1) shows similar extension than CS along the channels, the rest of lines have more compact sizes. This is clearly seen for NH_2D that only shows emission in the channels with the brightest CS emission. Also, while the extension of $HN^{13}C$ blue-shifted emission toward the east is comparable to CS, NH_2D has few emission further east than SE.

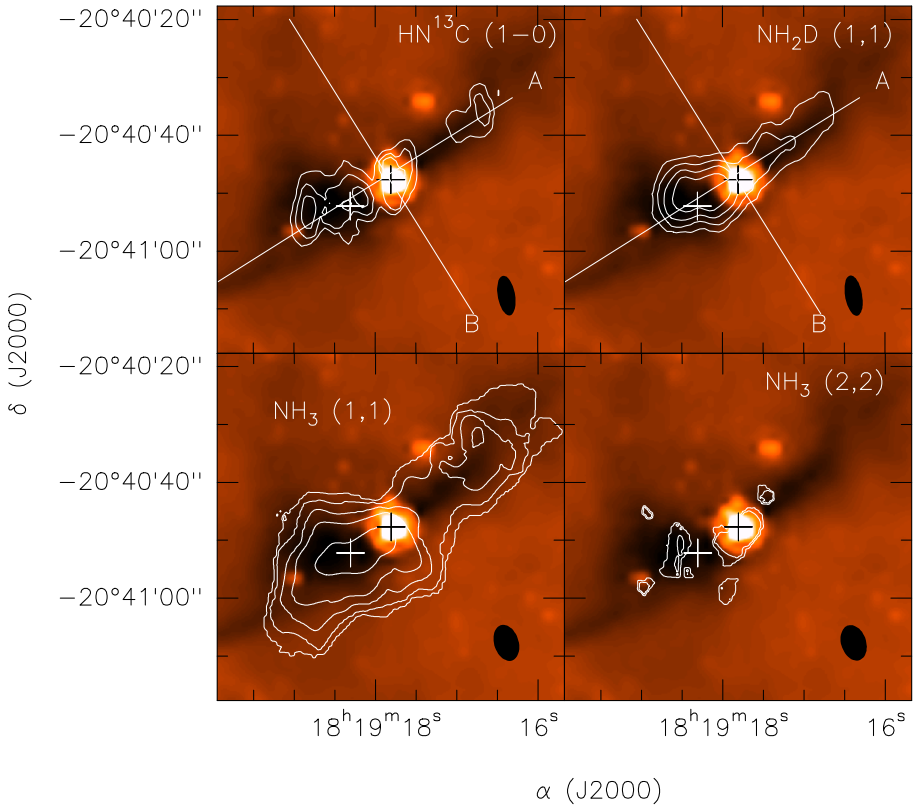

Figure 5.1: Superposition of the Spitzer 8 μm image (color scale) and the zero-order moment (integrated emission; white contours) of the N-bearing species observed in the HH 80N core with VLA and PdBI. The integrated emission of NH_3 (1,1) and NH_3 (2,2) corresponds to the main line of the transition. The contour levels are 3, 7, 12, 18 and 30 times 2 mJy beam^{-1} kms^{-1} (NH_3 (1,1) and NH_3 (2,2)) and 10 mJy beam^{-1} kms^{-1} ($HN^{13}C$ and NH_2D). For $HN^{13}C$ and NH_3 (2,2), the contours of the 4 and 5 times the nominal level of integrated emission were added, respectively. The solid lines show the cuts for the A and B direction PV plots of Figs. 5.5 and 7.4 (see Chapter 7). The crosses mark the positions of IRS1 and SE. The beam is shown in the bottom right corner of each panel.

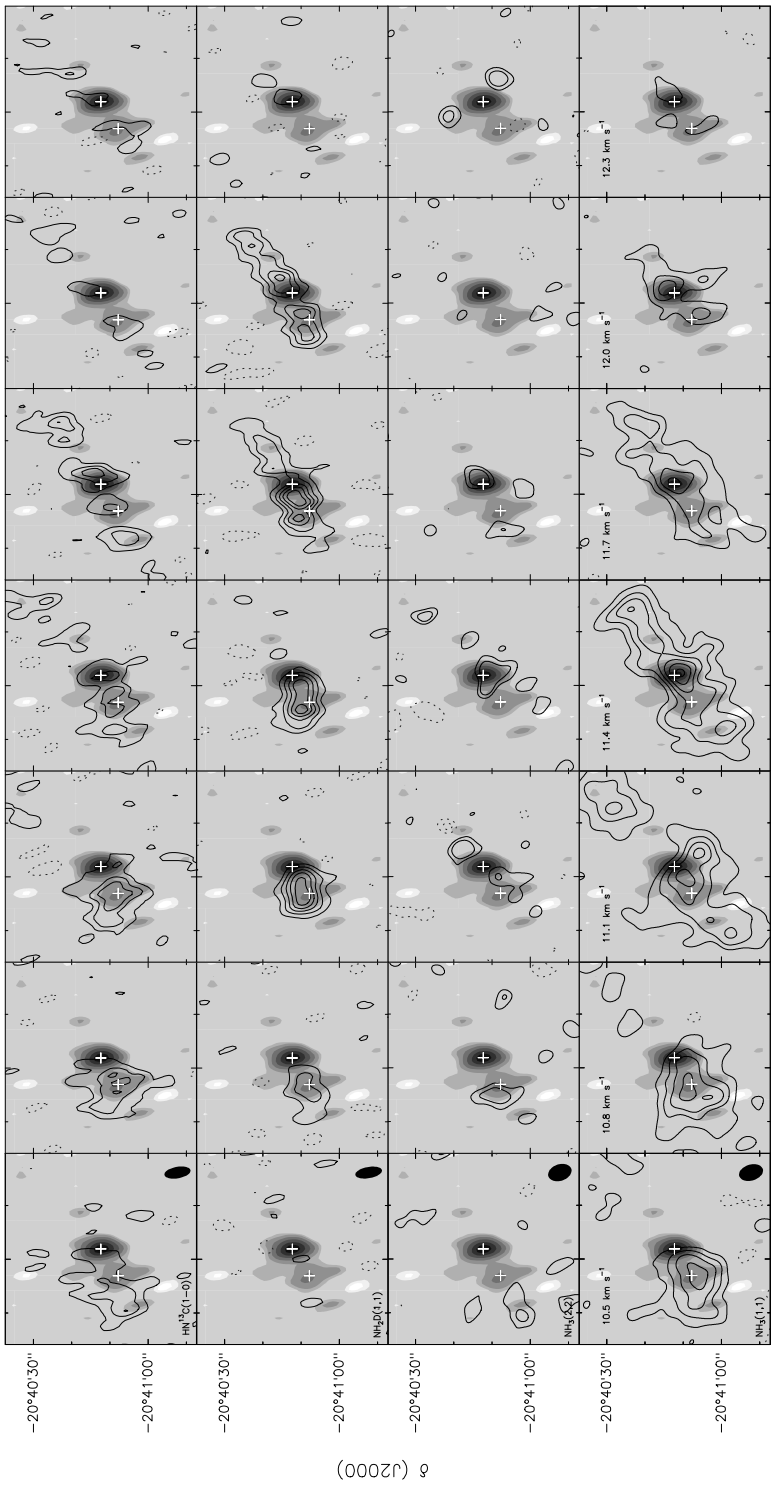

Figure 5.2: Channel velocity contour maps of the (from top to bottom) $HN^{13}C$ (1–0), NH_2D (1,1), NH_3(2,2) and NH_3(1,1) lines over the 10.5–12.3 km s^{-1} velocity range, with a velocity resolution of 0.3 km s^{-1}, superimposed over the 350 μm continuum PdBI map (gray scale, see Chapter 4). The contour levels are -3, 3, 6, 9, 12, 15 and 18 times the rms noise level for each species (see Table 5.2). For the NH_3 (2,2) line, the contours -2 and 2 times the rms noise level are also shown. The beam is shown in the bottom right corner of the first panel of each row. The white crosses mark the positions of IRS1 and SE.

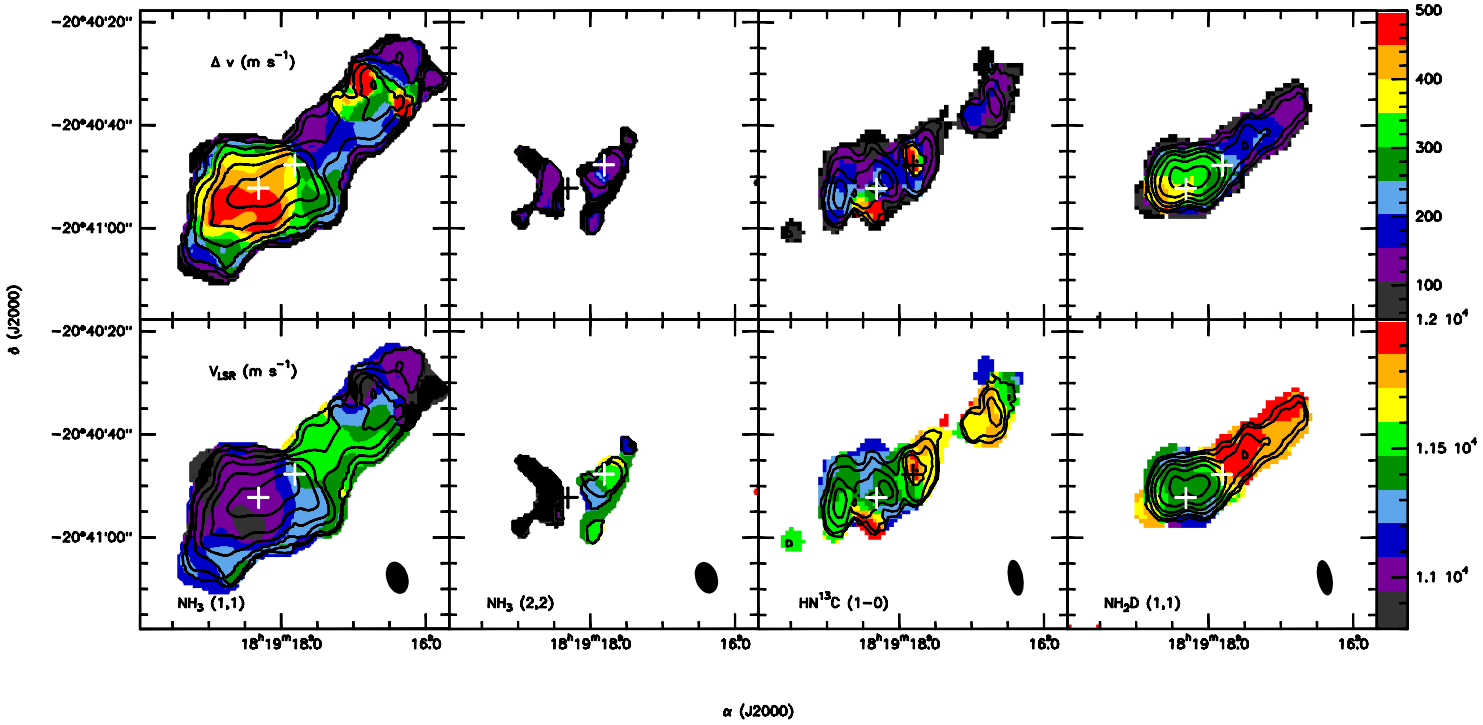

Figure 5.3: Superposition of the contour maps of the zero-order moment (integrated emission) with the color image of first-order (bottom panel) and second-order (top panel) maps of the (from left to right) NH_3 (1,1), NH_3(2,2), $HN^{13}C$ (1–0) and NH_2D (1,1) lines. The moment maps were obtained with the 10.5–12.0 km s^{-1} $v_{\rm LSR}$ range for NH_3 (1,1), 10.2–12.0 km s^{-1} for NH_3(2,2), 10.4–11.9 km s^{-1} for $HN^{13}C$, and 10.8–12.3 km s^{-1} NH_2D. Contour levels of the integrated emission are 2, 3, 5, 7, 10 and 15 times 4 mJy beam^{-1} km s^{-1} (NH_3(1,1)), 3 mJy beam^{-1} km s^{-1} (NH_3 (2,2)), 15 mJy beam^{-1} km s^{-1} (NH_2D) and 10 mJy beam^{-1} km s^{-1} ($HN^{13}C$). The crosses show the positions of IRS1 and SE. The beam is shown in the bottom right corner of the bottom panels.

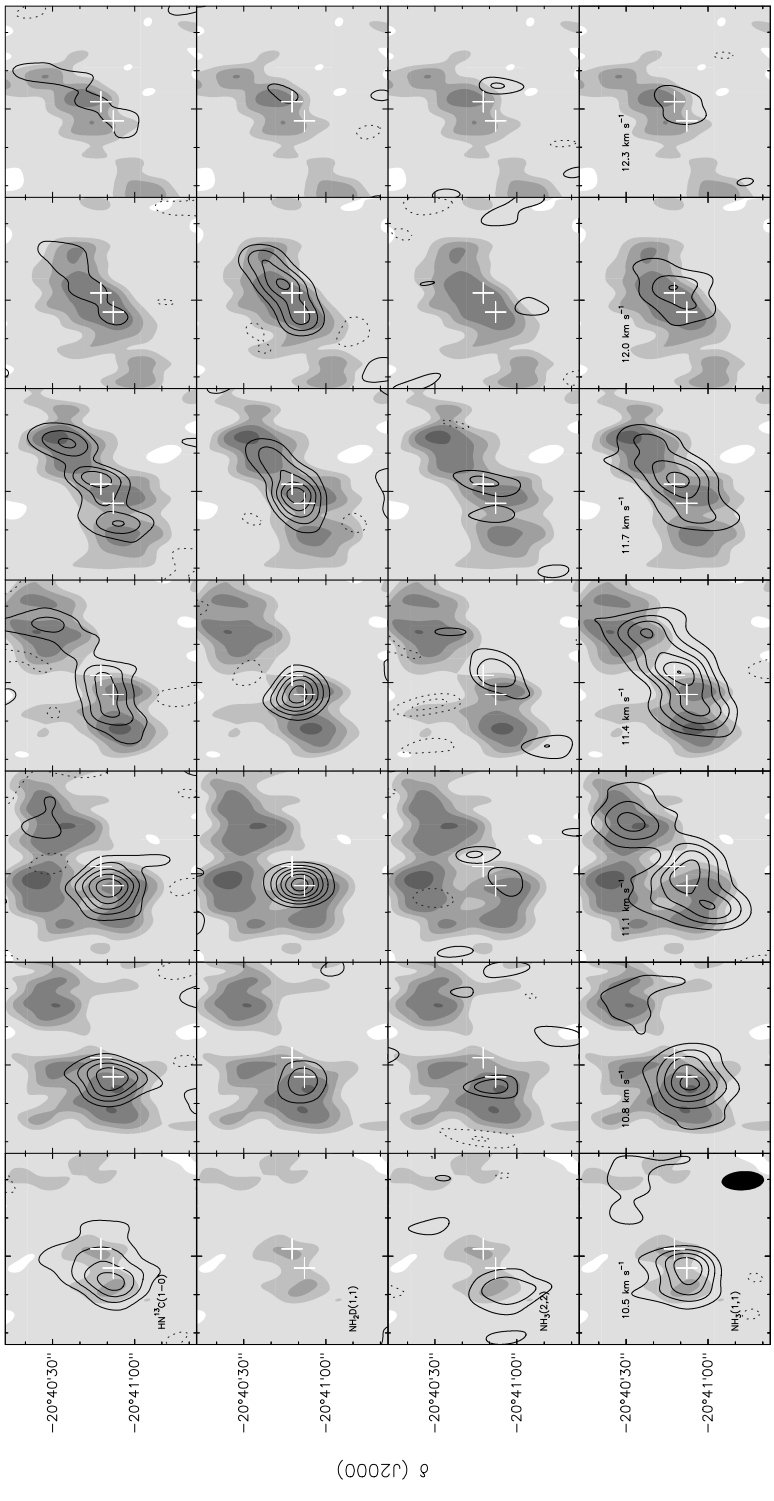

Figure 5.4: Channel velocity contour maps of the (from top to bottom) $HN^{13}C$, NH_2D, $NH_3(2,2)$ and $NH_3(1,1)$ lines over the 10.5–12.3 km s^{-1} velocity range, with a velocity resolution of 0.3 km s^{-1}, superimposed over the CS (2–1) BIMA channel maps (gray scale, see Chapter 3). The channel maps of N-bearing species were convolved to the synthesized beam of CS (2-1) BIMA channel maps obtained with natural weighting (15.6″×7.1″, PA. = 3°). The contour levels are -3, 3, 6, 9, 12, 15 and 18 times the rms noise level of the convolved map each species (9 mJy for NH_3 (1,1), 10 mJy for NH_3 (2,2), 32 mJy for NH_2D (1,1) and 30 mJy for $HN^{13}C$ (1–0)). For the NH_3 (2,2) line, the contours -2 and 2 times the rms noise level are also shown. The beam is shown in the bottom right corner of the first panel of the bottom row. The white crosses mark the positions of IRS1 and SE.

5.4 The contracting ring-like morphology

Figure 5.5 shows the comparison of the PV plots along the major (P.A. = 122°) and minor (P.A. = 32°) axes of the core (i.e. analogous to Chapter 3) of NH_2D and $HN^{13}C$ with respect to CS. To make an optimal comparison, the PV plots of NH_2D and $HN^{13}C$ were taken from their respective maps convolved to the synthesized beam of the BIMA CS channel maps obtained with natural weighting. Note that the cut along the major axis is shifted 4″ to the south with respect to the same cut presented in Chapter 3. The new cut trace better the emission of NH_2D and $HN^{13}C$ along the major axis of the core.

The quasi ring-like morphology seen in the CS PV plots along the major axis is identified in Chapter 3 as arising from a contracting ring-like structure perpendicular to the plane of the sky. This morphology is not a real structure but is the result of a strong molecular depletion at the inner and densest part of the core. N-bearing molecules do not deplete up to gas densities of $> 10^5$ cm^{-3} (Bergin et al. 1995; Aikawa et al. 2001), significantly higher than the depletion densities of CS. In addition, the improved angular resolution of the VLA and PdBI data with respect those of BIMA, allow us to resolve regions of 5000 AU of size, smaller than the diameter of the 'hole' of the ring. Therefore, for this scenario, $HN^{13}C$ and, specially, the NH_2D emission is expected to be more compact and closer to IRS1 than CS. This is clearly seen in Figs. 5.4 and 5.5. However, the morphology of $HN^{13}C$ and NH_2D in the major axis PV plot should follow a ring-like shape with a velocity range at least as large as the one observed in the CS emission. This is not seen in Fig. 5.5 where, instead, the PV plot for the NH_2D has an inverse L-shaped morphology encompassing the SE and IRS1 dusty sources. The $HN^{13}C$ PV plot resembles the $H^{13}CO^+$ and C_3H_2 PV plots shown in Chapter 3 (Fig. 3.4).

The PV plots along the minor axis show that $HN^{13}C$ and NH_2D have smaller radial velocities than CS and do not show the double peak expected for a contracting ring. If the ring is contracting as a result of gravitational collapse, the radial velocity of the gas is expected to increase at small core radii. This is not observed with neither NH_2D nor $HN^{13}C$ that trace regions of the core more compact and closer to IRS1 than CS. Therefore, the shape of the NH_2D emission in the PV plots along the major and minor axis questions the assumed scenario where the molecular core traces a flattened structure perpendicular to the plane of the sky and that it is

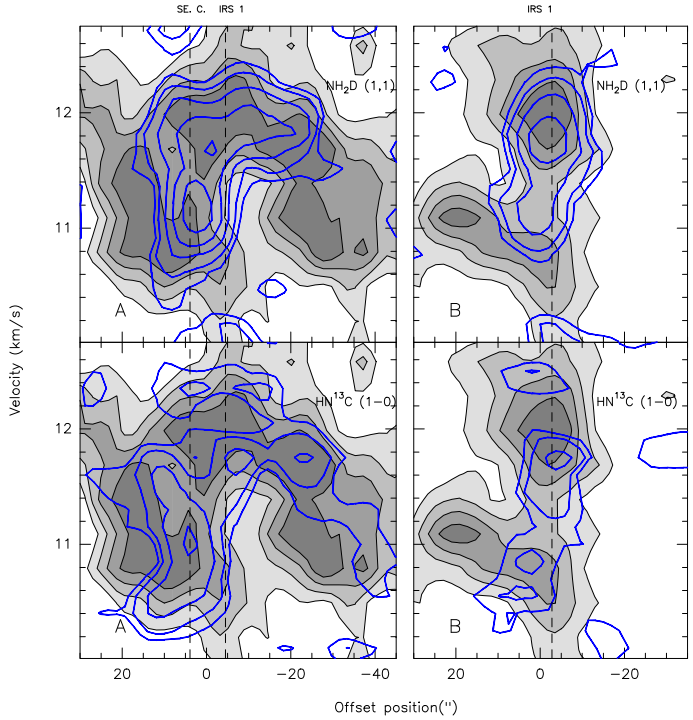

Figure 5.5: PV plots of the NH_2D (1,1) emission (top panels, blue contours) and $HN^{13}C$ (1-0) emission (bottom panels, blue contours) superimposed over the PV plots of the CS (2-1) emission (black contours and gray scale). The panels on the left represent the PV plots along the major axis of the core (PA = 122°, A direction) and the panels on the right represent the PV plots along the minor axis (PA = 32°, B direction). The positive offsets of the PV plots correspond to the southeast and northeast for the directions A and B, respectively. The PV plots of NH_2D (1,1) and $HN^{13}C$ (1-0) are obtained from their respective maps convolved to the synthesized beam of CS (2-1) BIMA channel maps obtained with natural weighting (15.6″×7.1″, P.A. = 3°). The contour levels are 3, 6, 12, 20 and 30 times 20 mJy beam^{-1} for NH_2D and 13 mJy beam^{-1} for $HN^{13}C$; 3, 6, 9 and 12 times 130 mJy beam^{-1} for CS (2–1). The position offsets of IRS1 and SE are marked with dashed lines.

infalling supersonically towards IRS1.

Figure 5.5 illustrates how different molecular species trace different parts of the core. While deuterated ammonia traces the dense gas of the HH 80N core, except at IRS1 where is possibly depleted (see § 5.5), CS is the most extended tracer and its emission possibly comes from the extended envelope of the HH 80N core with moderate density.

5.5 Column densities

Apart from the kinematic information, the molecular species presented in this chapter provide information on the column densities in the densest regions of the core, where the most evolved condensations, either prestellar or already with embedded objects (IRS1), are found. In particular, the deuterium enrichment is a well suited indicator of the chemical evolution of cores at these stages of low-mass star formation and, thus, it is related to the contraction history of the HH 80N core.

In Table 5.2 we list the excitation temperature, main line opacity of NH_2D (1,1) and NH_3 (1,1), rotational temperature, NH_2D and NH_3 column densities, and $D_{\rm frac}$ (i.e. the ratio of NH_2D vs. NH_3 column densities) obtained in EHS (see § 5.3), SE and IRS1. The NH_2D and NH_3 column densities were obtained following Busquet et al. (2010) and Palau et al. (2007), respectively. NH_3 (1,1) and NH_2D (1,1) have low opacity practically in all the core, which makes difficult the fit of the spectra with CLASS and therefore, the estimation of the column density. Thus, we focus our analysis on the discrete positions mentioned above where we derived reliable opacity values to calculate column densities, except for the NH_2D column density at IRS1, which was obtained assuming optically thin conditions. The NH_3 (2,2) transition is detected marginally in the HH 80N region and we only could obtain $T_{\rm rot}$ values at IRS1 and EHS. We assumed a value of 12 K for $T_{\rm rot}$ at SE.

Our derived column densities are in agreement with the typical values found in star forming regions: $\sim 10^{13}$–10^{14} cm^{-2} for NH_2D (Saito et al. 2000; Tiné et al. 2000; Roueff et al. 2005; Busquet et al. 2010) and $\sim 10^{14}$–10^{15} cm^{-2} for NH_3 (Palau et al. 2007; Busquet et al. 2009, 2010; Ruoskanen et al. 2011). With the exception of IRS1, the HH 80N core has a general high degree of deuteration being among the highest values derived in star forming regions (Fontani et al. 2008; Busquet et al. 2010)

Table 5.2: Summary of the results of the NH_3 and NH_2D analysis.

Position	Coordinates		T_{ex} [a]	τ_m (NH_2D)	τ_m (NH_3)	T_{rot} [b]	$N(NH_3)$	$N(NH_2D)$	D_{frac}^d
	α (J2000)	δ (J2000)	(K)			(K)	(10^{14} cm^{-2})	(10^{14} cm^{-2})	
EHS	$18^h19^m18^s.58$	$-20°41'58''.0$	5.6 ± 0.4	1.33 ± 0.42	4.83 ± 1.30	14.6 ± 2.5	5.2 ± 0.1	2.3 ± 0.7	0.4 ± 0.1
SE	$18^h19^m18^s.31$	$-20°41'52''.2$	6.9 ± 3.6	0.43 ± 0.28	3.27 ± 1.39	12.0 [c]	4.9 ± 0.1	0.6 ± 0.4	0.13 ± 0.08
IRS1	$18^h19^m17^s.69$	$-20°41'59''.8$	≤ 8	≤ 0.1	0.38 ± 0.08	16.7 ± 1.3	4.7 ± 0.1	≤ 0.6	≤ 0.13

Notes.

[a] Excitation temperature derived from NH_2D.

[b] Rotational temperature derived from NH_3.

[c] Assumed value.

[d] $D_{frac} = N(NH_2D)/N(NH_3)$.

Variations of $D_{\rm frac}$ over star forming regions are related with the evolutionary stage of the dense gas and values up to 10% are predicted (Penzias et al. 1977; Wootten et al. 1982). Furthermore, in the most evolved low-mass cores, values up to 40% have been found (Crapsi et al. 2005). While in massive star forming regions factors like high gas temperature and UV radiation may mislead the interpretation of this trend, the gas within the HH 80N core is mainly cold and has quiescent conditions. The star forming signatures of IRS1 only affect a small part of the core whereas the UV irradiation effect of HH 80N is present further east than SE, where we find slight heating ($\sim$14 K). Therefore, at EHS, the deuterium chemistry might be altered by the UV irradiation. On the other hand, NH_2D emission around SE comes from regions shielded from the UV radiation field. The $D_{\rm frac}$ enhancement at SE with respect to IRS1 can be attributed to different evolutionary stages, being SE prestellar and IRS1 protostellar. At the highest high angular resolution possible (done with uniform weighting) the NH_2D shows a lack of emission or a *hole* in IRS1 (see Fig. 7.4). This could be a sign of NH_2D destruction due to the increase of temperature produced by the protostellar object.

The fact that the NH_2D spectra show the most compact emission and has the most narrow linewidths among all the species of our molecular dataset (see Chapter 7) indicates that SE is found at the verge of gravitational collapse (e.g., Crapsi et al. 2005) and close to form a protostar. Also, chemical models show that the high density regime for the gas within prestellar cores should last about 1 Myr to produce significant abundance of NH_2D (Caselli et al. 2002). This value is an order of magnitude larger than the dynamical age of the HH 80/81/80N outflow, as shown in Chapter 2. Therefore, regardless the relative evolutionary state of the condensations of the HH 80N core, the presence of NH_2D in the core implies that it was formed before the jet arrival.

Chapter 6

Single-dish observations of the molecular envelope of the HH 80N core

6.1 Introduction

The basic units of low-mass star formation are small ($\sim$ 0.15 pc in diameter) cold ($10-15$ K) and dense ($2\times10^3-2\times10^5$ cm^{-3}) cores (Benson and Myers 1989) that differ significantly from the parental cloud from which they form out. A possible connection between these two regimes implies the condensation of velocity-coherent filaments out of less dense surrounding gas followed by turbulence dissipation and quasi-static fragmentation of these filaments (Hacar and Tafalla 2011). Indeed, dense cores are usually found embedded within larger structures and filaments (Schneider and Elmegreen 1979).

High resolution PdBI observations reveal that the HH 80N core is composed of several condensations suggesting possible fragmentation for this core. One of this condensations has associated an embedded object (IRS1) while another has prestellar nature but it is likely close to collapse (SE). These condensations are surrounded by moderate dense gas, mostly traced of CS, having this molecule the most extended emission among the species of our molecular dataset. This extended CS component constitutes a molecular envelope, gravitationally unbound from IRS1,

which seems to be affected by the HH 80/81/80N jet. The properties of the molecular envelope of HH 80N core may be inherited to these internal condensations.

In order to study the physical and chemical properties of the envelope of the HH 80N core, we carried out a molecular survey with IRAM 30m and MOPRA. In this chapter we analyze the molecular line data observed at several positions in the molecular envelope. In some cases, several transitions of a single specie (and isotolopogues) were obtained allowing us to infer the excitation conditions of the molecule and estimate the gas physical properties, such as density and temperature, as well as chemical abundances. We also discuss the chemistry properties based on the comparison with the appropriate chemical models (Aikawa et al. 2005).

6.2 Observations and Results

6.2.1 IRAM 30m

We observed the HH 80N region in four observing runs at the IRAM 30m radio telescope on Pico Veleta. The first observing run took place in 2006 September. The weather conditions were generally good but variable. The precipitable water was always $\lesssim$ 5 mm and the zenith opacity ranged between 0.05 and 0.25. The system temperatures ranged between $T_{\rm sys} \sim$ 150-450, 150-1600, 500-2000 and 520-2200 K for the 100 GHz, 150 GHz, 230 GHz and 270 GHz frequency bands, respectively. Due to the low source elevation ($< 30°$), the system temperatures of the receivers tuned to high frequencies ($>$ 150 GHz) were extremely high in the last scans of the run. The second observing run took place in the second observing week of the summer HERA pool in 2007 (October 30 - November 6). The weather was good with system temperatures ranging form $T_{\rm sys} \sim$ 160-600, 350-700, 700-1000 and 1000-1050 K for the 100 GHz, 150 GHz, 230 GHz and 270 GHz frequency bands, respectively, the zenith opacity ranging from 0.05 to 0.32 and the precipitable water was always $\lesssim$ 6 mm. The third run took place in 2008 September under very poor weather conditions. The zenith opacity and precipitable water were always $>$ 0.2 and $>$ 8 mm, respectively. The system temperatures were typically $\sim$ 200 K at 3 mm and $\sim$ 1600 K at 1 mm. During the first 3 observing runs, we used the four AB receivers simultaneously in three different configurations covering several molecular transitions at 3 mm, 2 mm and 1 mm.

Table 6.1: Summary of the lines observed with IRAM 30m.

Transition	Frequency (GHz)	Beam ($''$)	Beam Eficiency	Δv_{ch} (km s^{-1})	Observing Epoch	Positions[a] Observed
^{34}SO ($3_2 \rightarrow 2_1$)	97.715401	25.5	0.75	0.240	Sep 2006, May 2009	C, E, W, NB
SO($3_2 \rightarrow 2_1$)	99.29988	25.1	0.75	0.236	Sep 2006	E, W, NB
^{34}SO ($2_3 \rightarrow 1_2$)	106.743374	23.6	0.74	0.219	Sep 2006	E, W, NB
SO($2_3 \rightarrow 1_2$)	109.252112	23.0	0.73	0.214	Nov 2007	E, W, NB
SO($3_4 \rightarrow 2_3$)	158.971853	15.8	0.66	0.147	Sep 2006	E, W, NB
SO($5_5 \rightarrow 4_4$)	215.220708	11.7	0.58	0.109	Sep 2006	E, W, NB
SO($6_5 \rightarrow 5_4$)	219.949433	11.4	0.58	0.107	Sep 2006	E, W, NB
C^{34}S ($2 \rightarrow 1$)	96.412982	25.9	0.75	0.243	Nov 2007, Sep 2008, May 2009	C, E, W, NB
CS($2 \rightarrow 1$)	97.98097	25.4	0.75	0.239	Nov 2007, May 2009	C,E, W, NB
C^{34}S ($3 \rightarrow 2$)	144.617114	17.1	0.68	0.162	Nov 2007, May 2009	C, E, W, NB
CS($3 \rightarrow 2$)	146.969049	17.3	0.68	0.159	Sep 2006	E, W, NB
CS($5 \rightarrow 4$)	244.935606	10.2	0.54	0.096	Sep 2006, May 2009	C, E, W, NB
C_2S ($6_7 \rightarrow 5_6$)	86.181413	29.0	0.78	0.272	Sep 2008, May 2009	E, W, C
SO_2 ($3_{1,3} \rightarrow 2_{0,2}$)	104.029410	24.2	0.74	0.225	Sep 2006	E, W, NB
SO_2 ($3_{2,2} \rightarrow 2_{1,1}$)	208.700323	12.0	0.59	0.112	Sep 2006	E, W, NB
H_2S ($1_{1,0} \rightarrow 1_{0,1}$)	168.762762	14.8	0.63	0.139	Sep 2006	E, W, NB
DCO$^+$ ($3 \rightarrow 2$)	216.112582	11.5	0.55	0.108	Sep 2006	E, W, NB
N_2D^+ ($3 \rightarrow 2$)	231.321635	10.8	0.55	0.101	Nov 2007, Sep 2008	C, E, W, NB

Notes.

[a] E, C (IRS1), W and NB stands for East Ring, CB and CR-Ring, West Ring and NB clump, repectively (see Table 3.2).

The fourth observing run took place in 2009 May under good weather conditions with values for the zenith opacity of $0.05 < \tau < 0.17$ and precipitable water ~ 2 mm. We used the EMIR (Eight MIxer Receiver) receivers that provide improved sensitivities with respect to the old heterodyne receivers: the system temperatures were typically ~ 100 K at 3 mm, ~ 130 K at 2 mm and ~ 300 K at 1 mm.

In all the observing runs we set the VESPA backend with a bandwidth of 80 MHz and a spectral resolution of 40 kHz. We used the frequency-switching mode with a frequency throw of 3.9 MHz. We performed pointing every 1.5-2 hours using the QSO J1757-240 source. We obtained pointing accuracies $\lesssim 3''$, except for the second run that was degraded to $5''$ due to anomalous refraction. The telescope focus was checked several times a day, in particular, after sunrise and sunset.

We observed several discrete positions within the core. The observed molecular transitions as well as positions are summarized in Table 6.1. The positions are representative of clumps located in several parts of the HH 80N core that appear in the BIMA channel maps and were defined in Chapter 3 as Eastern Ring, CR-Ring and CB-Ring, Western Ring and NB clump (see Table 3.2). Comparing these positions with the clumps found in Chapter 4, we can see that the CR-Ring and CB-Ring position in the sky coincides with the position of the IRS1 embedded object, while SE is located between the Eastern Ring and Center Ring positions. Only at 3 mm, the spectra taken at both positions includes SE emission because of the large IRAM 30m beamsize at long wavelengths. For simplicity, in this chapter we refer to the positions observed with single-dish telescopes as East (East Ring), West (West Ring), Center (CB-Ring and CR-Ring) and North (NB clump) positions. Figure 6.1 (upper panel) plots the location of the observed positions over the integrated CS (2-1) BIMA map smoothed to the angular resolution of IRAM 30m observing at 3 mm. The data were reduced, analyzed and displayed using the GILDAS software. The spectra of different observing runs corresponding to the same transition line were averaged in each position and weighted with the system temperature.

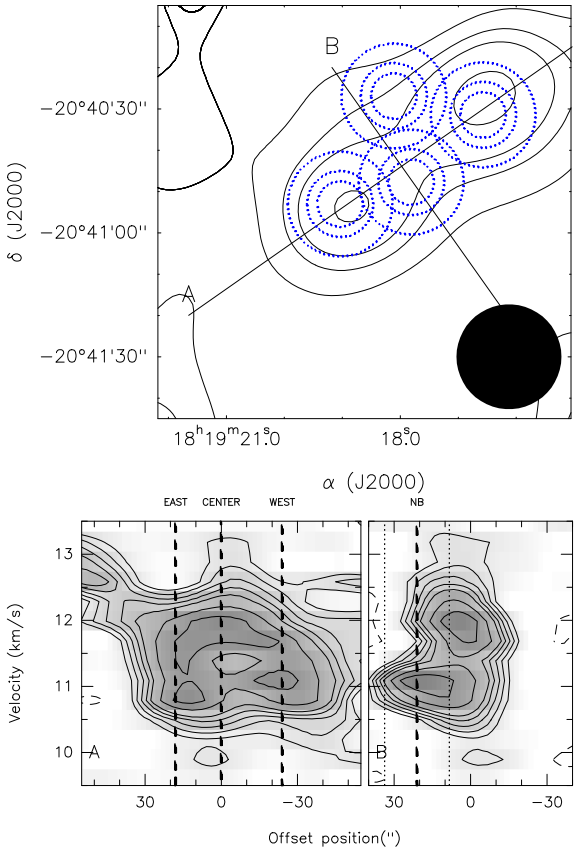

Figure 6.1: *Top panel*: Location of the positions observed with the IRAM 30m telescope overlapped with the contour map of the CS (2–1) emission of the 11.7 km s^{-1}channel of the HH 80N core observed with BIMA. The map has been convolved to the beamsize of the IRAM 30m at the frequency of the CS (2–1) transition. The contours are 3, 5, 9, and 13 times 0.3 $\mathrm{Jy\ beam^{-1}}$. Each position observed is indicated with three concentric circles that represent the approximate IRAM 30m beam sizes (from inside out) at 1, 2 and 3 mm. The solid lines represent the major (A, P.A.=122°) and minor (B, P.A.=32°) axes of the core. The beam of the map is shown in the bottom right corner. *Bottom panels*: PV plots of the CS (2-1) emission shown in the top panel along major (A, left panel) and minor (B, right panel) axes of the core. The contours are 4, 6, 8, 10, 12 ,16 and 20 times 0.3 $\mathrm{Jy\ beam^{-1}}$. The origin of position offsets of the PV plots are the intersection of the lines in the top panel and the positive offsets correspond to the northeast and southeast directions for the minor and major axes, respectively. The dashed lines represent the positions observed with the IRAM 30m telescope and the pointed lines (right panel) delimit the size of the IRAM 30m beamsize at the frequency of the CS (2–1) transition.

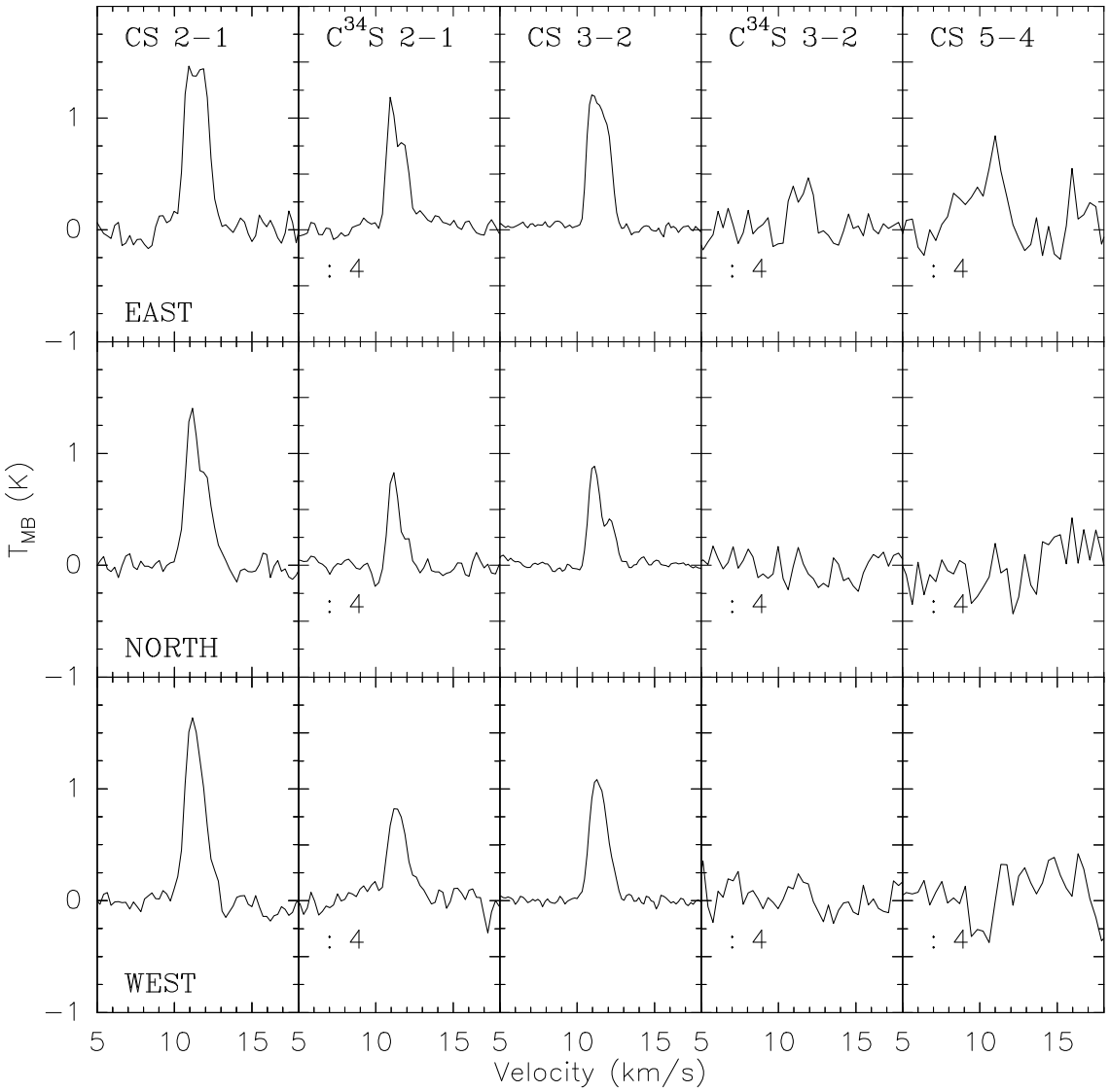

Figure 6.2: Spectra (smoothed to ~ 0.3 km s^{-1} of spectral resolution) of the transitions of CS and C^{34}S observed with the IRAM 30m telescope at the East (top row), North (middle row) and West (bottom row) positions in the HH 80N core. The brightness scale of the spectra must be divided by 4 except for the CS (2–1) and CS (3–2) lines.

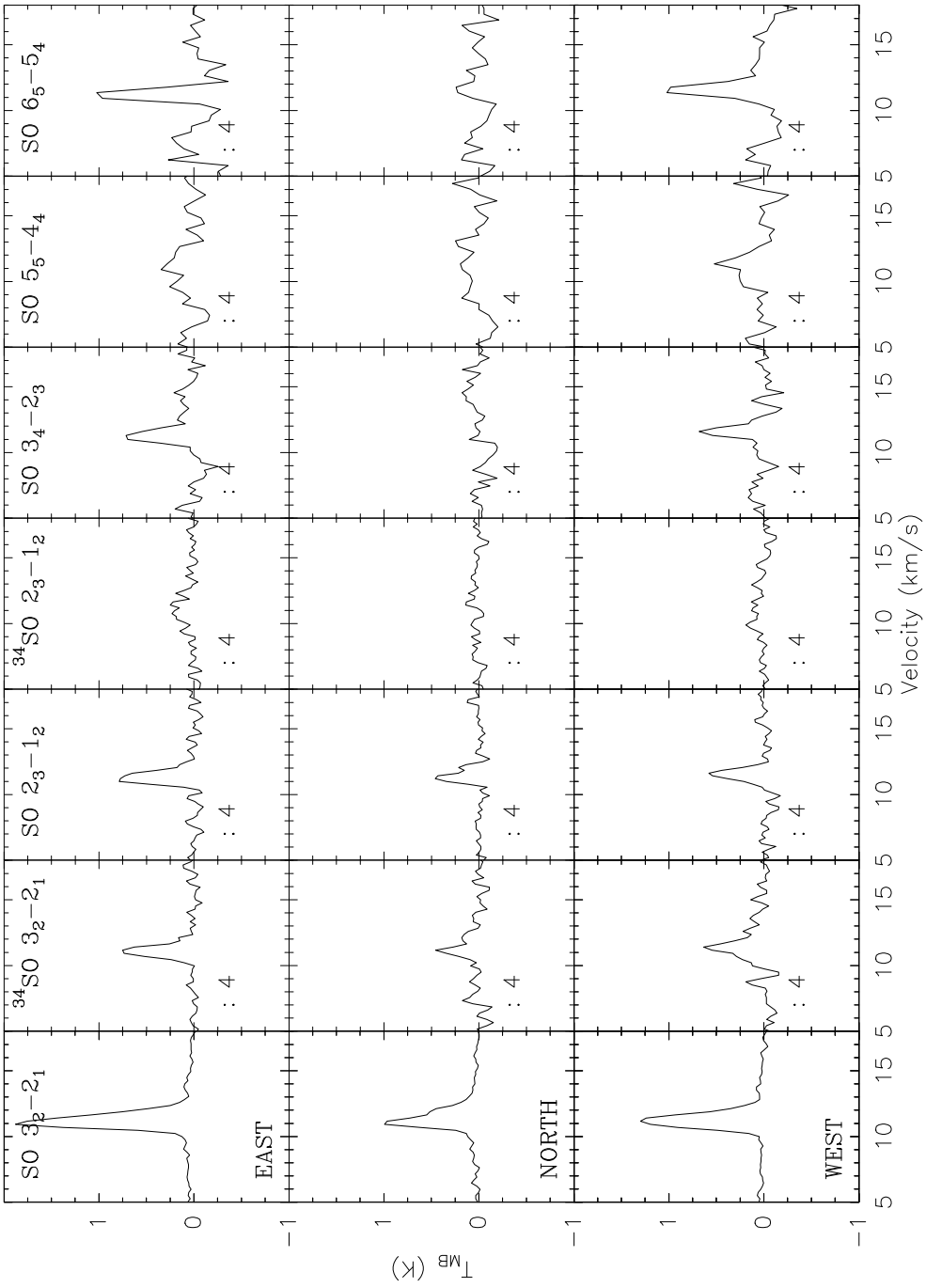

Figure 6.3: Spectra (smoothed to ~ 0.3 km s^{-1} of spectral resolution) of the transitions of SO and ^{34}SO observed with the IRAM 30m telescope at the East (top row), North (middle row) and West (bottom row) positions in the HH 80N core. The brightness scale of the spectra must be divided by 4 except for the first column.

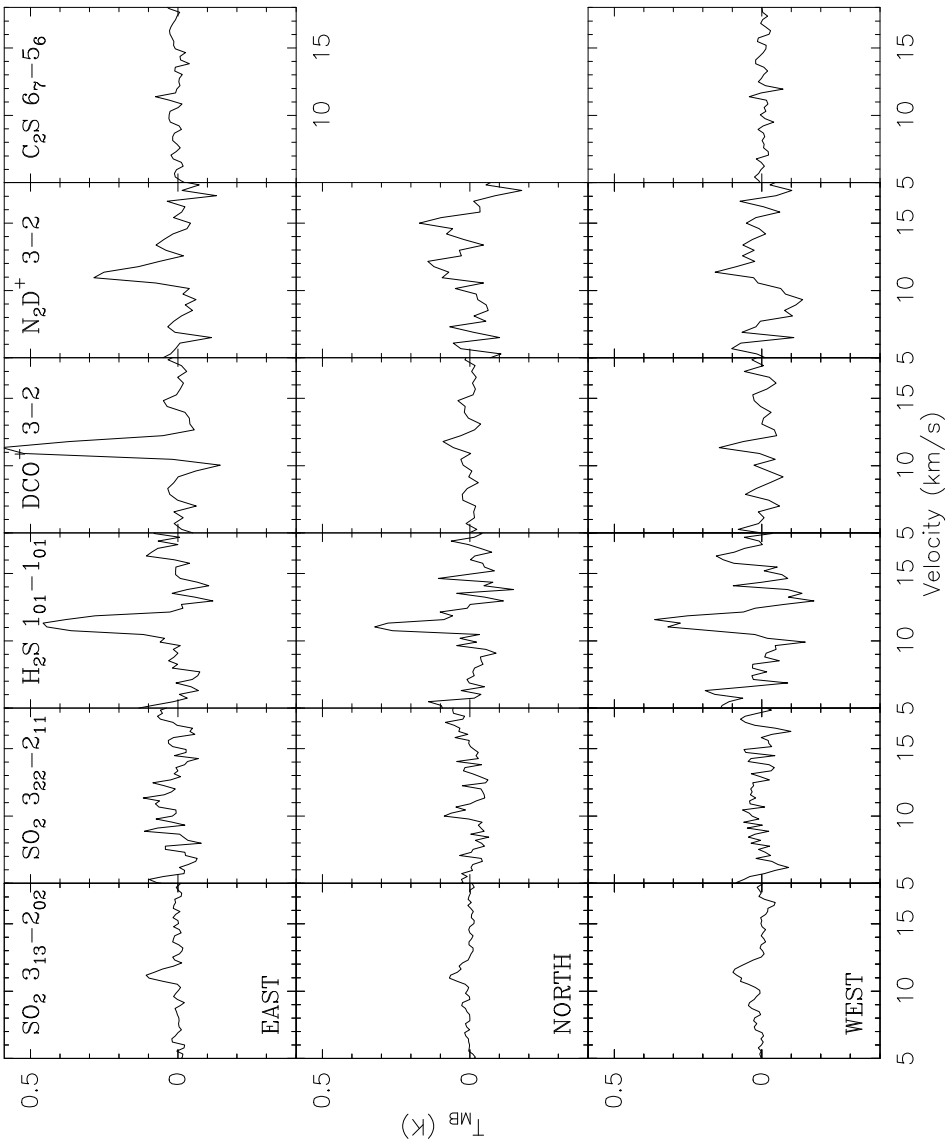

Figure 6.4: Spectra (smoothed to ~ 0.3 km s^{-1} of spectral resolution) of the transitions of SO_2, H_2S, DCO^+, N_2D^+ and C_2S observed with the IRAM 30m telescope at the East (top row), North (middle row) and West (bottom row) positions in the HH 80N core.

The IRAM 30m spectra are shown in Fig. 6.2, Fig. 6.3, Fig. 6.4 and Fig. 6.5. The most remarkable result in these figures is that the spectra have either two velocity components or present non-Gaussian shapes at all the positions except for the West. This is specially evident for the CS lines. Most of the 2 mm and 3 mm lines are clearly detected. However, most of the 1 mm lines are only marginally detected. Tables 6.2, 6.3, 6.4 and 6.5 give the Gaussian fit results of the lines observed with the IRAM 30m: the integrated area, the velocity of the line, the linewidth, the peak brightness temperature and *rms* noise of the spectra. For most species, the intensities are highest at East and lowest at NB. Linewidths are relatively narrow in all the positions (~ 1 km s^{-1}).

In order to interpret the spectra on basis of the data presented previously, we show the PV plots (Fig. 6.1, lower panels) obtained from the cuts along the directions A and B over the BIMA CS (2−1) channel maps. The BIMA CS data were convolved to the beamsize of the IRAM 30m observing at 3 mm. Taking into account the PV plot appearance, the observed spectra can be described as:

- *East position.* It has a double peak at 10.9 km s^{-1} and 11.9 km s^{-1}, specially seen at 3 mm with CS, which can be associated with the SE condensation and emission coming from rest the HH 80N core, respectively.

- *North position.* The spectra are composed of a narrow component with 11.1 km s^{-1} of systemic velocity, corresponding to the NB clump independent of the HH 80N core defined in Chapter 3. The broader and weaker component seen at velocities of 12.1 km s^{-1} is associated with the HH 80N core.

- *West position.* Most of the spectra consist of a single component peaking at 11.2 km s^{-1}, although the systemic velocity may vary depending on the observed line. In this position there is no high density condensation associated. Therefore, the emission of the spectra corresponds to moderately dense gas belonging to the HH 80N core.

- *Center position.* This position coincides with IRS1 position. The CS spectra shows the presence of two velocity components at 10.9 km s^{-1} and 11.8 km s^{-1}. The CS (2–1) spectrum has a brightness temperature of 1.25 K, which is comparable to the with the brightness temperature of this line observed with BIMA at the same position and convolved to the IRAM 30m beam. This

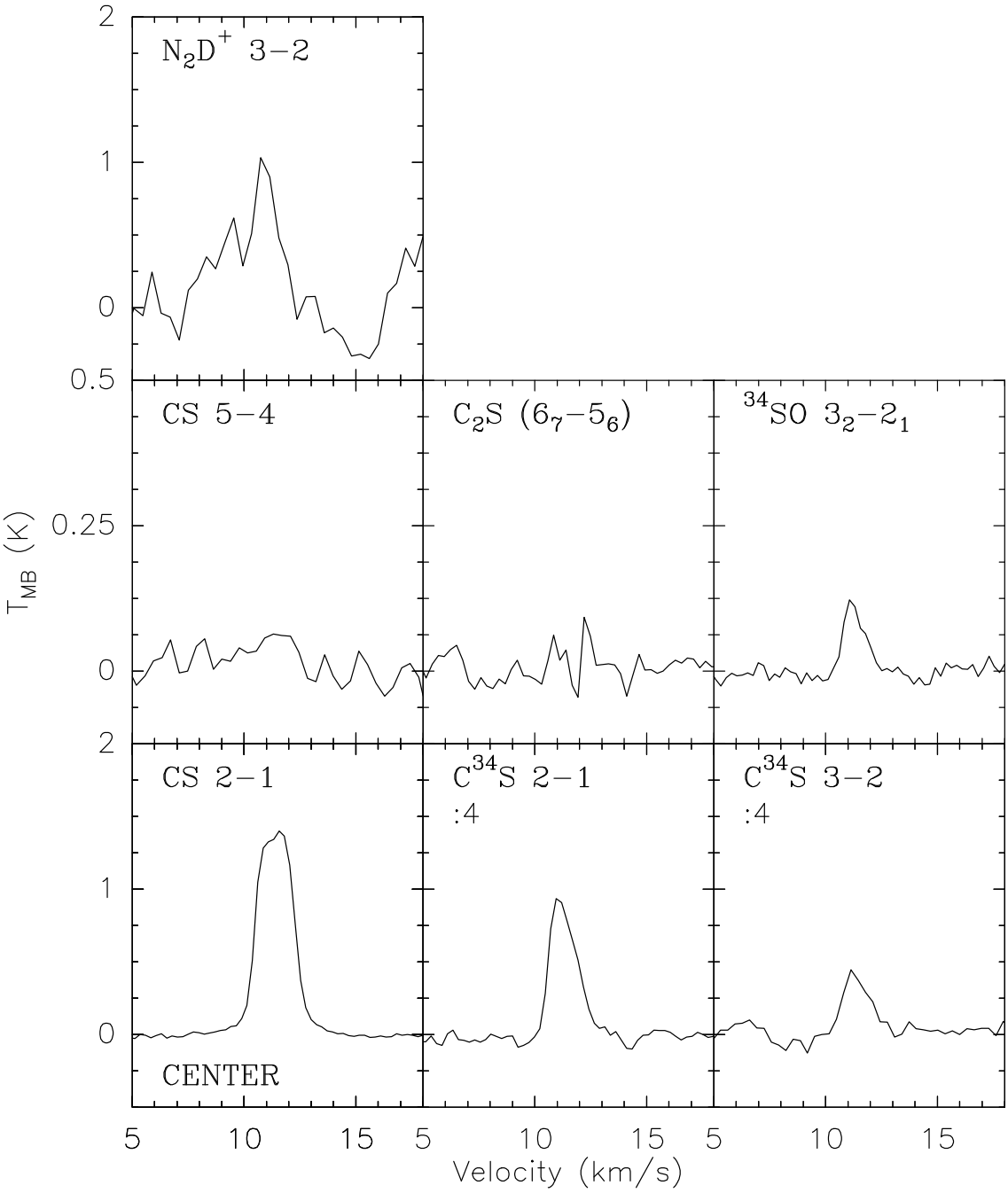

Figure 6.5: Spectra (smoothed to ~ 0.3 km s^{-1} of spectral resolution) of the transitions of CS, $C^{34}S$, ^{34}SO, C_2S and N_2D^+ observed with the IRAM 30m at the Center position in the HH 80N core. The brightness scale of $C^{34}S$ (2–1) and $C^{34}S$ (3–2) spectra must be divided by 4.

Table 6.2: Molecular line results for the species observed with IRAM 30 m at the East position[a].

Transition	$\int T_{\rm MB}{\rm d}v$ (K km s^{-1})	$v_{\rm LSR}$ (km s^{-1})	$\Delta v_{\rm LSR}$ (km s^{-1})	$T_{\rm MB}$ (K)	rms (K)
$SO(3_2 \rightarrow 2_1)$	1.746 (0.066)	11.005 (0.017)	0.898 (0.019)	1.827	0.040
	0.628 (0.052)	11.813 (0.045)	fixed	0.657	
$^{34}SO(3_2 \rightarrow 2_1)$	0.210 (0.01)	11.082 (0.023)	1.010 (0.057)	0.195	0.013
$SO(2_3 \rightarrow 1_2)$	0.130 (0.013)	11.057 (0.057)	0.638 (0.035)	0.191	0.014
	0.094 (0.010)	11.642 (0.047)	fixed	0.135	
$^{34}SO(2_3 \rightarrow 1_2)$	–	–	–	< 0.042	0.014
$SO(3_4 \rightarrow 2_3)$	0.215 (0.020)	11.266 (0.060)	1.061 (0.115)	0.191	0.032
$SO(5_5 \rightarrow 4_4)$	–	–	–	< 0.123	0.041
$SO(6_5 \rightarrow 5_4)$	0.259 (0.024)	11.185 (0.037)	0.739 (0.065)	0.330	0.062
CS(2→1)	1.356 (0.070)	10.952 (0.036)	0.908 (0.028)	1.403	0.016
	1.342 (0.068)	11.889 (0.031)	fixed	1.389	
$C^{34}S(2\rightarrow1)$	0.221 (0.010)	10.997 (0.032)	0.712 (0.022)	0.190	0.016
	0.149 (0.009)	11.848 (0.019)	fixed	0.292	
CS(3→2)	1.098 (0.021)	10.998 (0.010)	0.857 (0.010)	1.204	0.034
	0.862 (0.020)	11.868 (0.013)	fixed	0.944	
$C^{34}S(3\rightarrow2)$	0.007 (0.015)	10.891 (0.065)	0.514 (0.128)	0.122	0.034
	0.092 (0.018)	11.929 (0.065)	0.65 (0.139)	0.133	
CS(5→4)	–	–	–	< 0.180	0.060
$SO_2(3_{1,3} \rightarrow 2_{0,2})$	0.091 (0.009)	11.172 (0.032)	0.770 (0.071)	0.111	0.012
$SO_2(3_{2,2} \rightarrow 2_{1,1})$	–	–	–	< 0.168	0.056
$H_2S(1_{1,0} \rightarrow 1_{0,1})$	0.582 (0.043)	11.214 (0.041)	1.116 (0.085)	0.491	0.059
$DCO^+(3 \rightarrow 2)$	0.709 (0.041)	11.278 (0.027)	0.940 (0.055)	0.709	0.065
$N_2D^+(3 \rightarrow 2)$	0.321 (0.041)	11.197 (0.062)	0.951 (0.140)	0.318	0.087

Notes.

[a] For the spectra that present non-gaussian shapes we fitted two Gaussians with the same width. For the rest of spectra we fitted a single Gaussian

Table 6.3: Molecular line results for the species observed with IRAM 30 m at the North position[a].

Transition	$\int T_{\rm MB} dv$ (K km s^{-1})	$v_{\rm LSR}$ (km s^{-1})	$\Delta v_{\rm LSR}$ (km s^{-1})	$T_{\rm MB}$ (K)	rms (K)
$SO(3_2 \rightarrow 2_1)$	0.959 (0.032)	11.059 (0.015)	0.916 (0.022)	0.983	0.033
	0.415 (0.023)	12.076 (0.042)	fixed	0.425	
$^{34}SO(3_2 \rightarrow 2_1)$	0.084 (0.016)	11.085 (0.03)	0.785 (0.060)	0.107	0.017
	0.040 (0.009)	12.197 (0.110)	fixed	0.047	
$SO(2_3 \rightarrow 1_2)$	0.100 (0.06)	11.314 (0.038)	0.833 (0.099)	0.113	0.011
	–	–	–	< 0.033	
$^{34}SO(2_3 \rightarrow 1_2)$	–	–	–	< 0.039	0.013
$SO(3_4 \rightarrow 2_3)$	–	–	–	< 0.084	0.028
$SO(5_5 \rightarrow 4_4)$	–	–	–	< 0.123	0.041
$SO(6_5 \rightarrow 5_4)$	–	–	–	< 0.105	0.046
CS(2→1)	1.359 (0.136)	11.098 (0.029)	0.925 (0.029)	1.380	0.081
	0.705 (0.051)	12.110 (0.050)	fixed	0.716	
$C^{34}S$(2→1)	0.156 (0.021)	11.117 (0.025)	0.666 (0.028)	0.220	0.017
	0.043 (0.009)	11.933 (0.092)	fixed	0.064	
CS(3→2)	0.779 (0.016)	11.098 (0.009)	0.794 (0.010)	0.922	0.031
	0.384 (0.028)	12.144 (0.022)	fixed	0.410	
$C^{34}S$(3→2)	–	–	–	< 0.132	0.034
CS(5→4)	–	–	–	< 0.237	0.079
$SO_2(3_{1,3} \rightarrow 2_{0,2})$	0.080 (0.008)	11.185 (0.059)	1.237 (0.153)	0.061	0.011
$SO_2(3_{2,2} \rightarrow 2_{1,1})$	–	–	–	< 0.027	0.009
$C_2S(6_7 \rightarrow 5_6)$	–	–	–	< 0.051	0.017
$H_2S(1_{1,0} \rightarrow 1_{0,1})$	0.270 (0.030)	11.068 (0.049)	0.687 (0.106)	0.378	0.085
$DCO^+(3 \rightarrow 2)$	0.083 (0.019)	11.647 (0.083)	0.665 (0.146)	0.118	0.052
$N_2D^+(3 \rightarrow 2)$	–	–	–	< 0.297	0.099

Notes.

[a] For the spectra that present non-gaussian shapes we fitted two Gaussians with the same width. For the rest of spectra we fitted a single Gaussian.

Table 6.4: Molecular line results for the species observed with IRAM 30 m at the West position[a].

Transition	$\int T_{\rm MB} {\rm d}v$ (K km s^{-1})	$v_{\rm LSR}$ (km s^{-1})	$\Delta v_{\rm LSR}$ (km s^{-1})	$T_{\rm MB}$ (K)	rms (K)
$SO(3_2 \rightarrow 2_1)$	1.779 (0.027)	11.207 (0.023)	1.257 (0.023)	1.329	0.036
$^{34}SO(3_2 \rightarrow 2_1)$	0.235 (0.025)	11.267 (0.087)	1.560 (0.169)	0.141	0.017
$SO(2_3 \rightarrow 1_2)$	0.013 (0.010)	11.536 (0.030)	0.882 (0.068)	0.148	0.015
$^{34}SO(2_3 \rightarrow 1_2)$	–	–	–	< 0.039	0.013
$SO(3_4 \rightarrow 2_3)$	0.156 (0.015)	11.585 (0.037)	0.797 (0.096)	0.184	0.028
$SO(5_5 \rightarrow 4_4)$	0.153 (0.026)	11.387 (0.084)	1.136 (0.272)	0.126	0.040
$SO(6_5 \rightarrow 5_4)$	0.286 (0.023)	11.566 (0.030)	0.821 (0.089)	0.327	0.050
$CS(2 \rightarrow 1)$	1.671 (0.136)	11.088 (0.041)	1.030 (0.041)	1.502	0.075
	0.750 (0.116)	11.910 (0.078)	fixed	0.634	
$C^{34}S(2 \rightarrow 1)$	0.324 (0.018)	11.396 (0.038)	1.485 (0.156)	0.206	0.018
$CS(3 \rightarrow 2)$	1.020 (0.054)	11.176 (0.025)	0.964 (0.024)	0.995	0.034
	0.506 (0.047)	11.918 (0.042)	fixed	0.494	
$C^{34}S(3 \rightarrow 2)$	–	–	–	< 0.126	0.042
$CS(5 \rightarrow 4)$	–	–	–	< 0.246	0.082
$SO_2(3_{1,3} \rightarrow 2_{0,2})$	0.152 (0.024)	11.330 (0.066)	1.485 (0.150)	0.096	0.015
$SO_2(3_{2,2} \rightarrow 2_{1,1})$	–	–	–	< 0.081	0.027
$C_2S(6_7 \rightarrow 5_6)$	–	–	–	< 0.033	0.011
$H_2S(1_{1,0} \rightarrow 1_{0,1})$	0.513 (0.053)	11.402 (0.061)	1.132 (0.119)	0.426	0.075
$DCO^+(3 \rightarrow 2)$	0.105 (0.017)	11.426 (0.044)	0.508 (0.084)	0.195	0.053
$N_2D^+(3 \rightarrow 2)$	–	–	–	< 0.294	0.098

Notes.

[a] For the spectra that present non-gaussian shapes we fitted two Gaussians with the same width. For the rest of spectra we fitted a single Gaussian.

Table 6.5: Molecular line results for the species observed with IRAM 30 m at the Center position[a].

Transition	$\int T_{\rm MB} dv$ (K km s^{-1})	$v_{\rm LSR}$ (km s^{-1})	$\Delta v_{\rm LSR}$ (km s^{-1})	$T_{\rm MB}$ (K)	rms (K)
^{34}SO($3_2 \rightarrow 2_1$)	0.128 (0.006)	11.246 (0.026)	0.995 (0.058)	0.120	0.017
CS(2→1)	1.305 (0.010)	10.905 (0.005)	0.991 (0.005)	1.237	0.236
	1.350 (0.010)	11.856 (0.005)	fixed	1.279	
C^{34}S(2→1)	0.208 (0.014)	11.014 (0.032)	0.838 (0.033)	0.236	0.011
	0.111 (0.012)	11.819 (0.063)	fixed	0.124	
C^{34}S(3→2)	0.153 (0.009)	11.361(0.039)	1.349 (0.087)	0.107	0.020
CS(5→4)	–	–	–	< 0.213	0.071
$C_2S(6_7 \rightarrow 5_6)$	–	–	–	< 0.060	0.020
$N_2D^+(3 \rightarrow 2)$	–	–	–	< 0.570	0.190

Notes.

[a] For the spectra that present non-gaussian shapes we fitted two Gaussians with the same width. For the rest of spectra we fitted a single Gaussian.

implies small missing flux due to the missing short spacings of the BIMA array.

6.2.2 MOPRA

The MOPRA observations were carried out in 2008 May. The weather conditions were excellent with system temperature ranging between 160-180 K. We used the MOPS spectrometer in Zoom Mode, which provides up to 16 spectral windows of 137.5 MHz of bandwidth, divided in 4096 channels of 34 KHz of width (~ 0.1 km s^{-1} at 3 mm). The spectra were taken at the IRS1 position, in position switching mode selecting an off-source position 600″ away to the north. At 3 mm the MOPRA beam is $\sim 35''$ and the main beam efficiency is ∼0.45 (Ladd et al. 2005). The data were reduced with the ASAP software and the resulting spectra were converted to CLASS format, and analyzed and displayed with the GILDAS software. The observed transitions and the results of the Gaussian fits to the reduced spectra are shown in Table 6.6: for the transitions without hyperfine structure the parameters are the

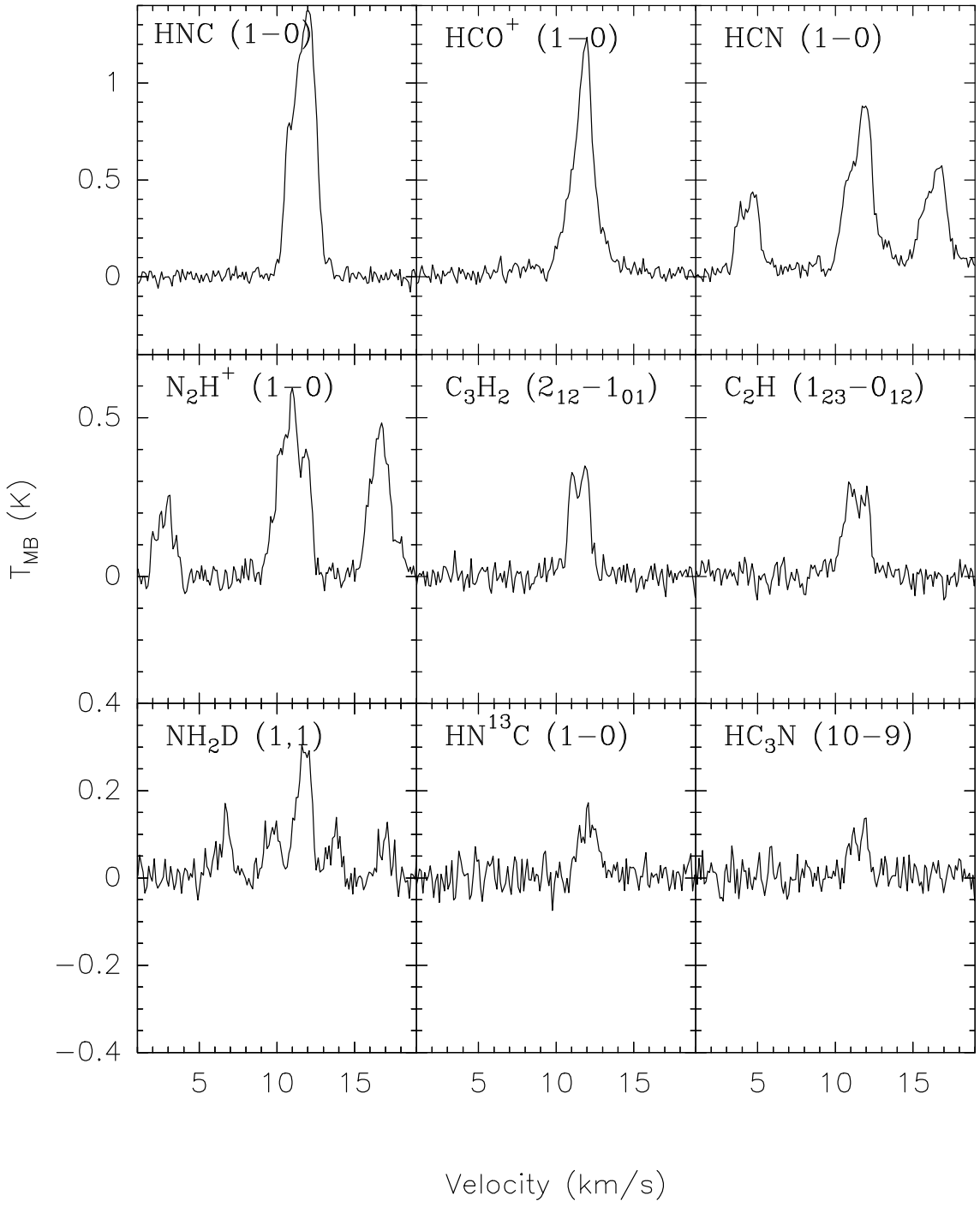

Figure 6.6: Spectra of the detected transitions of the species observed with the MOPRA telescope at the Center position in the HH 80N core.

Table 6.6: Parameters of the transition lines observed with MOPRA[a]

Transition	Frequency (GHz)	Area K km s^{-1}	$V_{\rm sys}$ km s^{-1}	Width km s^{-1}	Intensity K	Rms K
OCS (7–6)	85.139104	–	–	–	< 0.078	0.026
C_3H_2 ($2_{1,2}$–$1_{0,1}$)	85.338906	0.238 (0.010)	11.08 (0.02)	0.69 (0.02)	0.319	0.027
	.	0.256 (0.011)	11.90 (0.02)	fixed	0.351	
C_2S (6_7–5_6)	86.181413	–	–	–	< 0.078	0.026
$HN^{13}C$ (1–0)	87.090959	0.019 (0.016)	12.09 (0.06)	1.34 (0.13)	0.130	0.029
C_2H ($1_{2,3}$–$0_{1,2}$)	87.3169253	0.260 (0.013)	10.91 (0.03)	0.91 (0.03)	0.270	0.028
	.	0.230 (0.013)	11.91 (0.03)	fixed	0.239	
HC_5N (33–32)	87.863631	–	–	–	< 0.075	0.025
HCO^+ (1–0)	89.18852	0.360 (0.025)	10.75 (0.05)	1.21 (0.02)	0.278	0.030
	.	1.432 (0.032)	11.92 (0.01)	fixed	1.108	
HCOOH (4_{04}–3_{03})	89.57917	–	–	–	< 0.075	0.025
HC_2N (9–8)	89.419162	–	–	–	< 0.120	0.040
HNC (1–0)	90.663572	0.487 (0.022)	10.84 (0.03)	1.09 (0.02)	0.420	0.028
	.	0.950 (0.027)	11.96 (0.02)	fixed	0.820	
HC_3N (10–9)	90.978989	0.144 (0.015)	11.53 (0.07)	1.37 (0.15)	0.099	0.027
CH_2DOH (4_{13}–4_{04})	91.58697	–	–	–	< 0.072	0.024
^{13}CS (2–1)	92.494303	–	–	–	< 0.072	0.024
HDCS (3_{03}-2_{02})	92.981593	–	–	–	< 0.066	0.022
Hyperfine	.	$T_{MB} \times \tau$	Systemic velocity	Width		Rms
Transitions	.	K	km s^{-1}	km s^{-1}	τ_{main}	K
NH_2D (1,1)	85.926263	0.176 (0.013)	11.80 (0.02)	0.97 (0.04)	0.186	0.026
HCN (1–0)	88.63185	0.487 (0.022)	10.84 (0.03)	1.09 (0.02)	0.420	0.028
	.	0.950 (0.027)	11.96 (0.02)	fixed	0.280	
N_2H^+ (1–0)	93.17351	0.089 (0.005)	10.80 (0.01)	1.10 (0.03)	0.11(0.04)	0.028

Notes.

[a] For the spectra that present non-gaussian shapes we fitted two Gaussians with the same width. For the rest of spectra we fitted a single Gaussian.

same than those of Tables 6.2–6.5 with an additional column for the frequency; for the transitions with hyperfine structure the parameters are the same as above except for the third and sixth column, where we show the peak brightness temperature multiplied by opacity, and the opacity of the main hyperfine line, respectively.

9 transitions out of 17 (excluding hyperfine transitions) were detected, which are displayed in Fig. 6.6. Because the beam of MOPRA encompass a large part of the HH 80N core, the components discussed above appear blended in the spectra. The fit of a single Gaussian gives linewidths broader (> 1 km s^{-1}) than those of the IRAM 30m spectra. Below, the MOPRA data is used to derive global properties of the core. For NH_2D, the main beam brightness temperature measured with MOPRA is ~ 0.3 K, a factor of two higher than the brightness temperature of the spectrum taken at the same position in the NH_2D PdBI channel maps convolved to the MOPRA beam (~ 0.15 K). This gives $\sim$ 50% of missing flux due to the missing short spacings of the PdBI array.

6.3 Analysis

The detection of multiple transitions of CS and SO (and isotopologues) in some of the observed positions in the HH 80N core allows to constrain the physical properties of the emitting gas. We used the one-dimensional non-LTE RADEX radiative transfer model code (van der Tak et al. 2007) to find the set of molecular column densities (N), gas density (n) and gas temperature ($T_{\rm k}$) that best reproduce the intensity of the observed lines (see Tables 6.2–6.5). RADEX uses the escape probability formulation assuming an isothermal and homogeneous medium. In order to simulate the beam dilution effects we multiplied the intensities obtained with RADEX by the appropriate filling factor assuming that the size of the emission (θ) is the same for all the transitions and that the source emission profile has a Gaussian distribution. The true morphology of the source can be much more complex and, hence, the source size parameter must be understood as an effective angular size. As fixed parameters we adopted 2.73 K for the background temperature and the linewidth values reported in Tables 6.2–6.5 (typically between 0.5–1 km s^{-1}). We considered H_2 as the only collisional partner and adopted a sulphur isotope abundance ratio of 22.7 (Lucas and Liszt 1998).

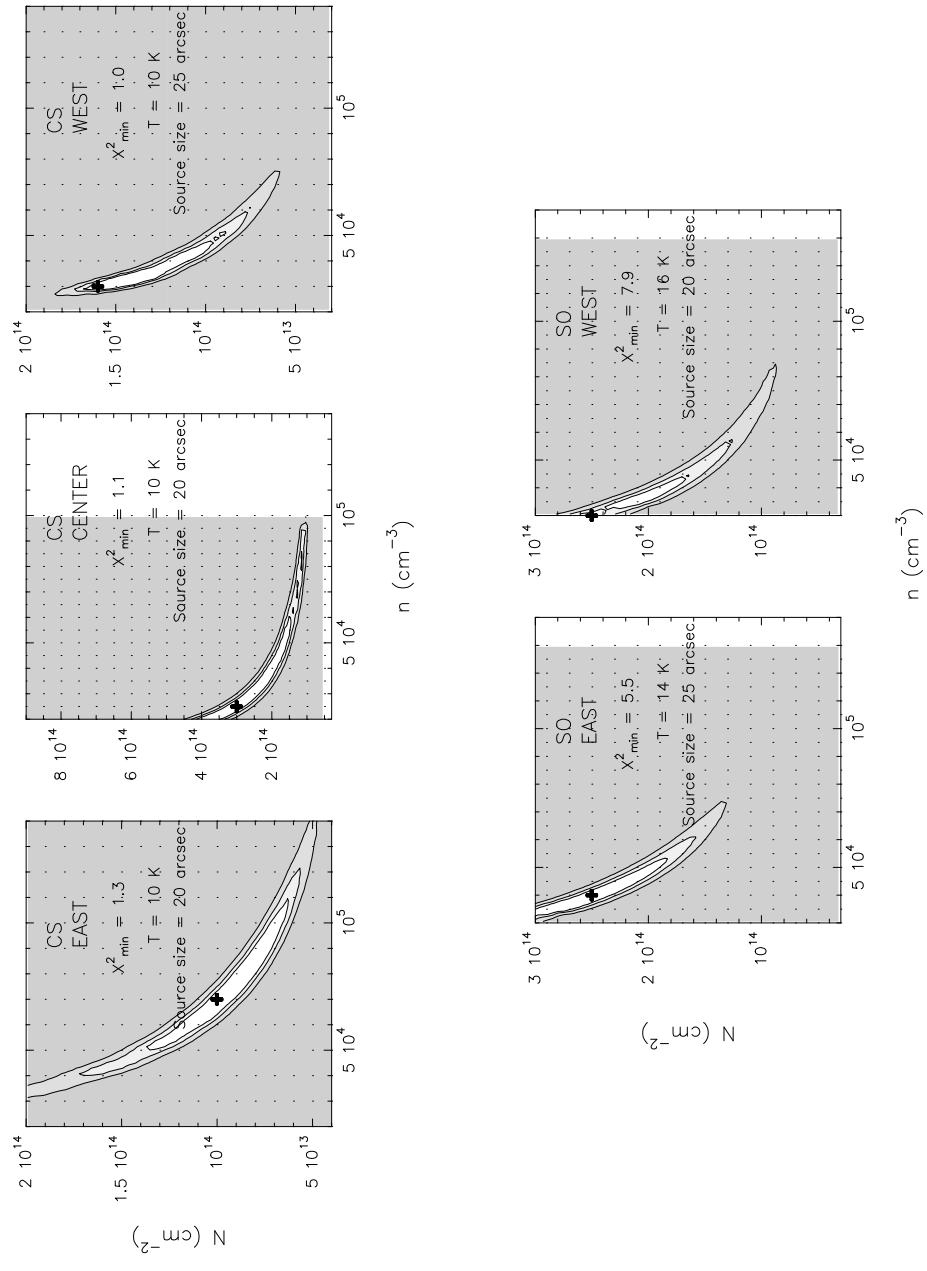

Figure 6.7: Contour plots (solid line and gray scale) of the χ^2 function derived from the RADEX analysis. The top panels show the results derived from the CS spectra observed at the East (left), Central (central) and West (right) positions. The bottom panels show the results derived from the SO spectra at the East (left) and West (right) positions. The cross marks the parameters that minimizes the χ^2 function in each panel. In all the cases the contour levels indicate the confidence limits corresponding to 99, 90 and 68% (1σ). These contours are relative to the minimum χ^2 value of each panel.

We determined the best fit model by means of χ^2-statistics resulting from comparing the measured and calculated line intensities. For each observed position we inspected the N(molecule)-n plane for different gas temperatures and source sizes within the 10 K $< T_{\rm k} <$ 20 K and $15'' < \theta < 100''$ ranges, respectively, for the SO and CS independently, because both molecules does not necessarily trace the same gas. In this analysis we excluded the NB position because the emission of the HH 80N core has a small contribution to the NB spectra. At the Center position we only run RADEX for the CS lines, because there is only one SO line observed.

Fig. 6.7 shows the plots of the best set of solutions of the χ^2 function. The large uncertainties of the RADEX analysis become evident in this figure. The uncertainty for the source size, θ, is $\pm 5''$, and for the temperature ± 2 K for CS and ± 4 K for SO. Considering these ranges, the n and N (X) determination is uncertain by about a factor of two in all the cases. The χ^2 analysis used for the SO did not included the SO $(2_3 - 1_2)$ because its contribution degrades the quality of the fit and moves the solutions for θ and n to higher values. The numerical results of Figure 6.7 are summarized in Table 6.7. In this table we also report the line peak intensity values predicted by RADEX taking in account the beam dilution. The calculated main beam intensity of SO $(2_3 - 1_2)$ is clearly above the observed while a low intensity for the non-detected ^{34}SO $(2_3 - 1_2)$ line is correctly predicted. A possible explanation could rely in the existence of several unresolved components overlapped in the sky with different physical conditions traced by different transitions.

In general, CS has better fit solutions than SO, as indicated by the lower $\chi^2_{\rm red}$ values obtained for CS. A possible explanation could be that the CS emission arises from gas with physical conditions rather homogeneous (one of the RADEX assumptions), while the conditions of the SO emitting gas are more complex. Note in Chapter 2 that the CS emission is much more homogeneous than the SO emission, which may be affected by other phenomena occurring in the region such as the UV radiation of HH 80N. In spite of small differences between the CS and SO results of Table 6.7, the physical properties of the gas estimated from the two independent probes are qualitatively similar ($n \leq 10^5$ cm^{-3} and $T_{\rm k} \leq 15$ K). Indeed, they trace cold and moderately dense gas that is able to excite low transitions of CS and SO. However, in regions far away from IRS1, the gas is not dense enough to be detected by the thermal dust emission given the sensitivity of our continuum observations, or with the absorption feature of the *Spitzer* 8 μm image. The derived small effective source size $(20'' - 25'')$ reflects the intrinsic clumpy structure of the HH 80N core. The possible CS and SO column density range derived with RADEX taking into

Table 6.7: Results of the RADEX analysis.

	CS				SO	
Position	East	Center	West		East	West
$n(10^4$ cm$^{-3})$	7	2.5	3		4	3
$T_{\rm K}$ (K)	10	10	10		14	16
$N(10^{14}$ cm$^{-2})$[a]	1	3	1.6		2.5	2.5
θ (arcsec)	20	20	25		25	20
$T_{\rm MB}^{\rm CS(2-1)}$ (K)	1.49	1.46	1.56	$T_{\rm MB}^{\rm SO(3_2-2_1)}$ (K)	1.82	1.34
$T_{\rm MB}^{\rm C^{34}S(2-1)}$ (K)	0.20	0.23	0.20	$T_{\rm MB}^{\rm ^{34}SO(3_2-2_1)}$ (K)	0.20	0.14
$T_{\rm MB}^{\rm CS(3-2)}$ (K)	1.21	1.16	1.02	$T_{\rm MB}^{\rm SO(2_3-1_2)}$ (K)[c]	0.47	0.35
$T_{\rm MB}^{\rm C^{34}S(3-2)}$ (K)	0.11	0.11	0.08	$T_{\rm MB}^{\rm ^{34}SO(2_3-1_2)}$ (K)[b]	0.02	0.02
$T_{\rm MB}^{\rm CS(5-4)}$ (K)[b]	0.09	0.08	0.05	$T_{\rm MB}^{\rm SO(3_4-2_3)}$ (K)	0.26	0.20
				$T_{\rm MB}^{\rm ^{34}SO(5_5-4_4)}$ (K)[b]	0.04	0.03
				$T_{\rm MB}^{\rm ^{34}SO(6_5-5_4)}$ (K)	0.23	0.19
χ^2_{red}	0.7	0.6	1.0		2.8	3.9

Notes.

[a] Bad constrained value. Column densities of CS at Center and SO at East are lower limits.

[b] This transition was undetected in the observations.

[c] This transition is not included in the χ^2 analysis (see text).

Table 6.8: CS and SO column densities derived from the uncertainty range of the RADEX analysis.

	Position					
	East		Center[b]		West	
Molecule	$N_{\rm m}$	$N_{\rm M}$	$N_{\rm m}$	$N_{\rm M}$	$N_{\rm m}$	$N_{\rm M}$
CS	2.3	7.8	≥ 7.5	–	3.0	7.8
SO	≥ 8.0	–	–	–	5.1	11.7

Notes.
[a] In units of 10^{13}.
[b] SO column densities at Center are shown in Table 6.9.

account θ and T variations (in addition to N(molecule) and$n$ variations shown in Fig. 6.7) are shown in Table 6.8.

For the molecules with only one transition observed, we fixed the values of n, $T_{\rm k}$ and θ and inspected N(X) values until the intensity peak of the main beam temperature of the observed line was reproduced in each position. In order to evaluate the uncertainties, we performed this process fixing the best fit values of CS and SO and the N(X) results obtained in both cases were taken as limits of a possible range of solutions. The resulting column densities for these species are shown in Table 6.9. In addition, we derived averaged H_2 column densities from the MAMBO continuum map convolved to the source size estimated above. At the MAMBO observing wavelength (1.2 mm) the continuum emission is optically thin and, hence, it is a good tracer for the mass along the line of sight. We followed Frau et al. (2010), assuming a dust opacity coefficient at 1.2 mm of 0.0066 cm^2 gr^{-1}, as the average value between dust grains with thin and thick ice mantles for a volume density of 10^5 cm^{-3} (Ossenkopf and Henning 1994), adequate given the cold and dense gas of the HH 80N core. For T we used 10 K and 15 K, and for the θ, $20''$ and $25''$ (i.e. the possible values according the RADEX results, see Table 6.7). The resulting H_2 column densities and the derived abundances are shown in Tables 6.10, 6.9 and 6.12, respectively. The column densities and abundances are multiplied by the filling factor corresponding to a beamsize of $25''$ (i.e. the beamsize of IRAM 30m at 3 mm). We did not follow this method for the H_2S line because the corresponding molecular data file was not available in the Leiden Atomic and Molecular Database (LAMBDA), which is used by RADEX to calculate the line intensities.

Table 6.9: Column densities obtained from the RADEX analysis For other species than CS i SO.[a]

		$n = 3 \times 10^4 \mathrm{cm}^{-3}$				$n = 7 \times 10^4 \mathrm{cm}^{-3}$			
		$T_\mathrm{K} = 10$ K		$T_\mathrm{K} = 15$ K		$T_\mathrm{K} = 10$ K		$T_\mathrm{K} = 15$ K	
Molecule	Position	$\theta = 20''$	$\theta = 25''$	$\theta = 20''$	$\theta = 25''$	$\theta = 20''$	$\theta = 25''$	$\theta = 20''$	$\theta = 25''$
SO_2	East	1.95	1.75	1.37	1.25	0.97	1.00	0.78	0.75
SO_2	West	2.92	3.25	1.95	2.00	1.75	1.76	1.17	1.25
DCO^+	East	1.37	1.50	0.58	0.75	0.58	0.50	0.23	0.25
DCO^+	West	0.14	0.17	0.06	0.08	0.06	0.08	0.03	0.04
N_2D^+	East	1.56	1.75	0.58	0.75	0.58	0.75	0.23	0.28
N_2D^+	West	1.37	1.50	0.58	0.50	0.58	0.50	0.19	0.25
SO[b]	Center	14.16	13.62	9.76	10.22	7.04	7.26	5.22	5.08

Notes.

[a] in units of 10^{13} cm^{-2}.

[b] Obtained from $N(^{34}\mathrm{SO})$ assuming a sulfur isotope abundance ratio, $^{32}\mathrm{S}/^{34}\mathrm{S}$, of 22.7 (Lucas & Liszt 1998).

Table 6.10: H_2 column densities derived from the 1.2 mm MAMBO map.[a]

	$T_K = 10$ K		$T_K = 15$ K	
Position	$\theta = 20''$	$\theta = 25''$	$\theta = 20''$	$\theta = 25''$
East	2.33	1.96	1.23	1.04
Center	5.22	3.72	2.76	1.96
West	0.82	0.80	0.43	0.42

Notes.
[a] In units of 10^{22} cm^{-2}.

Table 6.11: Molecular abundances derived from the uncertainty range of the column densities reported in Table 6.8 and the H_2 column densities of Table 6.10.[a]

	Position					
	East		Center[b]		West	
Molecule	χ_m	χ_M	χ_m	χ_M	χ_m	χ_M
CS	9.87	63.41	≥ 20.16	–	37.50	95.12
SO	≥ 40.82	–	–	–	118.60	272.09

Notes.
[a] In units of 10^{-10}.
[b] In this table, for the Center position we only report CS abundances. See Table 6.12 for the SO abundances obtained at the Center position.

Table 6.12: Fractional abundances relative to H_2 obtained with the column densities of Table 6.9 and Table 6.10.[a]

		$n = 3 \times 10^4 \mathrm{cm}^{-3}$				$n = 7 \times 10^4 \mathrm{cm}^{-3}$			
		$T_\mathrm{K} = 10$ K		$T_\mathrm{K} = 15$ K		$T_\mathrm{K} = 10$ K		$T_\mathrm{K} = 15$ K	
Molecule	Position	$\theta = 20''$	$\theta = 25''$	$\theta = 20''$	$\theta = 25''$	$\theta = 20''$	$\theta = 25''$	$\theta = 20''$	$\theta = 25''$
SO_2	East	8.37	8.93	11.10	12.02	4.18	5.10	6.34	7.21
SO_2	West	35.67	40.62	45.35	47.62	21.40	21.87	27.21	29.76
DCO^+	East	5.86	7.65	4.76	7.21	2.51	2.55	1.90	2.40
DCO^+	West	1.66	2.19	1.36	1.79	0.71	0.94	0.63	0.83
N_2D^+	East	6.70	8.93	4.76	7.21	2.51	3.83	1.90	2.64
N_2D^+	West	16.64	18.75	13.60	11.90	7.13	6.25	4.53	5.95
SO	Center	27.24	36.55	34.96	52.21	13.61	19.74	19.29	26.11

Notes.

[a] In units of 10^{-10}.

6.4 Discussion

According to chemical models (Bergin and Langer 1997; Taylor et al. 1998), some molecules (early type) are predicted to form early in the chemical evolution, while others (late type) require longer time to form. The most complex chemical models with a time-varying density predict, as a condensation contracts, significant depletion of some species (e.g. sulfur-bearing molecules) when the freeze out onto grain mantles is included in the models (Bergin and Langer 1997). Aikawa et al. (2005) followed the chemical evolution of a collapsing gas condensation for two types of dynamical evolution. The first model assumes a nearly hydrodynamical equilibrium (the initial ratio of gravity vs. pressure is α=1.1). In the second model (α=4.0) the condensation contracts dynamically. In the following we discuss briefly the chemistry of the HH 80N core by comparing our results with some of the chemical models mentioned above.

6.4.1 Global chemical properties of the HH 80N core

Among the lines detected with MOPRA and IRAM 30m there are either, early type (e.g CS, HCN, C_2H) and late type species (e.g. HCO^+, N_2H^+, NH_2D). The detection of late type molecules implies that some condensations of the HH 80N core must be evolved enough to process some chemical species, as can occur in IRS1. Moreover, the non-detection of the early type molecule C_2S, although we cannot discard to be caused by excitation effects, sets the lower possible age for the existence of dense gas in all the core to 10^5 yr, according to the lifetime of this molecule (de Gregorio-Monsalvo et al. 2006) in dense cores. These results are consistent with the HH 80N core being a relatively old core.

As already seen in the PdBI 3.5 mm continuum map, the HH 80N core has substructure that can not be resolved with the MOPRA and IRAM 30m beamsize. The chemistry of a cloud with an unresolved clumpy structure was modeled by Taylor et al. (1996, 1998) and observed in L673 (Morata et al. 2003, 2005). The authors concluded that the different spatial distribution of molecules could be a consequence of a clumpy nature for molecular clouds. Leaving aside photochemical and/or opacity effects, the observed rich chemistry in the HH 80N core could be consequence of the coexistence of condensations of different masses and densities,

some of them being quite evolved, which could yield different chemistry among them. Varied chemistry is also found in other clouds, and sometimes the chemical distribution can be very heterogeneous such as observed recently in the Pipe nebula (Frau et al. 2012)

6.4.2 Chemical differentiation in the HH 80N core

The results of Tables 6.8, 6.9, 6.11, 6.12 are summarized in Fig. 6.8. The CS and SO column densities are in agreement with those derived in Chapter 3 except for the Center position which are higher by a factor of > 2. The reason of this discrepancy could be the observation of less CS and SO transition lines at the Center position and, therefore, to have less constraints in the RADEX analysis with respect the rest of positions. The continuum emission maps (see Fig. 4.2) show that most of the material of the HH 80N core is concentrated at the IRS1 and eastern part of the HH 80N core, where higher H_2 column densities and a lower abundance trend of CS and SO with respect to the rest of the core are obtained.

Since molecular abundances can have strong variations in small regions along the line of sight, the direct comparison of the observed and modeled molecular abundances is not straightforward. In addition, deriving molecular abundances depends on a reliable H_2 column density estimation, which may be affected by temperature variations along the core. An easier comparison of observational data and models can be performed via molecular column densities. Molecular column densities are a direct observable that already includes density enhancement of the gas and molecular depletion. In the top panel of Fig. 6.8 we compare the column densities of Aikawa et al. (2005), who have presented one of the most realistic chemical model of core contraction. They derived column densities from the modeled abundance distribution of molecular species for the slow and rapid core contraction case in their chemical models. For a straightforward comparison with observations, they convolved the modeled molecular column densities to the angular resolution of the IRAM 30m telescope, which are displayed in their Table 2. Given the mass of the material of the HH 80N core not belonging to IRS1 (10 $M_\odot$), the resemblance of condensations in the HH 80N core with the modeled cores of Aikawa et al. (2005) (with 4 $M_\odot$ of mass) is likely and makes optimal the qualitative comparison of our results with the Aikawa et al. (2005) models.

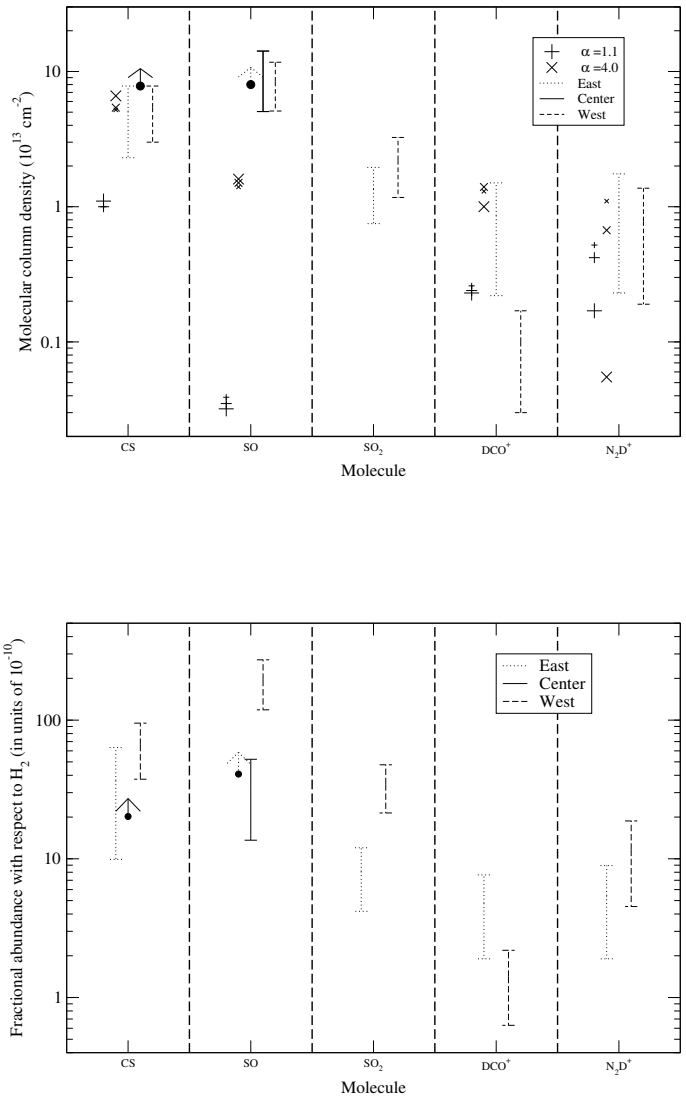

Figure 6.8: *Top panel*: Estimated ranges of molecular column densities of Tables 6.8 and 6.9 compared to the column densities derived from the theoretical models of Aikawa et al. (2005). Dotted lines correspond to the column density derived in the East position; solid lines,to the Center position; and dashed lines, to the West position. From big to small, right crosses correspond to the modeled column density when the core reaches a central density of 3×10^5 cm^{-3}, 3×10^6 cm^{-3} and 3×10^7 cm^{-3} with the model with $\alpha = 1.1$. Tilted crosses represent the same as right crosses but for the model with $\alpha = 4.0$. $\alpha = 1.1$ implies slow core collapse while $\alpha = 4.0$ implies rapid core collapse (see text). *Low panel:* Estimated ranges of possible molecular abundances with respect to H_2 of the species of Tables 6.11 and 6.12. Dotted lines correspond to the abundance derived in the East region; solid lines,to the Center position; and dashed lines, to the West position.

In general, Fig. 6.8 shows that column densities of the molecular species in the HH 80N core are quite high, some of them even above the predictions of the model with $\alpha = 4.0$, indicating that the HH 80N core achieved high densities very rapidly. The Center position has the largest column densities of CS. The presence of IRS1 indicates that the gas in this position is more evolved and reached high central gas densities and, hence, the CS depletion is expected to be more severe. However, the possible rapid contraction of IRS1 may yield abundances of CS high enough in layers surrounding the densest part of the condensation to contribute to a high total CS column density towards the Center position. At the East position , SO and DCO^+ column densities tend to be highest, although we cannot discard a molecular enhancement due to the UV chemistry for these species. Modeled SO_2 column densities are not reported in the Table 2 of Aikawa et al. (2005). Our observed SO_2 column densities are similar or higher to the column densities observed in other regions even though this comparison involve observations with different instruments (e.g. 2×10^{13} cm^{-2} in L134N, Sweitzer 1978). N_2D^+ results do not contribute to clarify any specific trend.

Chapter 7

General discussion and conclusions

7.1 The role of the HH 80/81/80N outflow

7.1.1 Radiative perturbation by HH 80N

The nature of the molecular condensations ahead of HH objects studied up to date is well known (Girart et al. 2001, 2005; Viti et al. 2003, 2006; Whyatt et al. 2010). These clumps are believed to be transient dense structures inherent to molecular clouds with enhanced abundances of some molecular species (e.g. CH_3OH, HCO^+, SO, Viti and Williams 1999a; Viti et al. 2003) due to the presence of UV radiation coming from the HH object. Otherwise, these clumps would remain undetected when observed with lines of these species because they are quiescent and not long-lived enough to drive complex chemistry. Given that only a fraction of these clumps are massive enough to collapse and form stars, the association between the star forming core HH 80N next to an HH object is rare and makes the HH 80N region unique. While the study of the chemistry observed near HH objects typically involves small transient clumps, in Chapter 3 we study the photochemical effects caused by the UV irradiation of an HH object in a nearby condensation of gas (the HH 80N core) large enough to fragment and give birth to one or more protostars (IRS1).

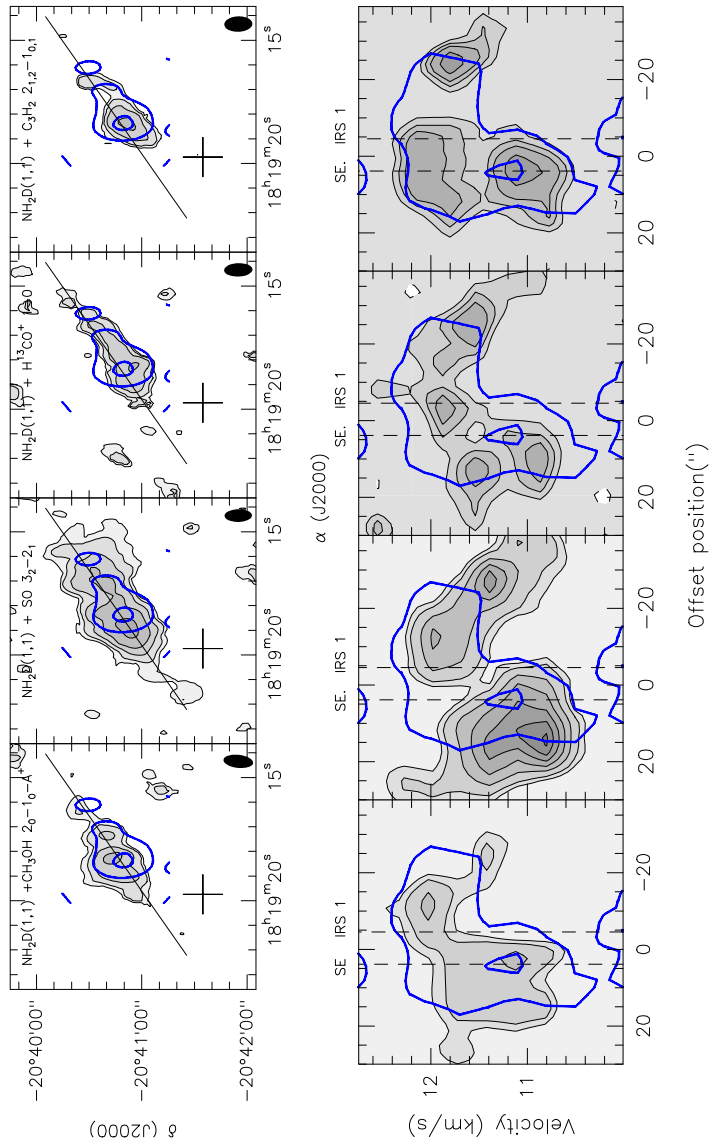

Figure 7.1: *Top panels:* Superposition of the integrated emission of the NH_2D (1,1) (blue contours) with the integrated emission of the (gray scale, from left to right) CH_3OH ($2_0 - 1_0$−A), SO ($3_2 - 2_1$), $H^{13}CO^+$ (1–0) and C_3H_2 ($2_{1,2} - 1_{0,1}$). The beam is shown in the bottom right corner of the top panels panels. The solid line marks the cut (A direction) of the PV plots shown in bottom panels *Bottom panels:* Superposition of the PV plots of NH_2D (1,1) (blue contours) with (gray scale, from left to right) CH_3OH ($2_0 - 1_0$−A), SO ($3_2 - 2_1$), $H^{13}CO^+$ (1–0) and C_3H_2 ($2_{1,2} - 1_{0,1}$) obtained from a cut along direction A. The positive offsets corresponds to the southeast direction. The position offsets of IRS1 and SE are marked with dashed lines. NH_2D data were smoothed to the angular resolution of BIMA observing at 3 mm.

We find high abundances of CH_3OH and SO in a region of the core facing HH 80N and, hence, more exposed to the UV radiation field. However, the chemistry of a large fraction of the core is not affected by UV irradiation. In fact, inside the clump, the observed chemistry is typical of starless cores, which have high abundances of dense gas tracers such as NH_3 and NH_2D. As seen in Figure 7.1, CH_3OH and SO have emission eastwards the NH_2D contours and SO has a peak 10″ southeast of SE. The linewidth at this position, close to HH 80N, show a clear broadening, but it is not large enough to trace a direct shock of the HH 80/81/80N outflow (with speed velocities of few hundreds of km/s) with the dense core. This means that in the condensations massive enough, such as the HH 80N core, the high densities achieved in the clump prevent the UV photons to penetrate inside. Therefore, the photochemical effects happen on the 'surface' of the clump. This effect was previously observed in HH 2 (Girart et al. 2005).

7.1.2 Collision of a low-density layer

The bow-shock of the HH 80/81/80N outflow goes past the vicinity of the HH 80N core without a direct impact as indicated by the lack of shock signatures: the high density tracers show velocity gradients of $\simeq 1.0$ km s^{-1}, whereas the flow velocity of the outflow is several hundreds of km s^{-1}; also, the molecular lines do not show high velocity wings (see Fig. 7.3). In addition, the SiO emission, an excellent tracer of strong shocks within molecular gas, is absent in the HH 80N core (see Chapter 3). Nevertheless, it is known that a connection between outflows and large scale motions exists in the molecular clouds (Reipurth et al. 1997), so it is still possible that the HH 80/81/80N outflow is having some influence in the peculiar kinematics of the molecular core.

The molecular gas associated with the SE dusty clump is shifted in velocity by ~ 1.0 km s^{-1} with respect the gas component associated with the IRS 1 protostar. We adopt the velocity of this component, $\simeq 12.0$ km s^{-1}, as the original velocity the HH 80N core. In Chapter 4 we estimated that the mass of material outside the IRS1 core is $\sim 10\ M_\odot$. Since the SE clump is the most massive structure outside IRS1, we adopt this value for the SE mass. In this case, the velocity shift of this clump implies a kinetic energy of $\sim 3 \times 10^{44}$ ergs. We can crudely estimate the timescale needed to provide this kinetic energy through momentum injection by the HH 80N shock. First, we assume that the energy dissipation in the HH 80N

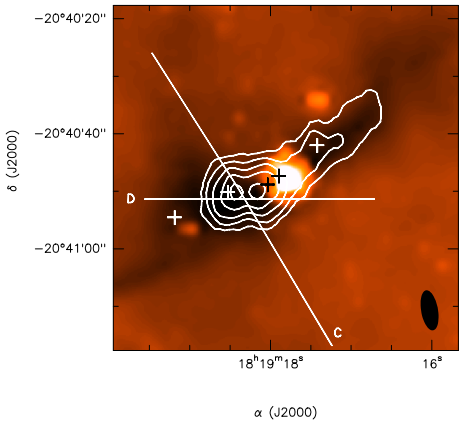

Figure 7.2: Superposition of the Spitzer 8 μm image (color scale) and the zero-order moment (integrated emission; white contours) over the 9.5-14.1 km s^{-1}velocity range of NH_2D (1,1). The contour levels are 3, 7, 12, 18, and 25 times 10 mJy beam^{-1} kms^{-1}. The solid lines show the cuts for the PV plots of Fig. 7.4. The crosses mark the positions where the spectra were taken. The beam is shown in the bottom right corner.

shock through momentum injection to the cloud ambient is of the same order as the radiative cooling. Molinari et al (2001) measured the spectral energy distribution in the far-IR of HH 80, HH 81 and HH 80N. HH 80N is brighter than HH 80 and 81 by a factor 2, but its flux is contaminated by the emission of the HH 80N core, so its far-IR luminosity is probably similar to the HH 80 and 81 luminosity. Therefore, we estimate a few tens of solar luminosities for HH 80N (i.e. $\sim 10^{34}$ erg s^{-1}). However, only a fraction of the energy released by HH80N arrives to the molecular core: the projected distance between the HH object and the core is 0.3 pc (see Chapter 1), so the solid angle subtended at the HH object by the molecular core is such that the dilution factor is $\sim 5\%$. Therefore, the HH 80/81/80N outflow transfers the energy required to drive the gas motions observed in the HH 80N core in $\sim 5 \times 10^4$ yr, a period of time compatible with the dynamical age of the outflow (10^5 yr, Yamashita et al. 1989).

A possible way to transfer part of the energy dissipated is through the generation of magneto-hydrodynamic waves that can produce density enhancements (Falle and Hartquist 2002; De Colle and Raga 2005; van Loo et al. 2006, 2007). These waves would travel away from the HH object and, thus, would interact with the HH 80N molecular core. In this scenario, the HH 80N core would have initially a systemic velocity of ~ 12.0 km s^{-1}. Then as the jet passes nearby, it would create

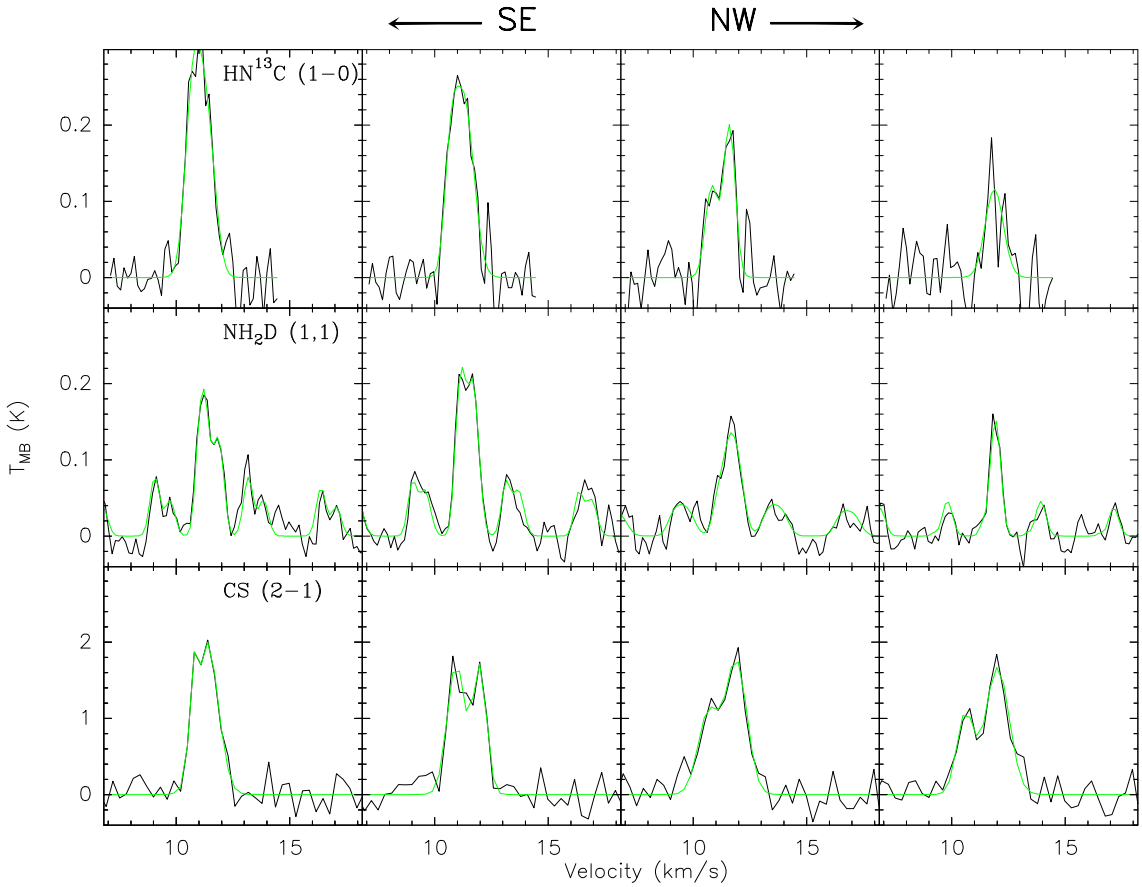

Figure 7.3: $HN^{13}C$ (1–0) (top panels), NH_2D (1,1) (middle panels) and CS (2–1)(bottom panels) spectra (black line) taken in the positions shown in Fig. 7.2. The CS spectra taken at the most eastward position is not shown in the figure. The green line indicates the best result of the fit of two Gaussian to the spectra.

a blue-shifted layer composed of gas swept by the HH 80/81/80N outflow, and with a density too low to be detected with the high density tracers used in this thesis. This layer would collide with the core generating the kinematic perturbation seen in the SE clump. Duarte-Cabral et al. (2011) modeled the collision of two filamentary clouds in order to reproduce the column density distribution and velocity field observed in Serpens by means of smoothed particle hydrodynamic simulations. One of the results of their simulations is the presence of several velocity components at the interface region of the collision. These components can show sharp or smooth velocity gradients, depending on the initial position of the clouds (i.e. whether they collide head-on or with their centers of gravity offset) and their degree of turbulence.

The HH 80N region, despite not sharing the exact geometry of the Serpens region, can be studied by means of a qualitative comparison with the results of Duarte-Cabral et al. (2011). To do this, we first obtained NH_2D maps with uniform weighting, which provide the best angular resolution possible. Then, we obtained PV plots along the major and minor axis of the core (A and B cuts, respectively), as well two additional cuts along the directions C and D, which are shown in Figure 7.2. The C cut is parallel to the minor axis but centered in the SE clump. The D cut is complementary and traces a direction halfway between the A and C cuts. The resulting PV plots for the four cuts are shown in Figure 7.4. The inspection of these cuts provides a complete kinematic picture of the HH 80N core, particularly in the eastern region where the NH_2D emission is concentrated. The improved angular resolution of the uniform weighed maps allows us to separate the emission arising from the SE and the IRS1 cores as different velocity components (see cut A Figure 7.4).

In Figure 7.5 we show synthetic PV plots resulting from the hydrodynamical simulations of Duarte-Cabral et al. (2011). Note that the complex features of these PV plots, in particular for the left panel of the figure. Interestingly the velocity distribution of this panel mimics fairly well the velocity structure seen in the NH_2D PV plot for the D cut (Fig. 7.4), although the velocity variations are a factor of 2 lower in the HH 80N core. This cut is along the SE core, suggesting that this condensation is found in the collision interface region. In addition, the appearance of PV plots along the directions B and C, showing at least two velocities at the same offset, is compatible with a head-on collision.

Apart from the velocity field, Duarte-Cabral et al. (2011) also make predictions of

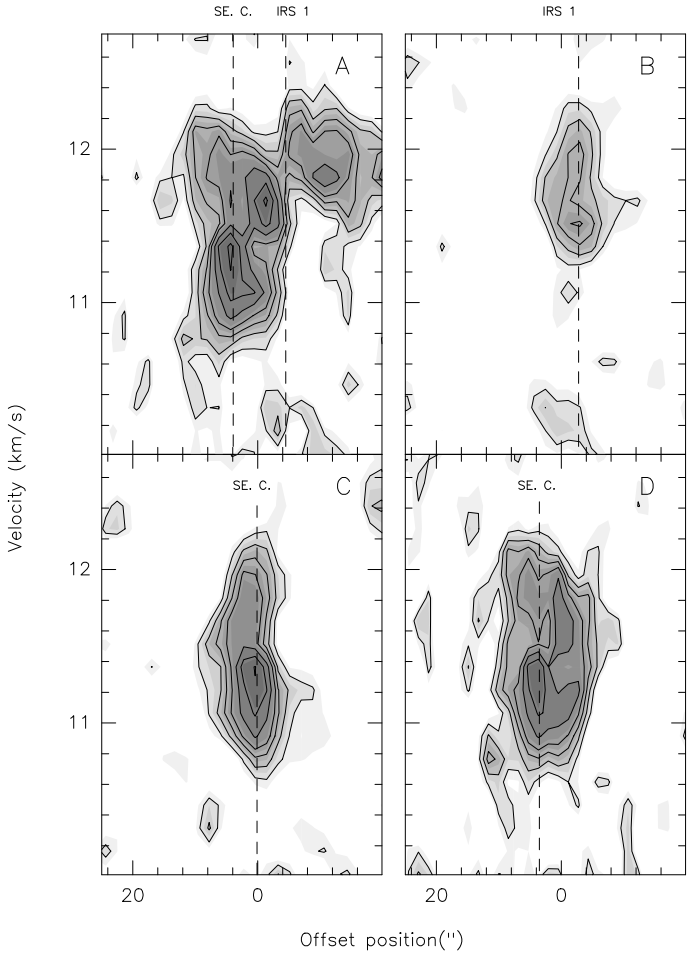

Figure 7.4: PV plots of the NH_2D (1,1) emission of the A (top left panel), B (top right panel), C (bottom left panel) and D (bottom right panel) directions. The positive offsets of the PV plots correspond to the southeast direction for the A cut, northeast for the B and C cuts, and east for D cut. The position offsets of IRS1 and SE are marked with dashed lines.

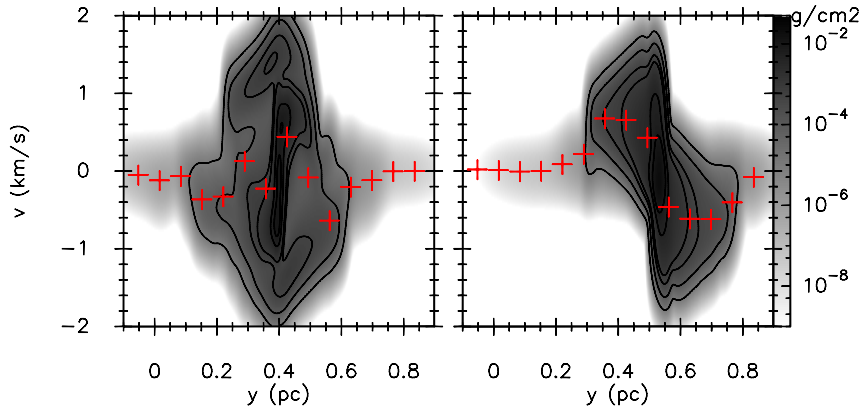

Figure 7.5: (From Duarte-Cabral et al. (2011)). PV plots (color scale and contours) obtained from a cut along the interface region of the synthetic map resulting from the simulation of a collision between two gas cylinders. The simulations were run without a turbulent velocity field for the gas in the cylinders. The left panel shows the results of the run corresponding to a direct collision between cylinders and right panel shows the results of an offset collision run.

the column density and mass distribution of the structure resulting from the collision of two clouds. Qualitatively, they found that a significant fraction of material is concentrated where the collision takes place generating instabilities and driving the formation of new stars. Remarkably, this perturbation can generate substructure inside the core, for example, via turbulent fragmentation (Ballesteros-Paredes and Mac Low 2002; Padoan and Nordlund 2002; van Loo et al. 2006, 2007). The location of IRS1 and SE in the presumed interacting region between the HH 80N core and the low density layer is in agreement with the collision scenario.

7.1.3 Triggered star formation

The collision could induce possible local instabilities in the HH 80N core that would trigger a star–formation episode in the HH 80N region, such as presumably happened in Serpens (Graves et al. 2010; Duarte-Cabral et al. 2010, 2011). If a significant amount of swept gas remains bound, dense condensations can be generated inside the core. Some of these condensations could be massive enough to induce gravity to overcome the internal pressure of the condensation, and thus, collapse. Given the velocity of the SE core with respect to the IRS 1 core ($\simeq 1.0$ km s^{-1}) and assuming

that the low density layer, as passes through the core, travels a distance of ∼0.05 pc (the approximate FHWM size for IRS1 and SE measured from the 3.5 mm PdBI contour map), we derive an interaction time of $\sim 5 \times 10^4$ yr. This period of time is similar to the time needed by the outflow to transfer the energy required to feed the gas motions observed in the HH 80N core, and significantly larger than the derived age for IRS1 ($\sim 2 \times 10^4$ yr, see Chapter 4). Therefore, a collapse induced by the collision event is feasible. Similar as IRS1, SE could be the result of the perturbation and could collapse in the future. For an 1 km s^{-1} linewidth, we derive a virial mass of $\sim 5\ M_{\odot}$, which is half the mass of the material of the HH 80N core not belonging to IRS1 (10 $M_{\odot}$, see Chapter 4).

The study of star formation induced by an external agent has been tackled with many approaches. Some works based on statistical arguments (Healy et al. 2004) employ surveys and large sets of objects. Other studies are based on theoretical work, either analytical (Leão et al. 2009) or through simulations (Hennebelle et al. 2003; Duarte-Cabral et al. 2011). On the other hand, some authors focus the attention on measurable observables such as the spatial distribution of molecular gas and dust in the region, the kinematics of the gas surrounding externally perturbed cores or interaction timescales (Wilking et al. 1984; Redman et al. 2003; Goicoechea et al. 2008).

Similar diagnostics of triggered star formation as those discussed for the HH 80N core were found in L1551 (Yokogawa et al. 2003). From the spatial distribution and velocity structure of the high density molecular tracers observed in L1551, Yokogawa et al. (2003) suggested that the dense gas in the region was being swept. In addition, the timescale of the outflow interaction is comparable to the lifetime of the object embedded within their studied core in L1551. In this thesis we additionally show that, regardless the possibility that IRS1 was triggered by the HH 80/81/80N outflow, the later is not capable of modifying the course of protostellar collapse from the standard case, as shown in Chapter 4.

7.2 Summary of the scenario of the HH 80N region

This work is a follow up study of Girart et al. (2001), which started with the analysis of BIMA molecular line dataset assuming that the molecular emission arises from a ring–like structure perpendicular to the plane of the sky, as interpreted previously

by (Girart et al. 2001). In this scenario, the ring, which is not a real structure but a result of a strong central depletion, is contracting with supersonic infall velocities (0.6 km s^{-1}) toward a central embedded object, IRS1. This morphology is clearly seen in CS, for which we derived an inner an outer radius of the ring of 2.5×10^4 AU and 6×10^4 AU, respectively, but not for the rest of species, which show strong molecular differentiation among them along the ring structure. This chemical differentiation may be partially caused by the UV photons coming from HH 80N that impinge on the part of the HH 80N core facing the HH object. This implies that the HH 80N core must be spatially close to HH 80N, not only in projection in the sky and, therefore, in the vicinity of the HH 80/81/80N outflow.

In order to shed light on a possible perturbation of the dynamical evolution of the HH 80N core by the HH 80/81/80N outflow, in Chapter 4 we modeled the continuum emission of the HH 80N IRS1 core using standard models of protostellar collapse. We found that a slowly rotating collapsing envelope of radius 0.08 pc and 20 $M_\odot$ plus a circumstellar disk of radius 300 AU and 0.6 $M_\odot$ fits fairly well the thermal dust emission of the IRS1 core. In addition, it predicts a static envelope beyond 1.5×10^4 AU from the embedded object, inconsistent with the supersonic infall velocities found using molecular species observed with BIMA. Since the thermal dust emission provides information on the mass distribution of the HH 80N core but not on the velocity field, the molecular dense envelope around IRS1 may not be necessarily static. However, to be consistent with our continuum modeling, the supersonic motions mentioned above can not be gravitationally bound. Besides, the PdBI and APEX continuum maps reveal that the HH 80N core is fragmenting into several condensations, being IRS1 one of them. This is in agreement with having infall motions within a region of 1.5×10^4 AU of radius from IRS1, with the kinematics and structure of the rest of the envelope decoupled from that of the IRS1 embedded object.

The interferometric observations of N-bearing species allow us to trace the densest part of the HH 80N core, where strong depletion affects the line emission of other molecules. This is because nitrogen bearing molecules do not deplete until the gas reaches densities up to 10^5–10^6 cm^{-3}. We find that the radial velocities of the gas traced with N-bearing molecules are smaller than those traced by CS at the position of IRS1, contrary to what could be expected if the envelope of HH 80N core traced by CS was infalling onto IRS1. Furthermore, the morphology of PV plots of the lines of N-bearing molecules differ from the expected for a contracting

ring morphology. Alternatively, the PV plots appearance could be explained with a collision event between a low density layer, maybe generated via MHD waves by the outflow, and the HH 80N core. The collision could generate local instabilities giving birth to new protostars.

In Figure 7.6 we outline a possible scenario proposed for the HH 80N region. As seen in the figure, the HH 80N core is composed of two velocity components, one, associated with the SE condensation, interacting with MHD waves fed by the outflow, and the other apparently not perturbed, associated with IRS1. The fact that the interacting part of the HH 80N core and the northern head of the HH 80/81/80N outflow are both blue-shifted is consistent with the possibility that the gas of the core is pushed as a result of the outflow passage. We cannot discern whether the IRS1 condensation preserves the original velocity of the HH 80N core because it is not disturbed or because it is too massive to be swept by the MHD waves. Apart form the HH 80N core, there is the Red Shifted Eastern structure (RSE) that is connected with the core at the far east of the SE condensation. The velocity gradient of the RSE towards SE suggests that this structure had an original velocity similar to the IRS1 condensation ($\sim$ 12.0 km s^{-1}) and then was partially swept by the MHD waves. However, given its distinctive properties (e.g. moderate gas density), we cannot rule out the possibility that the spatial connection between RSE and the HH 80N core is due to a projection effect.

The wide molecular survey presented in this thesis show how different molecular species trace different parts of the core. An excellent example is illustrated by NH_2D and CS. Deuterated ammonia traces the dense gas of the HH 80N core including the two velocity components associated to the IRS1 and SE condensations. On the other hand, CS is the most extended tracer and its emission possibly includes gas of the HH 80N core with moderate density tracing also the medium between condensations. The combination of the velocity gradients of the HH 80N core with the kinematics of this moderately dense gas may lead to interpret the CS PV plots appearance as a ring-like structure with radial motions.

7.3 Open questions and future aims

In this section, we suggest several points to further investigate star formation triggered by an external agent.

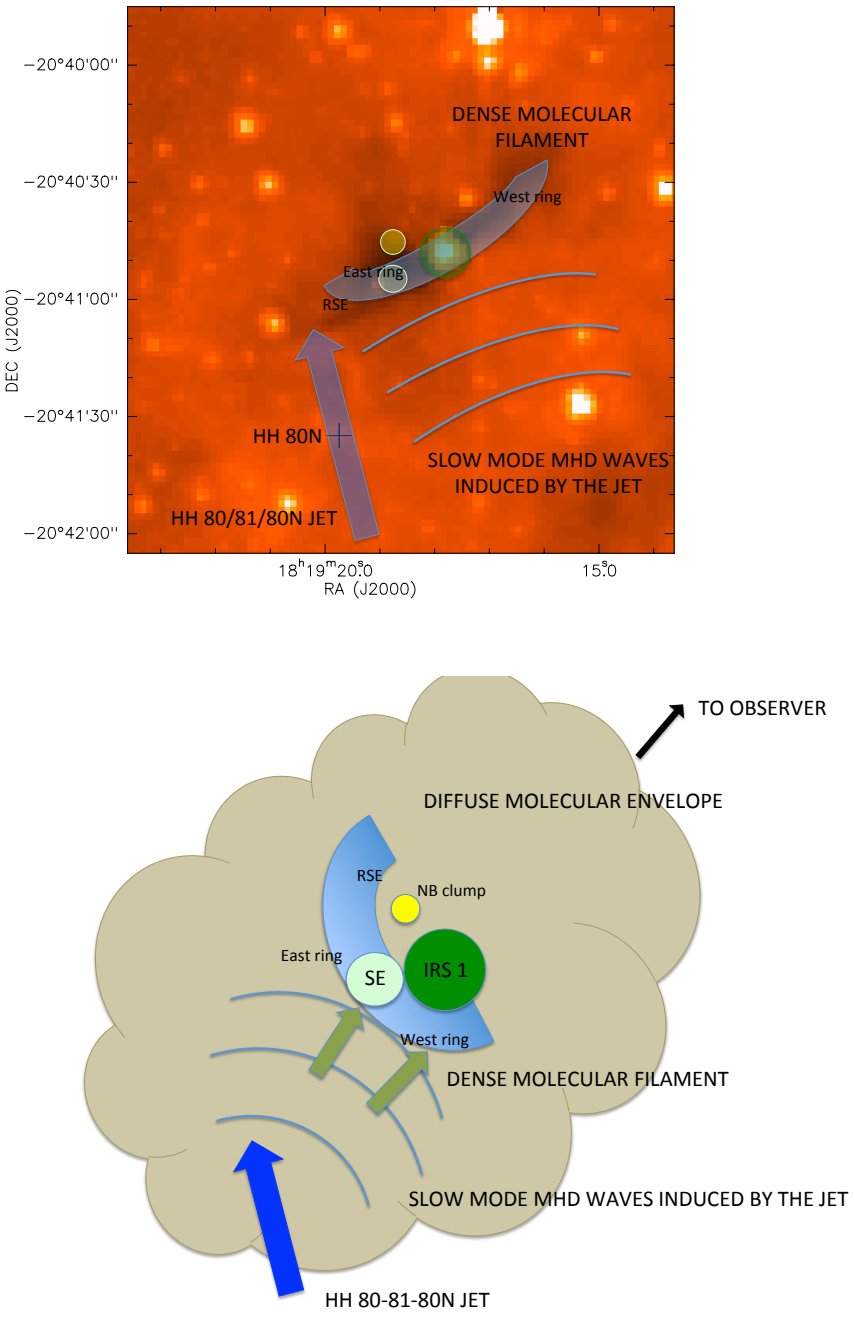

Figure 7.6: Schematic representation of the proposed scenario for the HH 80N region in order to account for the kinematic properties derived from the variety of molecular lines observed in the region.

1. To include hydrodynamic simulations in our analysis in order to provide additional evidence of collision between the HH 80N core and a low density layer. Although the timescale of the interaction is comparable to the age of IRS1 and that there is similarity between the PV plots of the HH 80N region and those resulting from hydrodynamic simulations, the approach presented in this chapter is purely qualitative. Hydrodynamic simulations taking into account the particular geometrical configuration of the HH 80N region are paramount to definitely confirm that the formation of IRS1 was caused by a collision event.

2. To apply the methodology developed in this work to other star forming regions with different local conditions. Apart from outflow influence, star forming regions can be perturbed by other agents such as supernova expanding shells, HII regions, stellar winds, etc. Expanding the analyzed dataset to star forming regions found in a variety of situations can help in determining the role of the environmental effects in the star formation process. This can shed light on the question whether the isolated star formation is the general rule or, otherwise, most of the observed stars are the feedback result of other stellar processes.

Bibliography

Adams, F. C. and Shu, F. H. (1985). Infrared emission from protostars. *The Astrophysical Journal*, 296:655–669.

Aikawa, Y., Herbst, E., Roberts, H., and Caselli, P. (2005). Molecular Evolution in Collapsing Prestellar Cores. III. Contraction of a Bonnor-Ebert Sphere. *The Astrophysical Journal*, 620:330–346.

Aikawa, Y., Ohashi, N., and Herbst, E. (2003). Molecular Evolution in Collapsing Prestellar Cores. II. The Effect of Grain-Surface Reactions. *The Astrophysical Journal*, 593:906–924.

Aikawa, Y., Ohashi, N., Inutsuka, S., Herbst, E., and Takakuwa, S. (2001). Molecular Evolution in Collapsing Prestellar Cores. *The Astrophysical Journal*, 552:639–653.

Allen, M. and Robinson, G. W. (1977). The molecular composition of dense interstellar clouds. *The Astrophysical Journal*, 212:396–415.

Andre, P. and Montmerle, T. (1994). From T Tauri stars to protostars: Circumstellar material and young stellar objects in the rho Ophiuchi cloud. *The Astrophysical Journal*, 420:837–862.

Andre, P., Ward-Thompson, D., and Barsony, M. (1993). Submillimeter continuum observations of Rho Ophiuchi A - The candidate protostar VLA 1623 and prestellar clumps. *The Astrophysical Journal*, 406:122–141.

Anglada, G. (1996). Radio Jets in Young Stellar Objects. In A. R. Taylor & J. M. Paredes, editor, *Radio Emission from the Stars and the Sun*, volume 93 of *Astronomical Society of the Pacific Conference Series*, pages 3–7.

Bachiller, R., Liechti, S., Walmsley, C. M., and Colomer, F. (1995). Methanol enhancemant in young bipolar outflows. *Astronomy and Astrophysics*, 295:L51+.

Bacmann, A., Lefloch, B., Ceccarelli, C., Steinacker, J., Castets, A., and Loinard, L. (2003). CO Depletion and Deuterium Fractionation in Prestellar Cores. *The Astrophysical Journal, Letters*, 585:L55–L58.

Ballesteros-Paredes, J. and Mac Low, M.-M. (2002). Physical versus Observational Properties of Clouds in Turbulent Molecular Cloud Models. *The Astrophysical Journal*, 570:734–748.

Bally, J. and Devine, D. (1994). A parsec-scale 'superjet' and quasi-periodic structure in the HH 34 outflow? *The Astrophysical Journal, Letters*, 428:L65–L68.

Bally, J., Devine, D., and Alten, V. (1996). A Parsec-Scale Herbig-Haro Jet in Barnard 5. *The Astrophysical Journal*, 473:921–+.

Basu, S. and Mouschovias, T. C. (1994). Magnetic braking, ambipolar diffusion, and the formation of cloud cores and protostars. 1: Axisymmetric solutions. *The Astrophysical Journal*, 432:720–741.

Bates, D. R. and Spitzer, Jr., L. (1951). The Density of Molecules in Interstellar Space. *The Astrophysical Journal*, 113:441–+.

Beckwith, S. V. W. and Sargent, A. I. (1991). Particle emissivity in circumstellar disks. *The Astrophysical Journal*, 381:250–258.

Belloche, A., André, P., Despois, D., and Blinder, S. (2002). Molecular line study of the very young protostar IRAM 04191 in Taurus: infall, rotation, and outflow. *Astronomy and Astrophysics*, 393:927–947.

Belloche, A., Hennebelle, P., and André, P. (2006). Strongly induced collapse in the Class 0 protostar NGC 1333 IRAS 4A. *Astronomy and Astrophysics*, 453:145–154.

Benson, P. J. and Myers, P. C. (1989). A survey for dense cores in dark clouds. *The Astrophysical Journal Supplement Series*, 71:89–108.

Bergin, E. A. and Langer, W. D. (1997). Chemical Evolution in Preprotostellar and Protostellar Cores. *The Astrophysical Journal*, 486:316–+.

Bergin, E. A., Langer, W. D., and Goldsmith, P. F. (1995). Gas-phase chemistry in dense interstellar clouds including grain surface molecular depletion and desorption. *The Astrophysical Journal*, 441:222–243.

Blake, G. A., Sandell, G., van Dishoeck, E. F., Groesbeck, T. D., Mundy, L. G., and Aspin, C. (1995). A molecular line study of NGC 1333/IRAS 4. *The Astrophysical Journal*, 441:689–701.

Bontemps, S., Andre, P., Terebey, S., and Cabrit, S. (1996). Evolution of outflow activity around low-mass embedded young stellar objects. *Astronomy and Astrophysics*, 311:858–872.

Bottinelli, S., Ceccarelli, C., Williams, J. P., and Lefloch, B. (2007). Hot corinos in NGC 1333-IRAS4B and IRAS2A. *Astronomy and Astrophysics*, 463:601–610.

Busquet, G., Palau, A., Estalella, R., Girart, J. M., Anglada, G., and Sepúlveda, I. (2009). Low-mass protostars and dense cores in different evolutionary stages in IRAS 00213+6530. *Astronomy and Astrophysics*, 506:1183–1198.

Busquet, G., Palau, A., Estalella, R., Girart, J. M., Sánchez-Monge, Á., Viti, S., Ho, P. T. P., and Zhang, Q. (2010). The NH_2D/NH_3 ratio toward pre-protostellar cores around the UC H II region in IRAS 20293+3952. *Astronomy and Astrophysics*, 517:L6+.

Calvet, N., Hartmann, L., Kenyon, S. J., and Whitney, B. A. (1994). Flat spectrum T Tauri stars: The case for infall. *The Astrophysical Journal*, 434:330–340.

Carey, S. J., Clark, F. O., Egan, M. P., Price, S. D., Shipman, R. F., and Kuchar, T. A. (1998). The Physical Properties of the Midcourse Space Experiment Galactic Infrared-dark Clouds. *The Astrophysical Journal*, 508:721–728.

Carrasco-González, C., Rodríguez, L. F., Anglada, G., Martí, J., Torrelles, J. M., and Osorio, M. (2010). A Magnetized Jet from a Massive Protostar. *Science*, 330:1209–.

Caselli, P., Walmsley, C. M., Zucconi, A., Tafalla, M., Dore, L., and Myers, P. C. (2002). Molecular Ions in L1544. II. The Ionization Degree. *The Astrophysical Journal*, 565:344–358.

Cassen, P. and Moosman, A. (1981). On the formation of protostellar disks. *Icarus*, 48:353–376.

Ceccarelli, C., Castets, A., Caux, E., Hollenbach, D., Loinard, L., Molinari, S., and Tielens, A. G. G. M. (2000). The structure of the collapsing envelope around the low-mass protostar IRAS 16293-2422. *Astronomy and Astrophysics*, 355:1129–1137.

Ceccarelli, C., Hollenbach, D. J., and Tielens, A. G. G. M. (1996). Far-Infrared Line Emission from Collapsing Protostellar Envelopes. *The Astrophysical Journal*, 471:400–+.

Chauhan, N., Pandey, A. K., Ogura, K., Jose, J., Ojha, D. K., Samal, M. R., and Mito, H. (2011). Star formation in bright-rimmed clouds and clusters associated with the W5 E H II region. *Monthly Notices of the Royal Astronomical Society*, 415:1202–1219.

Crapsi, A., Caselli, P., Walmsley, C. M., Myers, P. C., Tafalla, M., Lee, C. W., and Bourke, T. L. (2005). Probing the Evolutionary Status of Starless Cores through N_2H^+ and N_2D^+ Observations. *The Astrophysical Journal*, 619:379–406.

D'Alessio, P. (1996). *Accretion Disks around Young Stars*. PhD thesis, Instituto de Astronomía, UNAM, Apartado Postal 70-264, Ciudad Univesitaria, CP. 04510, México 20, D. F., México EMAIL: dalessio@astroscu.unam.mx.

D'Alessio, P., Merín, B., Calvet, N., Hartmann, L., and Montesinos, B. (2005). WWW Database of Models of Accretion Disks Irradiated by the Central Star. *Revista Mexicana de Astronomía y Astrofísica*, 41:61–67.

Davis, C. J., Dent, W. R. F., and Burnell, S. J. B. (1990). HCO(+) observations of the Herbig-Haro objects 1 and 2. *Monthly Notices of the Royal Astronomical Society*, 244:173–180.

De Colle, F. and Raga, A. C. (2005). Interaction of Herbig-Haro objects with molecular cloud and generation of Alfvén waves. *Monthly Notices of the Royal Astronomical Society*, 359:164–170.

de Gregorio-Monsalvo, I., Gómez, J. F., Suárez, O., Kuiper, T. B. H., Rodríguez, L. F., and Jiménez-Bailón, E. (2006). CCS and NH_3 Emission Associated with Low-Mass Young Stellar Objects. *The Astrophysical Journal*, 642:319–329.

Devine, D., Bally, J., Reipurth, B., and Heathcote, S. (1997). Kinematics and Evolution of the Giant HH34 Complex. *The Astronomical Journal*, 114:2095.

Di Francesco, J., Hogerheijde, M. R., Welch, W. J., and Bergin, E. A. (2002). Abundances of Molecular Species in Barnard 68. *The Astronomical Journal*, 124:2749–2755.

Di Francesco, J., Myers, P. C., Wilner, D. J., Ohashi, N., and Mardones, D. (2001). Infall, Outflow, Rotation, and Turbulent Motions of Dense Gas within NGC 1333 IRAS 4. *The Astrophysical Journal*, 562:770–789.

Draine, B. T. and McKee, C. F. (1993). Theory of interstellar shocks. *Annual Review of Astronomy and Astrophysics*, 31:373–432.

Duarte-Cabral, A., Dobbs, C. L., Peretto, N., and Fuller, G. A. (2011). Was a cloud-cloud collision the trigger of the recent star formation in Serpens? *Astronomy and Astrophysics*, 528:A50.

Duarte-Cabral, A., Fuller, G. A., Peretto, N., Hatchell, J., Ladd, E. F., Buckle, J., Richer, J., and Graves, S. F. (2010). The physical and dynamical structure of Serpens. Two very different sub-(proto)clusters. *Astronomy and Astrophysics*, 519:A27.

Evans, II, N. J. (1999). Physical Conditions in Regions of Star Formation. *Annual Review of Astronomy and Astrophysics*, 37:311–362.

Falle, S. A. E. G. and Hartquist, T. W. (2002). Generation of density inhomogeneities by magnetohydrodynamic waves. *Monthly Notices of the Royal Astronomical Society*, 329:195–203.

Fernández-López, M., Curiel, S., Girart, J. M., Ho, P. T. P., Patel, N., and Gómez, Y. (2011). Millimeter and Submillimeter High Angular Resolution Interferometric Observations: Dust in the Heart of IRAS 18162-2048. *The Astronomical Journal*, 141:72–+.

Fontani, F., Caselli, P., Bourke, T. L., Cesaroni, R., and Brand, J. (2008). Highly deuterated pre-stellar cores in a high-mass star formation region. *Astronomy and Astrophysics*, 477:L45–L48.

Frau, P., Girart, J. M., and Beltrán, M. T. (2012). Chemical differentiation toward the Pipe nebula starless cores. *Astronomy and Astrophysics*, 537:L9.

Frau, P., Girart, J. M., Beltrán, M. T., Morata, O., Masqué, J. M., Busquet, G., Alves, F. O., Sánchez-Monge, Á., Estalella, R., and Franco, G. A. P. (2010). Young Starless Cores Embedded in the Magnetically Dominated Pipe Nebula. *The Astrophysical Journal*, 723:1665–1677.

Furst, E., Reich, W., Reich, P., and Reif, K. (1990). A Radio Continuum Survey of the Galactic Plane at 11-CENTIMETER Wavelength - Part Four - a List of 6483 Small Diameter Sources. *Astronomy and Astrophysics Supplement Series*, 85:805.

Garrod, R. T., Williams, D. A., Hartquist, T. W., Rawlings, J. M. C., and Viti, S. (2005). The chemistry of transient dense cores. *Monthly Notices of the Royal Astronomical Society*, 356:654–664.

Girart, J., Estalella, R., and Ho, P. T. P. (1998). On the Nature of the Molecular Condensation Downstream from HH 80 North. *The Astrophysical Journal, Letters*, 495:L59+.

Girart, J. M., Estalella, R., Viti, S., Williams, D. A., and Ho, P. T. P. (2001). Star Formation Signatures in the Condensation Downstream of HH 80N. *The Astrophysical Journal, Letters*, 562:L91–L94.

Girart, J. M., Rodríguez, L. F., Anglada, G., Estalella, R., Torrelles, J. M., Marti, J., Pena, M., Ayala, S., Curiel, S., and Noriega-Crespo, A. (1994). Ammonia downstream from HH 80 North. *The Astrophysical Journal, Letters*, 435:L145–L148.

Girart, J. M., Viti, S., Estalella, R., and Williams, D. A. (2005). The molecular condensations ahead of Herbig-Haro objects. III. Radiative and dynamical perturbations of the HH 2 condensation. *Astronomy and Astrophysics*, 439:601–612.

Girart, J. M., Viti, S., Williams, D. A., Estalella, R., and Ho, P. T. P. (2002). The molecular condensations ahead of Herbig-Haro objects. I. Multi-transition observations of HH 2. *Astronomy and Astrophysics*, 388:1004–1015.

Goicoechea, J. R., Berné, O., Gerin, M., Joblin, C., and Teyssier, D. (2008). Star Formation near Photodissociation Regions: Detection of a Peculiar Protostar near Cederblad 201. *The Astrophysical Journal*, 680:466–473.

Graves, S. F., Richer, J. S., Buckle, J. V., Duarte-Cabral, A., Fuller, G. A., Hogerheijde, M. R., Owen, J. E., Brunt, C., Butner, H. M., Cavanagh, B., Chrysostomou, A., Curtis, E. I., Davis, C. J., Etxaluze, M., Francesco, J. D., Friberg, P., Friesen, R. K., Greaves, J. S., Hatchell, J., Johnstone, D., Matthews, B., Matthews, H., Matzner, C. D., Nutter, D., Rawlings, J. M. C., Roberts, J. F., Sadavoy, S., Simpson, R. J., Tothill, N. F. H., Tsamis, Y. G., Viti, S., Ward-Thompson, D., White, G. J., Wouterloot, J. G. A., and Yates, J. (2010). The JCMT Legacy Survey of

the Gould Belt: a first look at Serpens with HARP. *Monthly Notices of the Royal Astronomical Society*, 409:1412–1428.

Gyulbudaghian, A. L., Glushkov, Y. I., and Denisyuk, E. K. (1978). New Herbig-Haro objects. *The Astrophysical Journal, Letters*, 224:L137+.

Hacar, A. and Tafalla, M. (2011). Dense core formation by fragmentation of velocity-coherent filaments in L1517. *Astronomy and Astrophysics*, 533:A34.

Haro, G. (1952). Herbig's Nebulous Objects Near NGC 1999. *The Astrophysical Journal*, 115:572–+.

Haro, G. (1953). Hα Emission Stars and Peculiar Objects in the Orion Nebula. *The Astrophysical Journal*, 117:73–+.

Hayashi, C. (1966). Evolution of Protostars. *Annual Review of Astronomy and Astrophysics*, 4:171–+.

Healy, K. R., Hester, J. J., and Claussen, M. J. (2004). A Very Large Array Search for Water Masers in Six H II Regions: Tracers of Triggered Low-Mass Star Formation. *The Astrophysical Journal*, 610:835–850.

Hennebelle, P., Whitworth, A. P., Gladwin, P. P., and André, P. (2003). Protostellar collapse induced by compression. *Monthly Notices of the Royal Astronomical Society*, 340:870–882.

Herbig, G. H. (1950). The Spectrum of the Nebulosity Surrounding T Tauri. *The Astrophysical Journal*, 111:11–+.

Herbig, G. H. (1951). The Spectra of Two Nebulous Objects Near NGC 1999. *The Astrophysical Journal*, 113:697–699.

Herbst, E. and Klemperer, W. (1973). The Formation and Depletion of Molecules in Dense Interstellar Clouds. *The Astrophysical Journal*, 185:505–534.

Howe, D. A., Taylor, S. D., and Williams, D. A. (1996). The chemistry of core collapse in TMC1. *Monthly Notices of the Royal Astronomical Society*, 279:143–151.

Jennings, R. E., Cameron, D. H. M., Cudlip, W., and Hirst, C. J. (1987). IRAS observations of NGC1333. *Monthly Notices of the Royal Astronomical Society*, 226:461–471.

Jørgensen, J. K., Bourke, T. L., Myers, P. C., Schöier, F. L., van Dishoeck, E. F., and Wilner, D. J. (2005). Probing the Inner 200 AU of Low-Mass Protostars with the Submillimeter Array: Dust and Organic Molecules in NGC 1333 IRAS 2A. *The Astrophysical Journal*, 632:973–981.

Jørgensen, J. K., Schöier, F. L., and van Dishoeck, E. F. (2002). Physical structure and CO abundance of low-mass protostellar envelopes. *Astronomy and Astrophysics*, 389:908–930.

Jørgensen, J. K., Schöier, F. L., and van Dishoeck, E. F. (2004). Molecular inventories and chemical evolution of low-mass protostellar envelopes. *Astronomy and Astrophysics*, 416:603–622.

Kenyon, S. J., Calvet, N., and Hartmann, L. (1993). The embedded young stars in the Taurus-Auriga molecular cloud. I - Models for spectral energy distributions. *The Astrophysical Journal*, 414:676–694.

Kirk, J. M., Ward-Thompson, D., and André, P. (2005). The initial conditions of isolated star formation - VI. SCUBA mappingof pre-stellar cores. *Monthly Notices of the Royal Astronomical Society*, 360:1506–1526.

Klessen, R. S. (2001). The Formation of Stellar Clusters: Mass Spectra from Turbulent Molecular Cloud Fragmentation. *The Astrophysical Journal*, 556:837–846.

Lada, C. J. (1987). Star formation - From OB associations to protostars. In M. Peimbert & J. Jugaku, editor, *Star Forming Regions*, volume 115 of *IAU Symposium*, pages 1–17.

Ladd, N., Purcell, C., Wong, T., and Robertson, S. (2005). Beam Size, Shape and Efficiencies for the ATNF Mopra Radio Telescope at 86-115 GHz. *Publications of the Astronomical Society of Australia*, 22:62–72.

Langer, W. D. and Penzias, A. A. (1990). C-12/C-13 isotope ratio across the Galaxy from observations of C-13/O-18 in molecular clouds. *The Astrophysical Journal*, 357:477–492.

Langer, W. D. and Penzias, A. A. (1993). (C-12)/(C-13) isotope ratio in the local interstellar medium from observations of (C-13)(O-18) in molecular clouds. *The Astrophysical Journal*, 408:539–547.

Leão, M. R. M., de Gouveia Dal Pino, E. M., Falceta-Gonçalves, D., Melioli, C., and Geraissate, F. G. (2009). Local star formation triggered by supernova shocks in magnetized diffuse neutral clouds. *Monthly Notices of the Royal Astronomical Society*, 394:157–173.

Lizano, S. and Shu, F. H. (1989). Molecular cloud cores and bimodal star formation. *The Astrophysical Journal*, 342:834–854.

Lucas, R. and Liszt, H. (1998). Interstellar isotope ratios from mm-wave molecular absorption spectra. *Astronomy and Astrophysics*, 337:246–252.

Maret, S., Ceccarelli, C., Caux, E., Tielens, A. G. G. M., and Castets, A. (2002). Water emission in NGC 1333-IRAS 4. The physical structure of the envelope. *Astronomy and Astrophysics*, 395:573–585.

Maret, S., Ceccarelli, C., Caux, E., Tielens, A. G. G. M., Jørgensen, J. K., van Dishoeck, E., Bacmann, A., Castets, A., Lefloch, B., Loinard, L., Parise, B., and Schöier, F. L. (2004). The H_2CO abundance in the inner warm regions of low mass protostellar envelopes. *Astronomy and Astrophysics*, 416:577–594.

Maret, S., Ceccarelli, C., Tielens, A. G. G. M., Caux, E., Lefloch, B., Faure, A., Castets, A., and Flower, D. R. (2005). CH3OH abundance in low mass protostars. *Astronomy and Astrophysics*, 442:527–538.

Martí, J., Rodríguez, L. F., and Reipurth, B. (1993). HH 80-81: A Highly Collimated Herbig-Haro Complex Powered by a Massive Young Star. *The Astrophysical Journal*, 416:208–+.

Martí, J., Rodríguez, L. F., and Reipurth, B. (1995). Large Proper Motions and Ejection of New Condensations in the HH 80-81 Thermal Radio Jet. *The Astrophysical Journal*, 449:184–+.

Martí, J., Rodríguez, L. F., and Reipurth, B. (1998). Proper Motions of the Inner Condensations in the HH 80-81 Thermal Radio Jet. *The Astrophysical Journal*, 502:337–+.

Martin-Pintado, J., Bachiller, R., and Fuente, A. (1992). SIO Emission as a Tracer of Shocked Gas in Molecular Outflows. *Astronomy and Astrophysics*, 254:315.

Masqué, J. M., Girart, J. M., Beltrán, M. T., Estalella, R., and Viti, S. (2009). The Molecular Emission of the Irradiated Star-Forming Core Ahead of HH 80N. *The Astrophysical Journal*, 695:1505–1516.

Masunaga, H. and Inutsuka, S.-i. (2000). Infall Signatures in Spectral Line Profiles of Protostellar Envelopes. *The Astrophysical Journal*, 536:406–415.

McLaughlin, D. E. and Pudritz, R. E. (1996). A model for the internal structure of molecular cloud cores. *Journal of the Royal Astronomical Society of Canada*, 90:326.

McMullin, J. P., Mundy, L. G., and Blake, G. A. (1994). The circumstellar environment of IRAS 05338-0624. *The Astrophysical Journal*, 437:305–316.

McMullin, J. P., Mundy, L. G., Blake, G. A., Wilking, B. A., Mangum, J. G., and Latter, W. B. (2000). A Spectral Line Study of Serpens S68 FIRS1 Region. *The Astrophysical Journal*, 536:845–856.

Molinari, S., Noriega-Crespo, A., and Spinoglio, L. (2001). A Shock-induced Photodissociation Region in the HH 80/81 Flow: Far-Infrared Spectroscopy. *The Astrophysical Journal*, 547:292–301.

Morata, O., Estalella, R., Lopez, R., and Planesas, P. (1997). CS observations of star-forming regions. *Monthly Notices of the Royal Astronomical Society*, 292:120–+.

Morata, O., Girart, J. M., and Estalella, R. (2003). Multitransitional observations of the CS core of L673. *Astronomy and Astrophysics*, 397:181–189.

Morata, O., Girart, J. M., and Estalella, R. (2005). Evidence for transient clumps and gas chemical evolution in the CS core of L673. *Astronomy and Astrophysics*, 435:113–124.

Moriarty-Schieven, G. H., Snell, R. L., Strom, S. E., Schloerb, F. P., Strom, K. M., and Grasdalen, G. L. (1987). High-resolution images of the L1551 bipolar outflow - Evidence for an expanding, accelerated shell. *The Astrophysical Journal*, 319:742–753.

Motte, F. and André, P. (2001). The circumstellar environment of low-mass protostars: A millimeter continuum mapping survey. *Astronomy and Astrophysics*, 365:440–464.

Mundt, R., Brugel, E. W., and Buehrke, T. (1987). Jets from young stars - CCD imaging, long-slit spectroscopy, and interpretation of existing data. *The Astrophysical Journal*, 319:275–303.

Neufeld, D. A. and Dalgarno, A. (1989). Fast molecular shocks. I - Reformation of molecules behind a dissociative shock. *The Astrophysical Journal*, 340:869–893.

Ohashi, N., Hayashi, M., Ho, P. T. P., and Momose, M. (1997). Interferometric Imaging of IRAS 04368+2557 in the L1527 Molecular Cloud Core: A Dynamically Infalling Envelope with Rotation. *The Astrophysical Journal*, 475:211–+.

Osorio, M., Anglada, G., Lizano, S., and D'Alessio, P. (2009). Collapsing Hot Molecular Cores: A Model for the Dust Spectrum and Ammonia Line Emission of the G31.41+0.31 Hot Core. *The Astrophysical Journal*, 694:29–45.

Osorio, M., D'Alessio, P., Muzerolle, J., Calvet, N., and Hartmann, L. (2003). A Comprehensive Study of the L1551 IRS 5 Binary System. *The Astrophysical Journal*, 586:1148–1161.

Osorio, M., Lizano, S., and D'Alessio, P. (1999). Hot Molecular Cores and the Formation of Massive Stars. *The Astrophysical Journal*, 525:808–820.

Ossenkopf, V. and Henning, T. (1994). Dust opacities for protostellar cores. *Astronomy and Astrophysics*, 291:943–959.

Padoan, P. and Nordlund, Å. (2002). The Stellar Initial Mass Function from Turbulent Fragmentation. *The Astrophysical Journal*, 576:870–879.

Pagani, L., Pardo, J.-R., Apponi, A. J., Bacmann, A., and Cabrit, S. (2005). L183 (L134N) revisited. III. The gas depletion. *Astronomy and Astrophysics*, 429:181–192.

Palau, A., Estalella, R., Girart, J. M., Ho, P. T. P., Zhang, Q., and Beuther, H. (2007). Star formation in a clustered environment around the UCH {II} region in IRAS 20293+3952. *Astronomy and Astrophysics*, 465:219–233.

Palla, F. and Stahler, S. W. (1993). The Pre-Main-Sequence Evolution of Intermediate-Mass Stars. *The Astrophysical Journal*, 418:414–+.

Pastor, J., Buj, J., Estalella, R., Lopez, R., Anglada, G., and Planesas, P. (1991). A CS study of star-forming regions previously mapped in ammonia. *Astronomy and Astrophysics*, 252:320–330.

Penzias, A. A., Wannier, P. G., Wilson, R. H., and Linke, R. A. (1977). Deuterium in the Galaxy. *The Astrophysical Journal*, 211:108–114.

Plambeck, R. L. and Snell, R. L. (1995). Observations of the Clumpy Shell of the L1551 Bipolar Outflow. *The Astrophysical Journal*, 446:234–+.

Pratap, P., Dickens, J. E., Snell, R. L., Miralles, M. P., Bergin, E. A., Irvine, W. M., and Schloerb, F. P. (1997). A Study of the Physics and Chemistry of TMC-1. *The Astrophysical Journal*, 486:862–+.

Pudritz, R. E. and Norman, C. A. (1983). Centrifugally driven winds from contracting molecular disks. *The Astrophysical Journal*, 274:677–697.

Rathborne, J. M., Jackson, J. M., Chambers, E. T., Stojimirovic, I., Simon, R., Shipman, R., and Frieswijk, W. (2010). The Early Stages of Star Formation in Infrared Dark Clouds: Characterizing the Core Dust Properties. *The Astrophysical Journal*, 715:310–322.

Rawlings, G. C. I. (1982). St.Elmos Fire. *Journal of the British Astronomical Association*, 92:148–+.

Rawlings, J. M. C., Hartquist, T. W., Menten, K. M., and Williams, D. A. (1992). Direct diagnosis of infall in collapsing protostars. I - The theoretical identification of molecular species with broad velocity distributions. *Monthly Notices of the Royal Astronomical Society*, 255:471–485.

Redman, R. O., Feldman, P. A., Wyrowski, F., Côté, S., Carey, S. J., and Egan, M. P. (2003). Interactions between a Bright Young Stellar Object and the Midcourse Space Experiment Infrared-dark Cloud G79.3+0.3: An Early Stage of Triggered Star Formation? *The Astrophysical Journal*, 586:1127–1135.

Reipurth, B., Bally, J., and Devine, D. (1997). Giant Herbig-Haro Flows. *The Astronomical Journal*, 114:2708–+.

Roberts, H., Herbst, E., and Millar, T. J. (2003). Enhanced Deuterium Fractionation in Dense Interstellar Cores Resulting from Multiply Deuterated H_3^+. *The Astrophysical Journal, Letters*, 591:L41–L44.

Roberts, H. and Millar, T. J. (2000). Modelling of deuterium chemistry and its application to molecular clouds. *Astronomy and Astrophysics*, 361:388–398.

Rodríguez, L. F., Ho, P. T. P., Torrelles, J. M., Curiel, S., and Canto, J. (1990). VLA observations of the Herbig-Haro 1-2 system. *The Astrophysical Journal*, 352:645–653.

Rodríguez, L. F., Moran, J. M., Ho, P. T. P., and Gottlieb, E. W. (1980). Radio observations of water vapor, hydroxyl, silicon monoxide, ammonia, carbon monoxide, and compact H II regions in the vicinities of suspected Herbig-Haro objects. *The Astrophysical Journal*, 235:845–865.

Rodríguez, L. F. and Reipurth, B. (1989). Detection of radio continuum emission from the Herbig-Haro objects 80 and 81 and their suspected energy source. *Revista Mexicana de Astronomía y Astrofísica*, 17:59–63.

Roueff, E., Lis, D. C., van der Tak, F. F. S., Gerin, M., and Goldsmith, P. F. (2005). Interstellar deuterated ammonia: from NH_3 to ND_3. *Astronomy and Astrophysics*, 438:585–598.

Rudolph, A. and Welch, W. J. (1988). Herbig-Haro objects as shocked ambient cloudlets - High-resolution radio observations of HH 7-11. *The Astrophysical Journal, Letters*, 326:L31–L34.

Ruoskanen, J., Harju, J., Juvela, M., Miettinen, O., Liljeström, A., Väisälä, M., Lunttila, T., and Kontinen, S. (2011). Mapping the prestellar core Ophiuchus D (L1696A) in ammonia. *Astronomy and Astrophysics*, 534:A122.

Saito, S., Ozeki, H., Ohishi, M., and Yamamoto, S. (2000). Observations of NH_2D toward Dark Molecular Clouds. *The Astrophysical Journal*, 535:227–230.

Sandell, G., Knee, L. B. G., Aspin, C., Robson, I. E., and Russell, A. P. G. (1994). A molecular jet and bow shock in the low mass protostellar binary NGC 1333-IRAS2. *Astronomy and Astrophysics*, 285:L1–L4.

Schaller, G., Schaerer, D., Meynet, G., and Maeder, A. (1992). New grids of stellar models from 0.8 to 120 solar masses at Z = 0.020 and Z = 0.001. *Astronomy and Astrophysics Supplement Series*, 96:269–331.

Schneider, S. and Elmegreen, B. G. (1979). A catalog of dark globular filaments. *The Astrophysical Journal Supplement Series*, 41:87–95.

Schöier, F. L., Jørgensen, J. K., van Dishoeck, E. F., and Blake, G. A. (2002). Does IRAS 16293-2422 have a hot core? Chemical inventory and abundance changes in its protostellar environment. *Astronomy and Astrophysics*, 390:1001–1021.

Shu, F. H. (1977). Self-similar collapse of isothermal spheres and star formation. *The Astrophysical Journal*, 214:488–497.

Shu, F. H., Adams, F. C., and Lizano, S. (1987). Star formation in molecular clouds - Observation and theory. *Annual Review of Astronomy and Astrophysics*, 25:23–81.

Shu, F. H., Najita, J., Ostriker, E. C., and Shang, H. (1995). Magnetocentrifugally Driven Flows from Young Stars and Disks. V. Asymptotic Collimation into Jets. *The Astrophysical Journal, Letters*, 455:L155+.

Spitzer, L. (1978). *Physical processes in the interstellar medium.*

Suzuki, H., Yamamoto, S., Ohishi, M., Kaifu, N., Ishikawa, S.-I., Hirahara, Y., and Takano, S. (1992). A survey of CCS, HC3N, HC5N, and NH3 toward dark cloud cores and their production chemistry. *The Astrophysical Journal*, 392:551–570.

Sweitzer, J. S. (1978). On the excitation of interstellar ammonia in the Kleinmann-Low nebula. *The Astrophysical Journal*, 225:116–129.

Tafalla, M., Mardones, D., Myers, P. C., Caselli, P., Bachiller, R., and Benson, P. J. (1998). L1544: A Starless Dense Core with Extended Inward Motions. *The Astrophysical Journal*, 504:900.

Tafalla, M., Myers, P. C., Caselli, P., and Walmsley, C. M. (2004). On the internal structure of starless cores. I. Physical conditions and the distribution of CO, CS, N_2H^+, and NH_3 in L1498 and L1517B. *Astronomy and Astrophysics*, 416:191–212.

Tafalla, M., Myers, P. C., Caselli, P., Walmsley, C. M., and Comito, C. (2002). Systematic Molecular Differentiation in Starless Cores. *The Astrophysical Journal*, 569:815–835.

Tafalla, M., Santiago-García, J., Myers, P. C., Caselli, P., Walmsley, C. M., and Crapsi, A. (2006). On the internal structure of starless cores. II. A molecular survey of L1498 and L1517B. *Astronomy and Astrophysics*, 455:577–593.

Taylor, S. D., Morata, O., and Williams, D. A. (1996). The distribution of CS and NH_3_ in star-forming regions. *Astronomy and Astrophysics*, 313:269–276.

Taylor, S. D., Morata, O., and Williams, D. A. (1998). The distribution of molecules in star-forming regions. *Astronomy and Astrophysics*, 336:309–314.

Taylor, S. D. and Williams, D. A. (1996). Molecular emission ahead of Herbig-Haro bow shocks. *Monthly Notices of the Royal Astronomical Society*, 282:1343–1348.

Terebey, S., Shu, F. H., and Cassen, P. (1984). The collapse of the cores of slowly rotating isothermal clouds. *The Astrophysical Journal*, 286:529–551.

Tielens, A. G. G. M. and Hagen, W. (1982). Model calculations of the molecular composition of interstellar grain mantles. *Astronomy and Astrophysics*, 114:245–260.

Tiné, S., Roueff, E., Falgarone, E., Gerin, M., and Pineau des Forêts, G. (2000). Deuterium fractionation in dense ammonia cores. *Astronomy and Astrophysics*, 356:1039–1049.

Tobin, J. J., Hartmann, L., Bergin, E. A., Chiang, H.-F., Looney, L. W., Chandler, C. J., Maret, S., and Heitsch, F. (2012). Complex Structure in Class 0 Protostellar Envelopes III: Velocity Gradients in Non-Axisymmetric Envelopes, Infall or Rotation? *ArXiv e-prints*.

Tobin, J. J., Hartmann, L., Chiang, H.-F., Looney, L. W., Bergin, E. A., Chandler, C. J., Masqué, J. M., Maret, S., and Heitsch, F. (2011). Complex Structure in Class 0 Protostellar Envelopes. II. Kinematic Structure from Single-dish and Interferometric Molecular Line Mapping. *The Astrophysical Journal*, 740:45.

Torrelles, J. M., Gomez, J. F., Ho, P. T. P., Anglada, G., Rodriguez, L. F., and Canto, J. (1993). Ammonia Emission Downstream of the Herbig-Haro Object 1. *The Astrophysical Journal*, 417:655–+.

Torrelles, J. M., Rodriguez, L. F., Canto, J., Anglada, G., Gomez, J. F., Curiel, S., and Ho, P. T. P. (1992). On the nature of the excitation of Herbig-Haro object 2. *The Astrophysical Journal, Letters*, 396:L95–L97.

Ungerechts, H., Bergin, E. A., Goldsmith, P. F., Irvine, W. M., Schloerb, F. P., and Snell, R. L. (1997). Chemical and Physical Gradients along the OMC-1 Ridge. *The Astrophysical Journal*, 482:245–+.

van der Tak, F. F. S., Black, J. H., Schöier, F. L., Jansen, D. J., and van Dishoeck, E. F. (2007). A computer program for fast non-LTE analysis of interstellar line spectra. With diagnostic plots to interpret observed line intensity ratios. *Astronomy and Astrophysics*, 468:627–635.

van Dishoeck, E. F., Blake, G. A., Jansen, D. J., and Groesbeck, T. D. (1995). Molecular Abundances and Low-Mass Star Formation. II. Organic and Deuterated Species toward IRAS 16293-2422. *The Astrophysical Journal*, 447:760–+.

van Loo, S., Falle, S. A. E. G., and Hartquist, T. W. (2006). Generation of density inhomogeneities by magnetohydrodynamic waves in two dimensions. *Monthly Notices of the Royal Astronomical Society*, 370:975–980.

van Loo, S., Falle, S. A. E. G., and Hartquist, T. W. (2007). Dense core compression and fragmentation induced by the scattering of hydromagnetic waves. *Monthly Notices of the Royal Astronomical Society*, 376:779–784.

Viti, S., Girart, J. M., Garrod, R., Williams, D. A., and Estalella, R. (2003). The molecular condensations ahead of Herbig-Haro objects. II. A theoretical investigation of the HH 2 condensation. *Astronomy and Astrophysics*, 399:187–195.

Viti, S., Girart, J. M., and Hatchell, J. (2006). An observational survey of molecular emission ahead of Herbig-Haro objects. *Astronomy and Astrophysics*, 449:1089–1100.

Viti, S. and Williams, D. A. (1999a). Chemical evolution ahead of Herbig-Haro objects. *Monthly Notices of the Royal Astronomical Society*, 310:517–526.

Viti, S. and Williams, D. A. (1999b). Time-dependent evaporation of icy mantles in hot cores. *Monthly Notices of the Royal Astronomical Society*, 305:755–762.

Whyatt, W., Girart, J. M., Viti, S., Estalella, R., and Williams, D. A. (2010). The clumpiness of molecular clouds: HCO^+ (3-2) survey near Herbig-Haro objects. *Astronomy and Astrophysics*, 510:A74+.

Wilking, B. A., Doering, C. R., Harvey, P. M., Lada, C. J., and Joy, M. (1984). The formation of massive stars along the W5 ionization front. *The Astrophysical Journal*, 279:291–303.

Wolfire, M. G. and Koenigl, A. (1993). Molecular line emission models of Herbig-Haro objects. II - HCO(+) emission. *The Astrophysical Journal*, 415:204–217.

Wootten, A., Loren, R. B., and Snell, R. L. (1982). A study of DCO+ emission regions in interstellar clouds. *The Astrophysical Journal*, 255:160.

Yamashita, T., Suzuki, H., Kaifu, N., Tamura, M., Mountain, C. M., and Moore, T. J. T. (1989). A new CO bipolar flow and dense disk system associated with the infrared reflection nebula GGD 27 IRS. *The Astrophysical Journal*, 347:894–900.

Yokogawa, S., Kitamura, Y., Momose, M., and Kawabe, R. (2003). High Angular Resolution, Sensitive CS J = 2-1 and J = 3-2 Imaging of the Protostar L1551 NE: Evidence for Outflow-triggered Star Formation? *The Astrophysical Journal*, 595:266–278.

Zhou, S., Evans, II, N. J., Koempe, C., and Walmsley, C. M. (1993). Evidence for protostellar collapse in B335. *The Astrophysical Journal*, 404:232–246.